EMBRY-RIDDLE
Aeronautical University™
SCHOLARLY COMMONS

Dissertations and Theses

12-2019

Development of a Research Spacecraft Test-Bed with Implementation of Control Laws to Compensate Undesired Dynamics

Yomary Angélica Betancur Vesga

DEVELOPMENT OF A RESEARCH SPACECRAFT TEST-BED WITH

IMPLEMENTATION OF CONTROL LAWS TO COMPENSATE UNDESIRED

DYNAMICS

A Thesis

Submitted to the Faculty of

Embry-Riddle Aeronautical University

By

Yomary Angélica Betancur Vesga

In Partial Fulfillment of the Requirements for the Degree of

Master of Science in Aerospace Engineering

December 2019

Embry-Riddle Aeronautical University

Daytona Beach, Florida

DEVELOPMENT OF A RESEARCH SPACECRAFT TEST-BED WITH IMPLEMENTATION OF CONTROL LAWS TO COMPENSATE UNDESIRED DYNAMICS
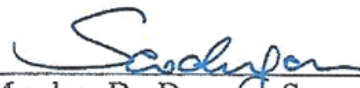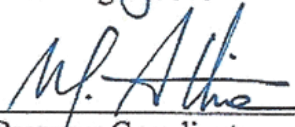
by

Yomary Angélica Betancur Vesga

This Thesis was prepared under the direction of the candidate's committee chairman, Dr. Hever Moncayo, Department of Aerospace Engineering, and has been approved by the members of the thesis committee. It was submitted to the Office of the Senior Vice President for Academic Affairs and Provost, and was accepted in partial fulfillment of the requirements for the degree of Master of Science in Aerospace Engineering.

THESIS COMMITTEE

Chairman, Dr. Hever Moncayo

Member, Dr. Troy Henderson

Member, Dr. Dongeun Seo
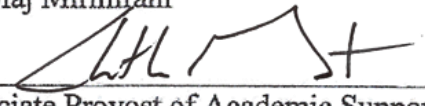
Graduate Program Coordinator,
Dr. Magdy Attia

Date 12 . 5 . 2019

Dean of College of Engineering,
Dr. Maj Mirmirani

Date 12/5/19

Associate Provost of Academic Support
Dr. Christopher Grant

Date 12/5/19

I dedicate this thesis to my family – Mrs. Graciela Lopez, Mrs. Yomary Vesga, Mr. William Betancur, Teresa, Sandra Leidy, Dairo and Luis; Shaggy, Merlina, Lulú and the Bird family.

ACKNOWLEDGMENTS

The completion of this thesis is by far one of the most significant academic achievements in my career as an engineer for it represents years of learning, perseverance growth; and most importantly, it is the embodiment of a long-lasting goal I had since I was at school: to contribute to space research. When I look back, I have nothing but a feeling of appreciation and gratitude for every rewarding moment of this learning curve and for every person who assisted me along the way. Onboard of this journey, there was an incredibly talented team that provided valuable expertise and support in the development of this mission. Not only their guidance contributed to my professional progress but also my personal growth. As such, I would like to send my special acknowledgements to my supervisor, Dr. Hever Moncayo, for guiding me with his experience and expertise, and for being a remarkable mentor in my academic life. Also, thank you for supporting my research through the grant from NASA.

Likewise, I would like to thank the Embry Riddle Aeronautical University for being a second home and for supporting my research by providing a facility and tools. It is much appreciated. Distinctive acknowledgements to my Advisory Committee: Dr. Troy Henderson and Dr. Dungeon Seo, Thank you for the valuable gift of your time and collaboration. Special thanks to Michael Potash and Bill Russo, for your interest on my research, and your insightful participation and mentoring role in building my knowledge foundations and understanding throughout this journey.

I also recognize my research contributors from Rishika Banerjee. Your insights were vital to build the spacecraft. Thank you to those who encouraged me to pursue a graduate degree: my family, my professors, and my friends: Andrei, Karina, Nolan, Cindy, Juan,

Diana, Mansi, and Sharath for listening and cheering me up throughout this process. Last but not least, thank you to God for allowing this dream to become true.

TABLE OF CONTENTS

Page

LIST OF TABLES

LIST OF FIGURES

SYMBOLS

L_x, L_y, L_z	Actual Distance of each Thruster to the CG of the vehicle
α_r	Angle of Rotation
$\vec{H}$	Angular Momentum Vector
$\tilde{e}_\Omega$	Angular Rate Performance Metric
$\dot{\omega}_x, \dot{\omega}_y, \dot{\omega}_z$	Angular Rates in the X, Y and Z axes
$\omega_x, \omega_y, \omega_z$	Angular Velocities in the X, Y and Z axes
$\vec{\omega}(t)$	Angular Velocity Vector
$\tilde{\delta}_q$	Attitude Performance Metric
B_f	Body Fixed Reference Frame
$\ddot{\vec{r}}$	Center of the Mass
$K_{\omega q}$	Control Gain Matrices
$u_{NLDI}(t)$	Control law
$\vec{q} \otimes \vec{q}_c$	Cross Product of Two Quaternions
ζ	Damping Ratio
Q_d	Desired quaternion
T_n	Desired Thrust
$\vec{q} \odot \vec{q}_c$	Dot Product between Two Quaternions
ϕ, θ, ψ	Euler Angles
P_I	Global Performance Index Metric
J	Inertial Matrix

I_f	Inertial Reference Frame
$\Omega(\omega(t))$	Kinematic Quaternion Matrix
λ	Lambda
$[M]_{3x2}$	Matrix of the thrust misalignment error in the X, Y and Z axes
$\Delta\alpha$	Misalignment Angle with respect to the X and Y axes
$\Delta\beta$	Misalignment Angle with respect to the Z axis
$\vec{M}(t)$	Moment Vector
$M_x M_y M_z$	Moments in the X, Y, and Z axes
$\omega_{n:x,y,z}$	Natural Frequency
β	Nomimal Misalignment Angle with respect to the X and Y axes
α	Nominal Misalignment Angle with respect to the X and Y axes
$p(\lambda)$	Polynomial Characteristic Equation
$J_x\ J_y\ J_z$	Principal Moments of Inertia
$\vec{q}'$	Quaternion Conjugate
δq_e	Quaternion Error
q_0	Quaternion Scalar Part
$\vec{q}$	Quaternion Vector
$\vec{q}_{1:3} \in \Re^3$	Quaternion Vector Part
$R_{I_q}^B$	Rotational Matrix
$\tilde{s}$	Solenoid Performance Metric
$\vec{x}$	State Vector

$\kappa(t)$ Thrust Magnitude Error function time

$\vec{F}(t)$ Total Force Vector

m Total Mass of the System

$n_1, n_2, n_3,$ Vector Components of the Principal Axis of Rotation

$\vec{q}_{R\psi} \ \vec{q}_{R\theta} \ \vec{q}_{R\phi}$ Vector Components of the Rotational Matrix

$u_v(q,\omega)$ Virtual Controller

$\vec{P}_{1x3}$ X, Y, and Z vector of the desired thrust without any error

ABBREVIATIONS

ADCL Advanced Dynamics and Control Research Laboratory

DCM Direct Cosine Matrix

EASY Extreme Access System

EKF Extended Kalman Filter

ERAU Embry-Riddle Aeronautical University

HP High Pressure

IGOR Integrated Gravity Offloading Robotic System

IMU Inertia Measurement Unit

LiPo Lithium-ion Polymer

LP Low Pressure

LPR Low Pressure Regulator

MTE Mathematical Thrust Error Model

PC/104 Onboard Computer PCM-3355 Reference

PR1-2 Pressure Regulators

PS1-4 Pressure Sensors

PWM Pulse Width Modulated

Q1-24 Solenoid Valves

R1-2 Reservoirs

RV1-4 Relief Valves

SBC Single Board Computer

TMAE Thrust Misalignment Angle Error

TME Thrust Magnitude Error

TVCC   Thrust Vectoring Control Configuration

UDP   User Datagram Protocol

ABSTRACT

The development of research spacecraft systems has a significant impact on the preparation and simulation of future space missions. Hardware, software and operation procedures can be adequately tested, validated and verified before they are deployed for the actual mission. In this thesis, a spacecraft vehicle test-bed named Extreme Access System (EASY) was developed. EASY aims at supporting validation and verification of guidance, navigation and control algorithms. Description of EASY spacecraft systems, sub-systems and integration is presented in this thesis along with an analysis of results from numerical simulation and actual implementation of control laws. An attitude control architecture based on quaternion feedback linearization is also described, and performance analysis in the compensation of undesired dynamics is presented. The results show the capabilities and potential of EASY to simulate missions that require validation and verification stages.

1. Introduction

For years, the paradigm of space exploration has been a field of interest among researchers. Over the last decade, the development of new space technologies geared towards human space exploration and the search for space bodies holding new resources have exponentially increased. These types of missions require significant progress in order to cope with the extreme conditions of these environments, which in general include precise landing procedures, cooperative control, proximity operations, rendezvous, docking maneuvers. Hence, for a space mission to be successful, it has become vital the development of spacecraft test-bed so the hardware, software, control algorithms, and operation procedures can be tested, validated and verified on the ground to ensure precision and system functionality.

Many teams have contributed to the development of vehicle technologies that access these environments to complete exploration and resource extraction missions (Brophy, 2014; Hockman, Frick, Nesnas & Pavone 2015). For instance, Hover of Mini-Free Flyer Prototype XA-B and Hover of a Mars Mini-Free Flyer Prototype XA-C (See figure 1.1a and 1.1b) developed by NASA are two type of vehicles that were built with the aim of reaching restricted areas where a normal rover cannot operate (Prazenica, 2016). Its design, similar to a quad-copter, restricts its effective functionality in environments of low gravity where there is no existence of air.

More realistic prototypes such as the Mars Mini-Free Flyer and the Asteroid prospector flyer developed at NASA's Kennedy Space Center are alternative space vehicle approaches that use a gimbaled frame to allow free motion of the vehicle in roll, pitch and yaw axes (see Figure 1.1c and 1. 1d) (Perez, 2016). This gimbaled frame allows

the demonstration of angular velocity regulation in gravity less environments. However, this test-bed setup presents undesired friction in the attitude motion and does not allow vehicle translation, which reduces the overall testing performance and reliability.
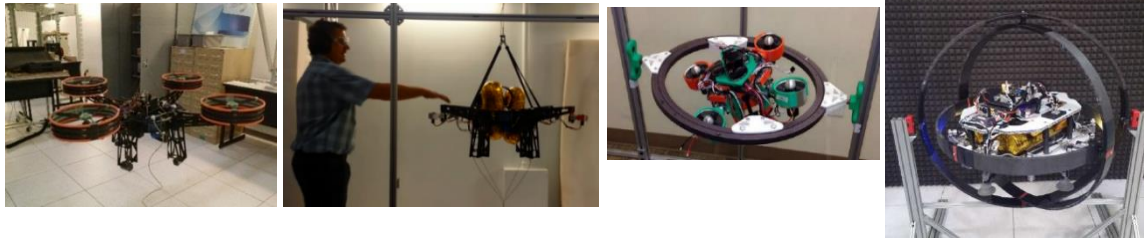
| a. Hover of a Mini-Free Flyer Prototype XA-B | b. Hover of a Mars Mini-Free Flyer Prototype XA-C | c. Mars Mini-Free Flyer Prototype Mounted in Gimbal Setup. | d. Asteroid Spacecraft Mounted in Gimbal Setup |

Figure 1.1 Facilities for Testing Mini-Free Flyer Prototypes for Extreme Access Environments.

As per all of these types of missions, appropriate testing facilities for those vehicles have become challenging. This is because constraints such as gravity and degrees of freedom hinders the acquisition of correct data to test and validate guidance, navigation, and control algorithms.

To overcome the aforementioned challenges, recent research efforts at the Advanced Dynamics and Control Research Laboratory (ADCL) at Embry Riddle Aeronautical University have been focused on the development of new extreme access vehicles and multiple control law algorithms that ensure guidance, navigation, and control of space vehicles as well as test-fidelity facility on-ground capable of simulating partial gravity (Garcia, 2017). This thesis aims to contribute to such a research goal.

In this thesis, a research Spacecraft test-bed Extreme Access System (EASY) is introduced and developed along with the implementation of a quaternion feedback linearization based control system. Additionally, a Mathematical Thrust Error model

(MTE) is presented to describe undesired dynamics such as Thrust Magnitude Error (TME) and Thrust Misalignment Angles Error (TMAE). Finally, the results of simulation and implementation are shown with the integration of the whole system.

1.1 Thesis Outline

This thesis is organized as follows. Firstly, Chapter 2 provides an overview of the different systems and components that integrate the Extreme Access System (EASY) research test-bed. As such, a description is provided regarding mechanical, pneumatic or propulsion, electronic, and electrical components. Chapter 3 presents a general description of quaternions and how they are used to represent spacecraft's dynamics and kinematics. Chapter 4 focuses on the modelling of undesired dynamics by understanding the impact of thrust misalignment angles errors and thrust magnitude errors. The design and development of control laws for attitude stabilization are then presented in Chapter 5. Chapter 6 describes a developed simulation environment using MATLAB/Simulink software that support numerical simulation for performance analysis of the control laws. A flight testing environment is also presented in Chapter 7 by implementing the Integrated Gravity Offloading Robotic System (IGOR). Complementary in chapter 8, an analysis of the performance system in the simulation and implementation stages is provided to investigate the control and stability capabilities of EASY's control system. Finally, general conclusions regarding the development, testing and analysis of results of EASY's spacecraft are presented.

2. Extreme Access System –EASY Research Test-Bed

The purpose of this chapter is to introduce the Extreme Access System (EASY) research test-bed and its main components. A description of the mechanical, pneumatic or propulsion, electronic, and electrical systems is provided, including a general review of the hardware that was implemented. Two types of main configurations of the mechanical system are also considered: standard and Thrust Vectoring Control (TVCC).

The pneumatic or propulsion system is developed with a focus on the EASY's nozzle design, the test-bed duty cycle, and the pneumatic or propulsion system components, which include the solenoid valve, compressed air tanks and air compressor. As per the electronic system, the description includes the electrical system along with the onboard computer, sensors, communication hardware, power, and propulsion hardware. Finally, a description of the manufacture and assembly process is provided.

No.	Equipment
1	Antenna
2	Air Compressed tanks
3	On-board Computer PC-104
4	IMU- Microstrain
5	Solenoid
6	Thrust Vectoring Config. Thrusters
7	Standard Config. Thrusters
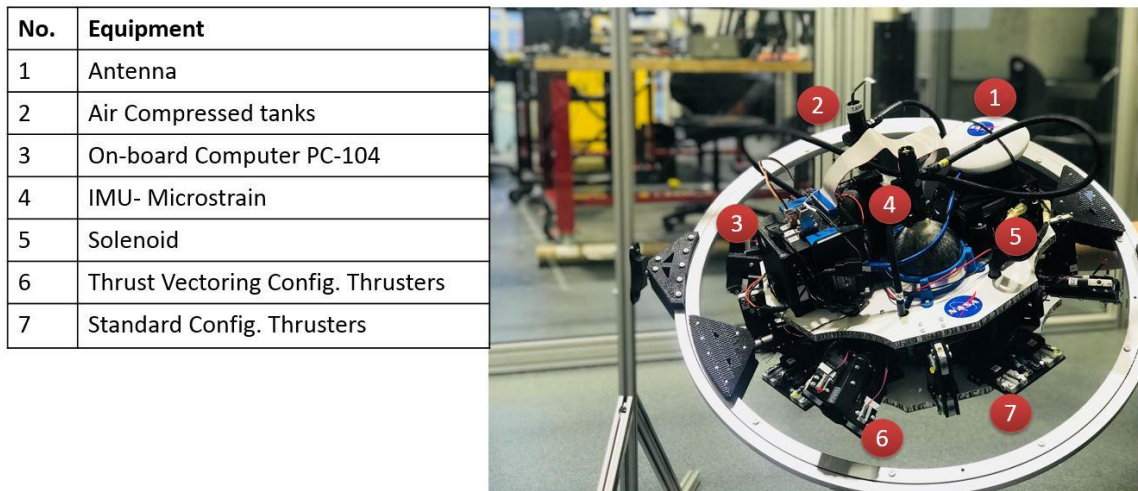
Figure 2.1 EASY Spacecraft.

2.1 EASY Spacecraft

EASY is a novel concept of spacecraft developed to support the testing, validation and verification of guidance, navigation and control algorithms required for space

exploration missions (See Figure 2.1). EASY integrates four main systems: mechanical, pneumatic or propulsion, electronic, and electrical systems.

2.2 Mechanical System

The mechanical system consists of two configuration types: standard and Thrust Vectoring Control (TVCC). In the standard configuration, the spacecraft uses sixteen fixed thrusters grouped in pairs. Here, a yaw rotation is created by the thrusters that are orthogonally located to the reference plane X and Y. The second type of configuration known as Thrust Vectoring Control, uses eight thrusters placed in pairs that are connected to a servo motor mechanism. This configuration allows each pair of solenoids to have a rotation around its position to achieve a yaw rotation. In both configurations through control allocation equations, an arrangement of thrusters is turned on and off to produce pitch, roll and yaw maneuvers. Figure 2.2 depicts the location of each of the thrusters around the X and Y axes of the vehicle.
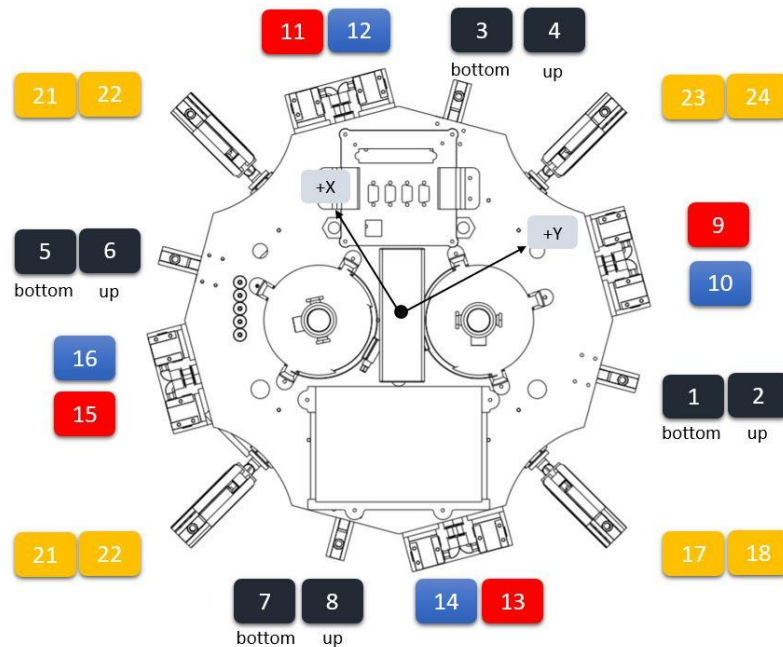
Figure 2.2 Location of the Thrusters in the X and Y Axes.

2.2.1 Standard Configuration

In standard configuration, EASY uses thrusters number 1, 2, 3, 4, 5, 6, 7 and 8 to generate pitching maneuvers in the positive and negative directions about the Y axis. This is shown in Figure 2.3. For pitching maneuvers in the positive direction, thrusters 2, 3, 5 and 8 are fired while thrusters 1, 4, 6 and 7 remain off. For negative pitching maneuvers, thrusters 1, 4, 6 and 7 are fired while 2, 3, 5 and 8 remain off.
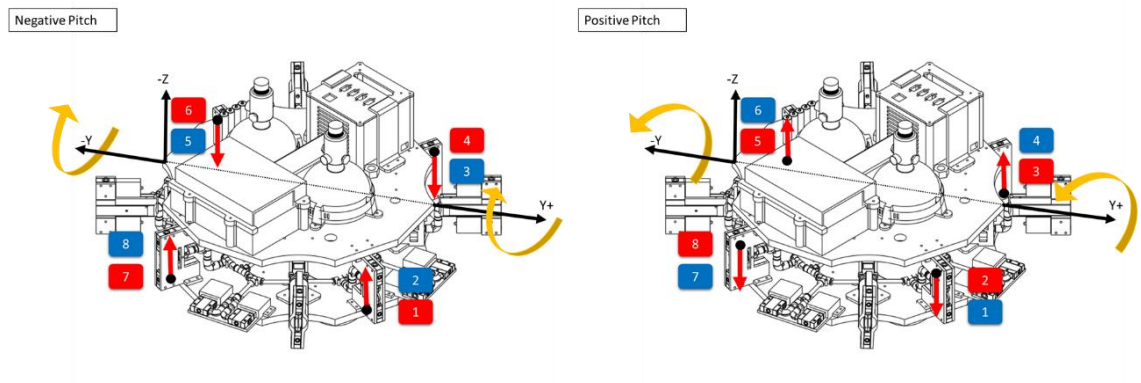
Figure 2.3 EASY Pitching Maneuver, Standard Configuration.
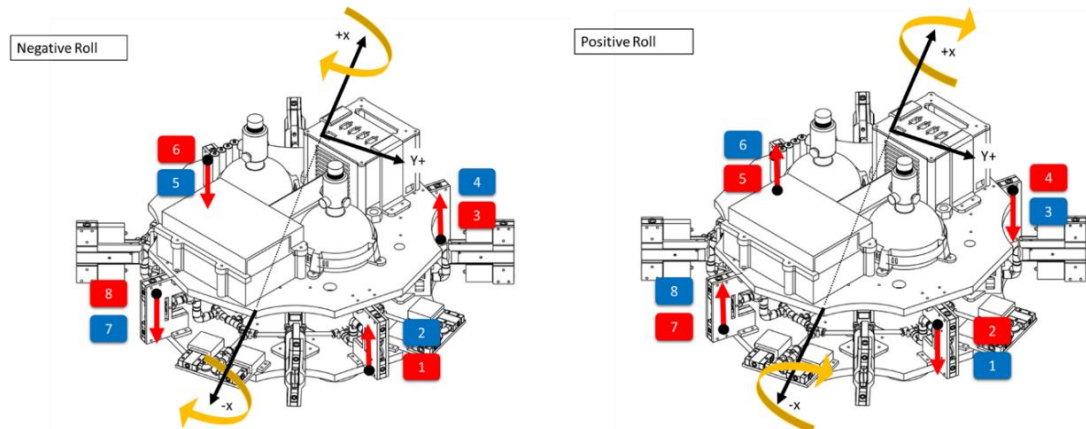
Figure 2.4 EASY Rolling Maneuver, Standard Configuration.

Figure 2.4 shows a roll maneuver in the positive and negative direction around the X axis. Thrusters 2, 4, 5 and 7 are fired while thrusters 1, 3, 6 and 8 remain off in order to

generate a positive roll rotation. In the opposite rotation, thrusters 1, 3, 6 and 8 must be fired while thrusters 2, 4, 5 and 7 remain off.

Yaw motion is accomplished by using four pairs of solenoids as shown in Figure 2.5. To perform a yaw maneuver in a positive direction about the Z axis, thrusters 9, 11, 13, and 15 are fired while solenoids 10, 12, 14, and 16 remain off. For a yaw maneuver in a negative direction about the Z axis, thrusters 10, 12, 14, and 16 are fired while thrusters 9, 11, 13, and 15 must remain off.
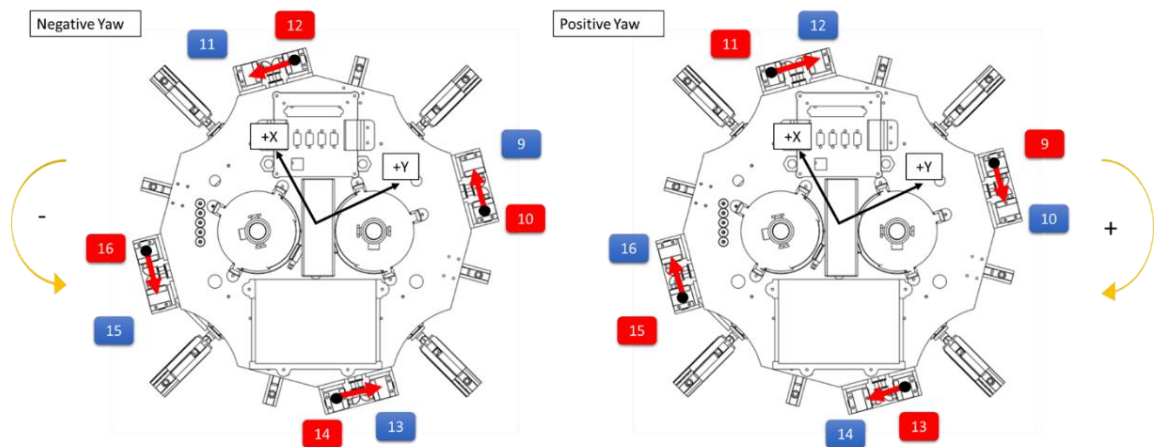
Figure 2.5 EASY Yawing Maneuver, Standard Configuration.

2.2.2 Thrust Vectoring Control Configuration

The second type refers to Thrust Vectoring Control Configuration (TVCC). In this configuration, EASY uses thrusters number 17, 18, 19, 20, 21, 22, 23, and 24 to perform pitching maneuvers in the positive and negative directions about the Y axis. This is shown in Figure 2.6. For a positive pitching maneuver, thrusters 18, 20, 21, and 23 are fired while 17, 19, 22, and 24 remain off. For negative pitching maneuvers, thrusters 17, 19, 22, and 24 are fired while 18, 20, 21, and 23 remain off.

Figure 2.7. shows a rolling maneuver in the negative and positive direction about the X axis. For a negative rolling maneuver, thrusters 17, 20, 22, and 23 are fired while

thrusters 18, 19, 21, and 24 remain off. For a positive rolling maneuver, thrusters 18, 19, 21, and 24 are fired while thrusters 17, 20, 22, and 23 remain off.
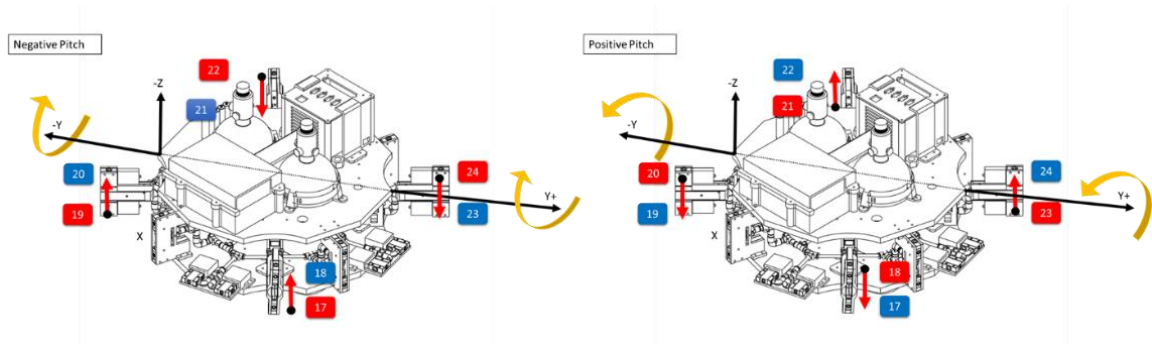
Figure 2.6 EASY Pitching Maneuver, Thrust Vectoring Control Configuration.
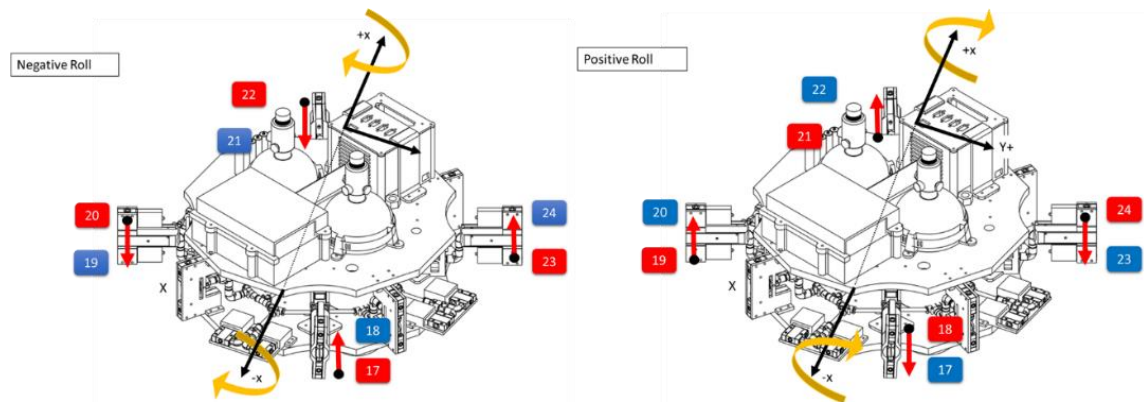
Figure 2.7 EASY Rolling Maneuver, Thrust Vectoring Control Configuration.

To accomplish yaw motion, all four pairs of thrusters must rotate in the same direction. This rotation will allow the spacecraft to produce either a negative or positive yaw movement, as shown in Figure 2.8 and Figure 2.9, respectively. To perform a yaw maneuver in a positive direction about the Z axis, thrusters 17, 19, 21, and 23 are fired while thrusters 18, 20, 22, and 24 remain off. For yaw movement in a negative direction about the Z axis, thrusters 18, 20, 22, and 24 are fired while thrusters 17, 19, 21, remain off.
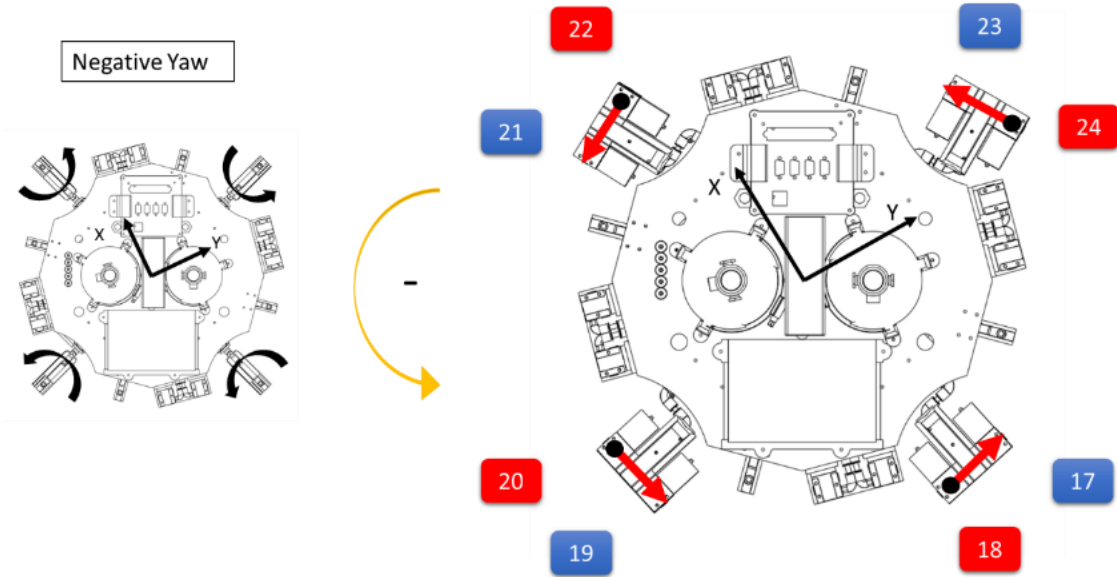
Figure 2.8 EASY Negative Yawing Maneuver, Thrust Vectoring Control Configuration.
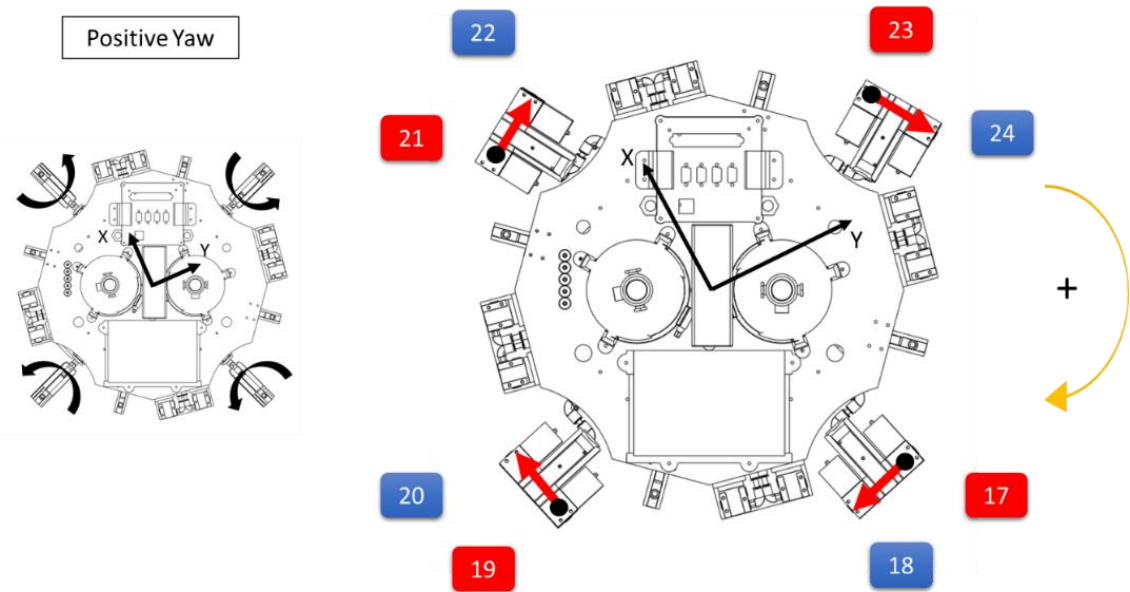
Figure 2.9 EASY Positive Yawing Maneuver, Thrust Vectoring Control Configuration.

2.3 Pneumatic or Propulsion System

The overall functionality of the EASY's pneumatic or propulsion system is illustrated in Figure 2.10. Compressed air was selected as the primary energy supply for the propulsion system due to its simplicity and safety for indoor testing. The compressed

air used in the spacecraft is stored in a pair of reservoirs (R1, R2) at high pressure. The

reservoirs, fabricated with composite materials, can contain up to 90 cubic inch of

compressed air at 4500 psi as maximum pressure.

To handle the high pressure coming from the reservoirs, four pressure regulators

(PR1 – 4) are used to regulate the pressure within the system. Two regulator pressures

PR1 and PR2 are located in the high-pressure zone to drop the pressure from 4500 psi to

an output pressure range of 800 to 850 psi. The second pair of pressure regulators are

located in the low-pressure area. Similar to the first pair of pressure regulators, this pair

drop the pressure from 800-850 psi to 130 psi, which is the desired operating pressure of

the thrusters. Tubing plastic with high-pressure resistance is installed within the system to

distribute the pressure to each of the thrusters.

Additionally, four sensors (PS1-4) are placed along the system to monitor the

pressure levels. For safety purposes, four relief valves (RV1 - 4) are used before each

pressure regulator in case the system suffers overpressure. Solenoid valves (Q1-24) are

placed at the end of the system with their corresponding nozzles. Each nozzle has been

designed to produce at least 1 Newton of Thrust.

2.3.1 Nozzle

The EASY's nozzle design is based on three main assumptions. First, the gas flow is

assumed to be quasi-one-dimensional. Second, the flow is considered isentropic (no heat

transfer). Third, the gas is treated as a perfect (ideal) gas. With these assumptions,

multiple iterations were performed to obtain the optimal configuration of the nozzle. The

maximum thrust obtained with the actual configuration of the nozzle at an operating

pressure of 130 psi in the simulation was 2.0 Ns. Table 2.1 shows the main characteristics

of EASY's nozzle.
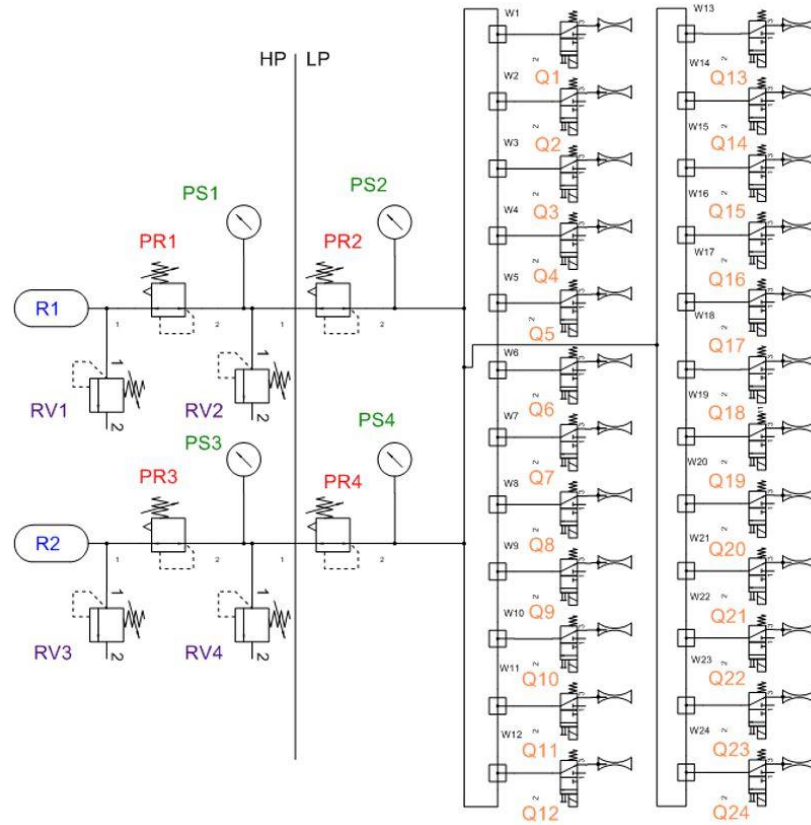
Figure 2.10 EASY's Pneumatic System Schematic.

Table 2.1

Characteristics of the EASY's Nozzle

Parameter	Value
Pressure at the entrance of the Nozzle	130 psi
Mach at the Throat	1
Ratio of specific heats	1.4
Specific gas constant	286.8881 kg/moL
Molar mass of air	0.028966
Diameter at the entrance	0.282 cm
Diameter at the throat	0.414 cm
Diameter at the exit	0.30 cm

2.3.2 Test-Bed for duty cycle characterization

2.3.2.1 Duty Cycle

Pulse Width Modulated (PWM) signals are used to determinate the duty cycle of a solenoid valve. PWM signals are based on two main characteristics: the frequency and time period or cycle. The frequency is characterized by two features: the first one is related to the velocity of the switching between the maximum and minimum value of the signal. The second one defines how fast the PWM signal completes a time period.
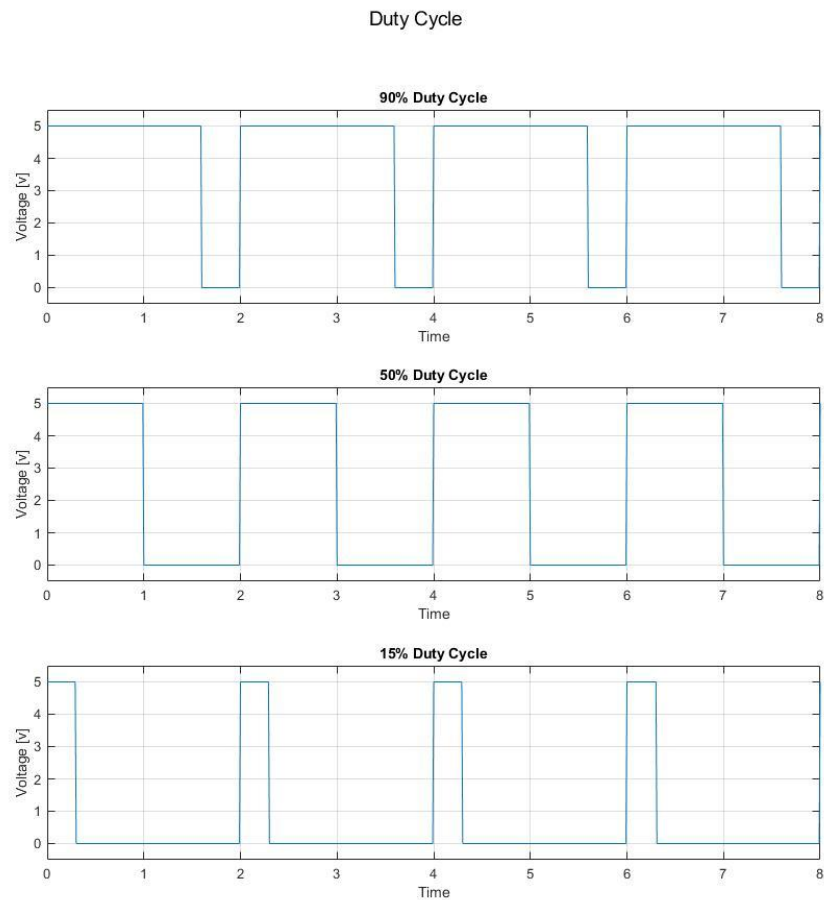
Figure 2.11 Duty Cycle of a Solenoid Valve.

The duty cycle of a PWM signal for a solenoid valve is determined by the amount of time that the valve remains open or closed during one period of time. It is considered a 100% duty cycle when the solenoid valve remains open during the whole time period. In the same way, 50% of duty cycle occurs when the solenoid valve remains open only for half of the time period. Figure 2.11 represents a typical behavior of a PWM signal with 90%, 50%, and 15% of duty cycle used in EASY to command a specific thruster activity.

2.3.2.2 Nozzle's TestBed

Nozzle's testbed (see Figure 2.12) was developed to obtain data regarding the amount of thrust produced by the thruster when the entry pressure at the nozzle is 130 psi. The Nozzle's testbed uses a single solenoid valve with its corresponding nozzle assembly. A voltage is provided to the solenoid valve by using an external power source. The compressed air is supplied to the thrusters by using the pair of reservoirs described in Section 2.2. The nominal operating pressure provided by the reservoirs is 130 psi. A PC/104 onboard computer and an I/O digital expansion board are used to compile codes and send digital commands to the thruster. The PC/104 onboard computer runs a boot system called Simulink real-time that uses xPC-Target tool. The xPC- Target is set up on a Host Computer using Matlab and enables the capability of the system to communicate in real-time with the onboard computer using TC/IP interface communication. This way, duty cycle commands can be sent to the solenoid valve.

A stochastic method is implemented to characterize the performance of the thruster. This method uses a scale to read small weights in grams (with 0.01 g sensitivity for accurate measurements). The thruster is located on the scale, and it is calibrated by considering the weight of the thruster so that it reaches zero without any action.

Once the duty cycle commands are sent from the Host computer, the scale provides

the weight sensed. A direct correlation between the weight and duty cycle can be made to

get the total force produced. As a result, thrust values are obtained at different constant

duty cycle, as well as, the maximum thrust produced by the thruster. The maximum thrust

achieved at 100% of the duty cycle was 1.35 Newtons.
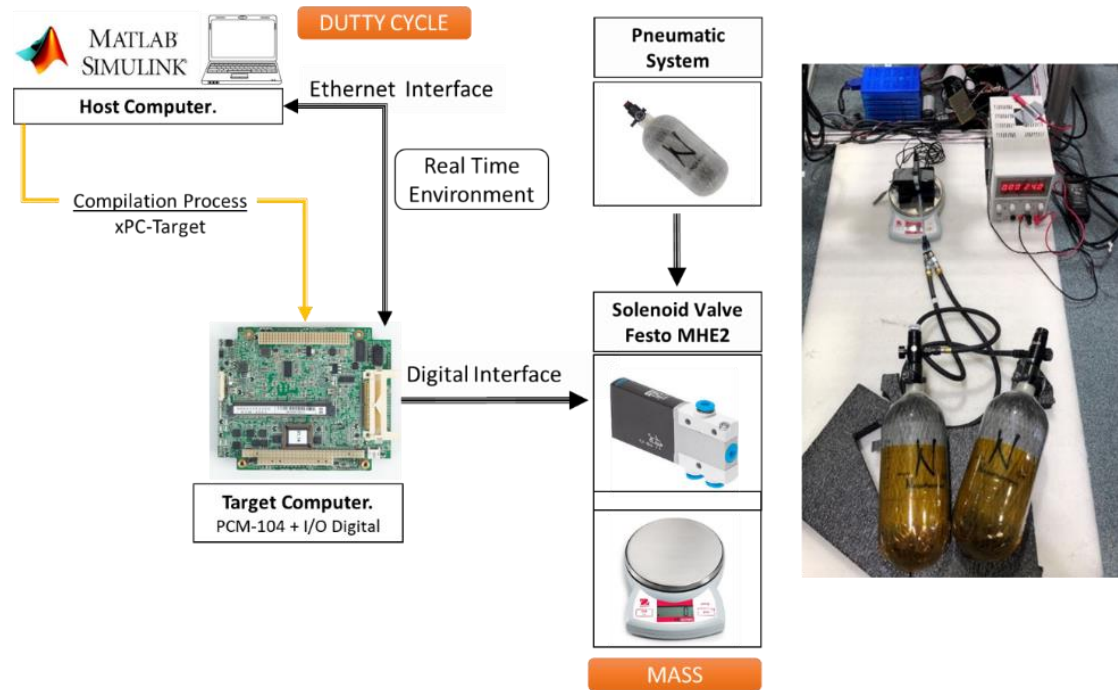
Figure 2.12 Nozzle's Testbed Setup.

The results obtained from the nozzle's testbed were grouped into a lookup table, as

shown in Figure 2.13. This lookup table shows the relationship between normalized

thrust and percentage of duty cycle where 0.1 and 1 represent the 10 %, and 100% of the

duty cycle, respectively. Thus, the output given to the thruster will be in terms of duty

cycle, which depends on how much thrust is required.
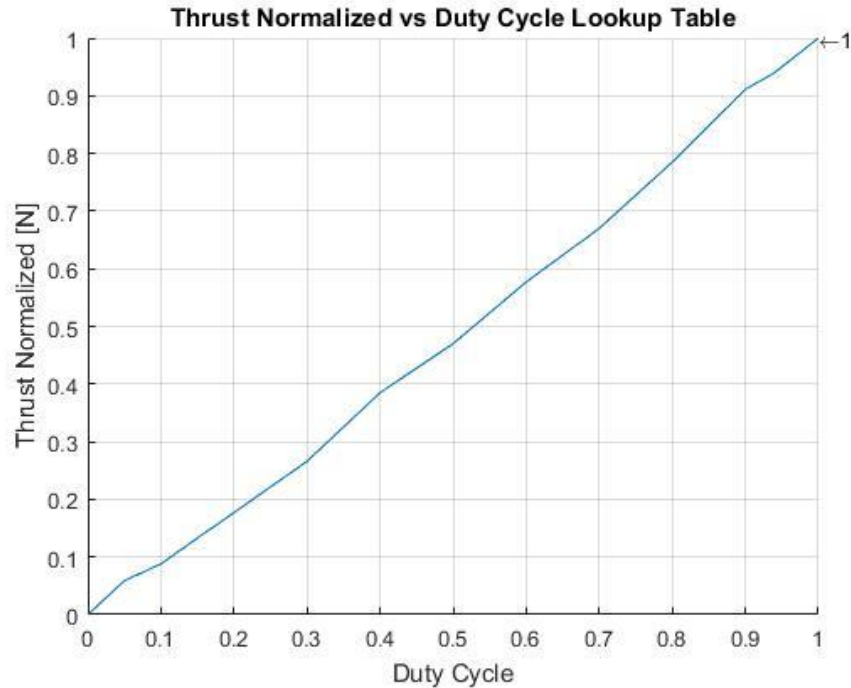
Figure 2.13 Thrust Normalized vs Duty Cycle Lookup Table.

2.3.3 Pneumatic or Propulsion Components

In this section, is presented an overall description of the principal pneumatic or propulsion components used for EASY spacecraft within its pneumatic or propulsion system. A solenoid valve, compressed air tanks with big bore line and an air compressor as described in terms of main functionality characteristics.

2.3.3.1 Solenoid Valve

The solenoid valve selected were Festo MHE2-M1H-3/2G-M7 of electrical actuation (see Figure 2.14). The MHE2 solenoid valve is a 3/2 closed monostable configuration with mechanical spring. Its normal nominal flow rate is 100 [l/min] with a maximum switching frequency of 130 Hz and a repetition accuracy of ±0.2ms. This fast-switching rate provides response times of 2-millisecond speed within a shorter cycle time. This

solenoid valve offers a constant dynamic response regardless of temperature or supply

voltage fluctuations with an extremely long service life of 500 million cycles (FESTO,

n.d.). It can be powered on with 24 V DC/1 A and no maintenance is required.

Figure 2.14 MHE2-M1H-3/2G-M Solenoid Valve by FESTO® (FESTO, n.d.).

2.3.3.2 Compressed Air Tanks

Since compressed air was chosen as the main source of energy for EASY'S

propulsion system, the reservoirs selected to store the compressed air were a pair of Ninja

Lite carbon fiber air tanks - 90/4500 (see Figure 2.15). These commercial tanks are

fabricated in composed materials and contain D.O.T and TC regulations approved.

Additionally, these tanks have a 5-year hydro test guarantee. Each ninja tank provides a

capacity of 90 cubic inch of storage and can contain up to 4500 psi. (NINJA, 2019).

The tanks have installed pressure regulators which provide a high output pressure

between 800 and 850 psi. Due to the need for regulating the output pressure to the desired

operating pressure 130 psi, the second stage of regulators is located on top of the first

stage. The second stage of regulators is Ninja V2 LPR (see Figure 2.15). To drive the

pressure around EASY, two big bore lines are connected to the second stage of

regulators, which drive the pressure to a set of plastic tubing. The plastic tubing finally

drives the pressure to the solenoids by using different FESTO® pneumatic connectors.

Figure 2.15 Ninja Lite Air Tank - 90/4500 and Ninja V2 LPR Regulator with Big Bore Line (NINJA, 2019).

2.3.3.3 Air Compressor

The solenoids MHE2 selected and described in previous sections operate with compressed air that complies with the regulations established in ISO 8573-1:2010 [7:4:4]. These regulations are related to air quality type. Because of this, specific setup of air purification is mandatory. Additionally, equipment to fill the compressed air tanks with a pressure capability up to 4500 psi is required. As a solution to these two previous requests, the W31 Mariner electrical compressor (See Figure 2.16) is selected to fill the requirements. W31 Mariner provides P21 Purifier with Refillable Purifier Element, 2nd and 3rd Stage Water Condensate & Oil Separator that complies with Air Quality regulations established in ISO 8573-1:2010 [7:4:4]. Moreover, this compressor has a maximum operating pressure of 5000 psi with a charging rate of 105 l/min (Compressors, 2019).

Figure 2.16 W31 Marine Air Compressor by Alkin® (Compressors, 2019).

2.4 Electronic System

Within the EASY's electronic system, an EASY's solenoid driver board was designed, built and tested. This board provides control of the switching on/off of each solenoid valve, as well as, the communication interface between the mentioned board and the onboard computer PC/104. This interface is manage by the use of I/O digital ports.

The block diagram shown in Figure 2.17 depicts an example of the schematic of 4 out of 24 channels that integrates EASY's solenoid driver board. Each channel represents each of the 24 Festo solenoid valves. The overall system is powered with 22.4 Volts. The main components of EASY's solenoid driver board include resistors, diodes, and MOSFET transistors. The MOSFET transistor controls the flow of current to the solenoid valve. A set of diodes is used in order to prevent voltage spikes (caused by the continuous fast switching on/off of the solenoids) from potentially damaging the transistors. Moreover, the circuit contains a series of LEDs that are turned on at the same time that the solenoids are in operation. The implementation of the LED allows the proper identification of solenoids that are being operated at a specific time.
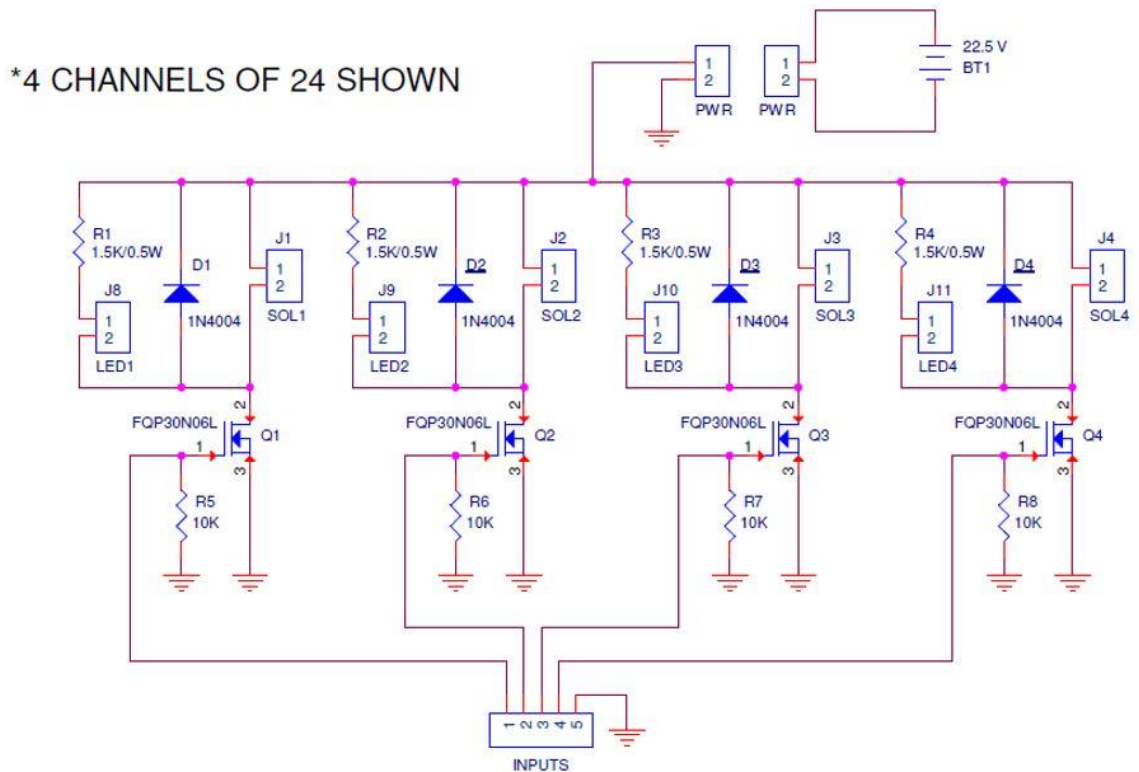
Figure 2.17 EASY's Solenoid Driver Board Schematic.

2.5 Electrical Power System

The provision of electrical power for EASY is perhaps one of the most fundamental requirements. Failure in the electrical power system will result in the loss of any hardware. In general, the electrical power system consists of two major energy sources, an overvoltage protection system and a power control/distribution network.

The two primary energy sources distribute voltage to two different lines (see Figure 2.18). The first line receives a power source of 22.4 V while the second line receives 14.8 V. A control/distribution network delivers the appropriate voltage/current levels to each of the components. This network uses three DC-DC CONV for 5, 6, and 24 output voltage. Thus, from the first line, the onboard computer can be powered on with 5V and the Solenoid driver board with 22.4 V. From the second line, the Antenna and servos are

powered on with 6 V and 24 V, respectively. Finally, an overvoltage protection system keeps the onboard computer protected from any overvoltage condition. This system uses a crowbar circuit. When an overvoltage condition occurs, a tripping of the circuit breaker indicates that the system is being protected.
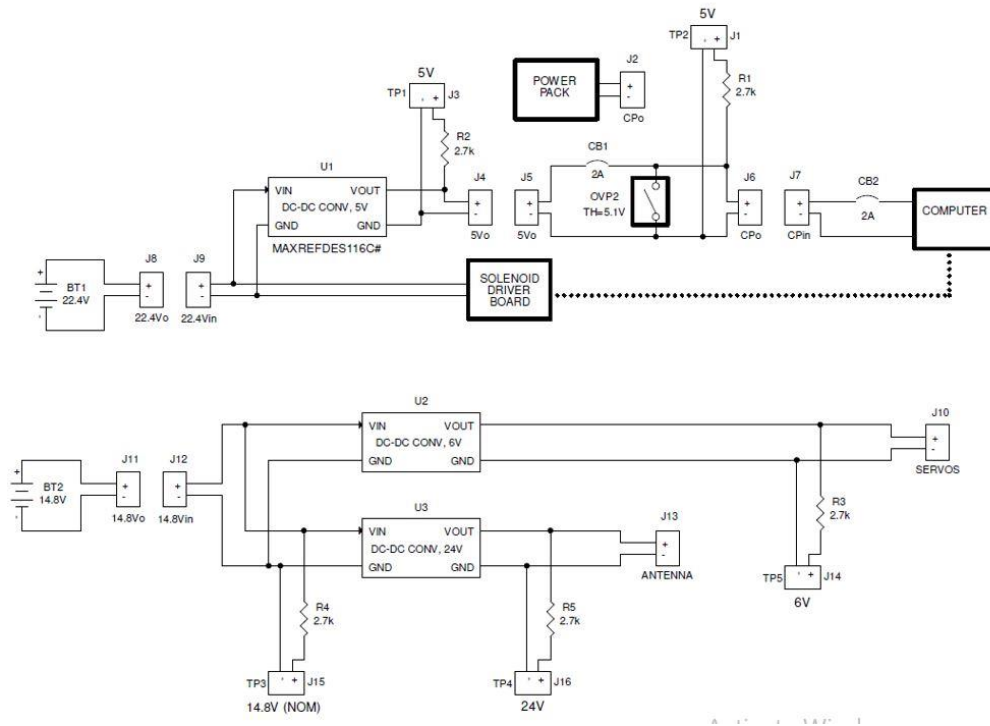
Figure 2.18 EASY's Electrical System Schematic.

2.6 Hardware Description

In this section, is presented an overall description of the hardware components used in EASY spacecraft.

2.6.1 Onboard Computer

The PC/104 reference PCM -3355 computer (see Figure 2.19) was selected as the onboard computer to process the control laws algorithms and to integrate sensors data collection. The PCM-3355 is a small (96X9mm) single-board computer (SBC) that offers acceptable processing and memory capabilities (1GB). This SBC computer supports

different types of serial communication, such as RS-232 (two), RS-422/485(one), SATA

(one), and USB 2.0 (two ports). Additionally, it includes multiple I/Os, and a single

10/100Mbps Ethernet. The PCM-3355 uses an AMD low power LX800/500 MHz and

LX600/366 MHz Processor. This SBC has the capability to use TCP/IP protocol to

download codes on it. Furthermore, PCM-3355 offers a convenient connector layout for

an easy system expansibility (ADVANTECH, 2019). This computer can be powered with

+5V or +12V.

Figure 2.19 PC/104 Computer - Reference PCM -3355 by Advantech® (ADVANTECH, 2019).

An Emerald –MM-4M-Port Serial Module (see Figure 2.20) is integrated into the

PCM-3355 to provide additional serial port capacity. This board provides four serial ports

operating at speeds up to 15 kbps (Diamond Systems, 2019). The power consumption of

this board is not higher than +5V, which the power to be on through its connection with

the PCM-3355. The connection between the Emerald –MM-4M-Port Serial Module and

the PCM-3355 computer is made through the PC/104 8-bit and 16-bit bus connectors.

Figure 2.20 Emerald –MM-4M-Port Serial Module by Diamond Systems® (Diamond, Systems 2019).

An additional Onyx MM Digital I/O Module (See Figure 2.21.) is also integrated

with the PCM-3355 and the Emerald –MM-4M-Port Serial Module. This board provides

digital communication capabilities. It features 48 digital I/O lines, 3 16-bit

counter/timers, and 3 independent PC bus interrupt inputs (Diamond Systems, 2019). The

digital I/O lines are used to communicate with the EASY's solenoid driver board.

Figure 2.21 Onyx MM Digital I/O Module by Diamond Systems® (Diamond Systems, 2019).

2.6.2 Sensors

   An inertial measurement unit (IMU) is used in EASY to provide accurate data

information of angular rates and attitude (Euler and quaternions). The 3DM-GX4-45™

by Lord MicroStrain® (see Figure 2. 22.) is selected as the IMU. This IMU features

various embedded sensors such as a triaxial accelerometer, gyroscope, magnetometer,

temperature sensors, and a pressure altimeter. The main characteristics of these sensors

are shown in Table 2. 2. The 3DM-GX4-45™ IMU runs a sophisticated Extended

Kalman Filter (EKF) to provide excellent data output of position, velocity, and attitude

using Dual on-board processors (LORD SENSING MicroStrain, 2019).

Table 2.2

Inertial Measurement Unit (IMU) Sensor Characteristics

Parameter	Accelerometer	Gyroscope	Magnetometer
Measurement range	± 5 *g* (standard)	300°/sec (standard	± 2.5 Gauss
	± 16 *g* (option)	$\pm 75, \pm 150, \pm 900$ °/sec	
Resolution	<0.1 m*g*	<0.008°/sec	--
Initial bias error	± 0.002 *g*	± 0.05°/sec	± 0.003 Gauss
Noise density	100 µg/√Hz	0.005°/sec/√Hz	100 µGauss/√Hz
Alignment error	± 0.05°	± 0.05°	± 0.05°
Sampling rate	30kHZ	30kHZ	7.5 Khz max
IMU data output rate	1 Hz to 500 Hz		

   The 3DM-GX4-45™ IMU uses an RS232 serial communication to send its sensor

data to the PCM-3355. Its USB 2.0 (full speed) is used to power on it by connecting it to

the PCM-3355 onboard computer.

Figure 2.22 3DM-GX4-45™ by Lord MicroStrain® (LORD SENSING MicroStrain 2019).

2.6.3 Communication Hardware

A NanoBeam M5 16dBi is assembled into EASY (see Figure 2.23.). The implementation of this antenna allows the communication of the onboard PC/104 computer with a host computer. This antenna is also used to change the parameters of the controller (tuning of control gains) and to monitor any signal in real-time (Inc, 2019).

Figure 2.23 NanoBeam by Ubiquiti® (Inc, 2019).

A Polulu Mini Maestro 18 channels USB servo controller is used to send PWM signals to the servos. To establish serial communication between the Polulu servo controller and the onboard computer PC/104, a TTL to RS232 converter module is used (See Figure 2. 24).
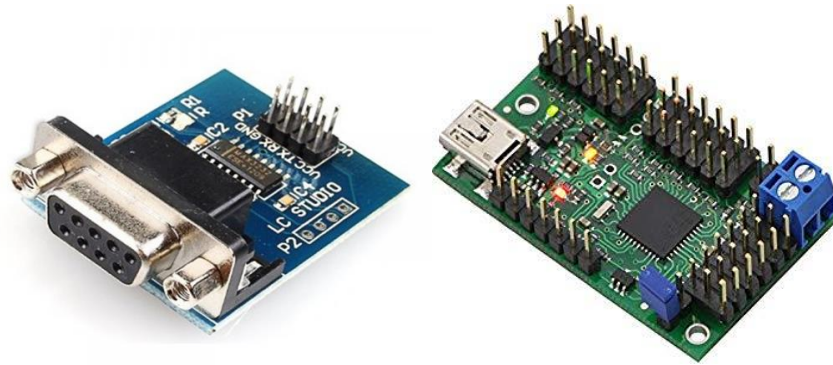
Figure 2.24 RS232 Serial Port to TTL Converter Module and Polulu Mini Servo Controller.

2.6.4 Power and Propulsion Hardware

As mentioned in the Electrical Power System description, two lithium-ion polymers (LiPo) battery are used to provide power to EASY (see Figure 2. 25.). The Turnigy® batteries of 22.4v/5.0 Amp and 14.8v/4.0 amp provide good performance and reliability.

Figure 2.25 5000mah 5s 20C and 4000mAh 4S 30C LiPo batteries by Turnigy®.

2.6.5 Integration Hardware

A general schematic of the connections between each hardware component is shown in Figure 2. 26. The red lines represent how the power is distributed to the components. Power source No. 1 provides power to the EASY's solenoid driver board, which also provides power to the 24 EASY's solenoids. Power source No. 2 provides power to the Polulu servo controller that then power the servos and the NanoBeam antenna. Finally, the EASY's IMU is powered directly from the PC/104 onboard computer.

Additionally, in Figure 2.26, the green, yellow and blue lines represent how the communication is handled between each of the components. The PC/104 onboard computer uses a serial protocol to receive the data coming from the IMU and also to send PWM commands to the Polulu servo controller. The PC/104 onboard computer is also interfaced with the EASY's solenoid driver through digital protocol communication. Finally, the Ethernet protocol allows the communication between the NanoBeam antenna and the PC/104 onboard computer. The NanoBeam antenna also receives information from the Host computer using Wireless.
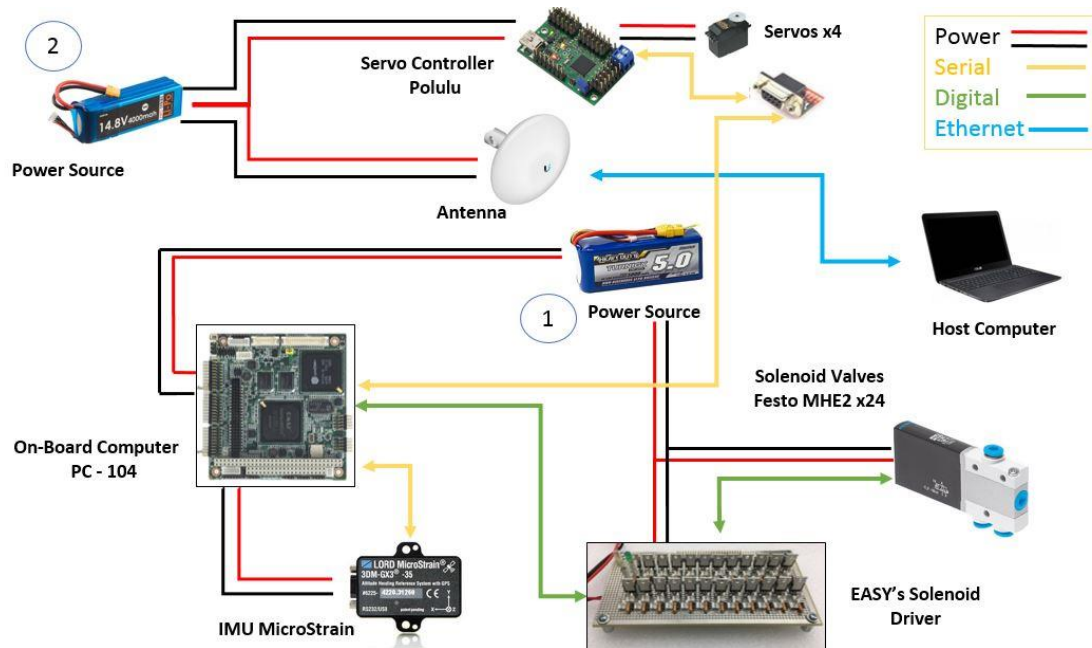
Figure 2.26 Power Distribution and Communication Setup.

2.7 Manufacture and Assembly

Manufacture and assembly of the vehicle were performed by considering the design described in previous sections. Due to simplicity, 60% of EASY's structure was built using a 3D printer of 5Th generation. For the remaining 40%, materials such as 3003 Aluminum honeycomb panel, carbon steel, carbon fiber, commercial steel and

commercial aluminum were used as shown in Figure 2.27. Figure 2.28 shows the final

assembly of EASY spacecraft mounted on a gimbal structure. The gimbal structure

provides the facility to have a rotation in the three axes.
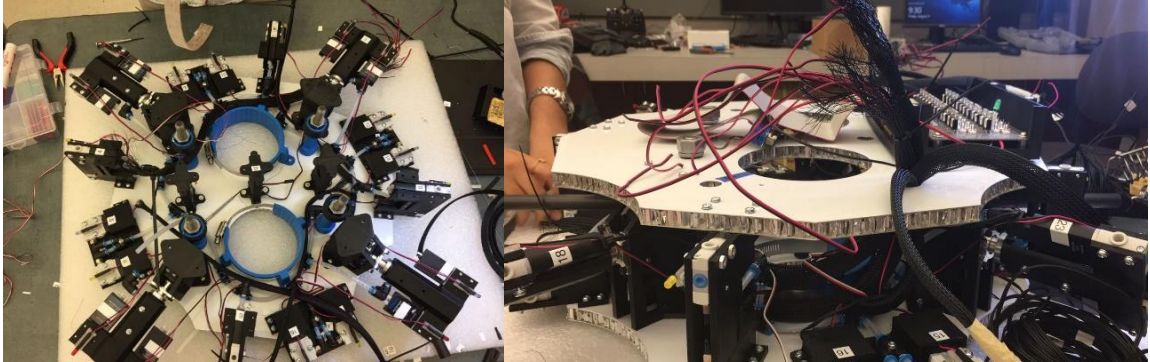
Figure 2.27 EASY's Building Process.
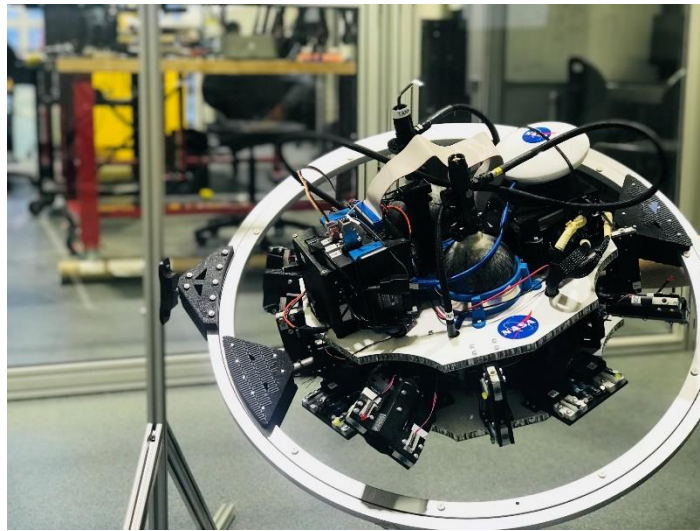
Figure 2.28 EASY Spacecraft.

3. EASY Model

This chapter provides a general description of the Spacecraft's dynamics and kinematics. This description will consider the role of quaternions and will assume that the spacecraft is a rigid body to obtain the rotational kinematics. With these considerations in mind, this section will focus on a set of key topics such as the determination of the frame and the implementation of quaternions with an explanation on its properties, rotational matrix quaternions, and Direction Cosine Matrix in Quaternion and Quaternion error. Other subsections will revolve around Attitude Quaternions Kinematics, Attitude Dynamics, Translational Dynamics, Rotational Dynamics, and Forces and Moments.

3.1 Determination of Frame

It is convenient for attitude analysis to define a body fixed reference frame B_f and an inertial reference frame I_f (Wie 2015), as shown in Figure 3. 1. Conventionally, a frame is defined by the orientation of its Cartesian axes and the location of its origin. The body fixed reference frame is usually tied to the actual vehicle where the origin of each coordinate is the center of mass of the body. This frame rotates with the body, thus providing the body's rotation state. An inertial reference frame instead is typically described as a frame that moves at a constant velocity but does not rotates with the body. In this manner, the attitude of any rigid body can be analyzed when a change occurs from an initial orientation to any other given orientation.
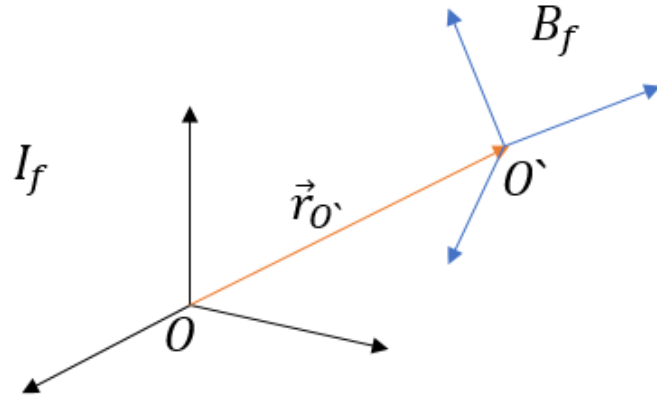
Figure 3.1 Rigid Body Reference Frame.

3.2 Quaternion Implementation

Spacecraft are required to perform fast maneuvers with rotations that are higher than 90 degrees. Using Euler representation of the rotations in the three axes represent a limitation for maneuvers that requires +/- 90 degrees rotation. This limitation is generated by a singularity in the Euler based Kinematic of rotation equations. This phenomenon known as Gimbal lock, can be resolved by using quaternions based representation of the rotations.

A quaternion is an ordered pair $\vec{q} = (q_0, \vec{q}_{1:3})$ represented with a vector $\vec{q}_{1:3} \in \mathbb{R}^3$ and a scalar part q_0 (Landis Markley & Crassidis, 2014), as denoted in Equation 3.1. Therefore, a vector quaternion part states to a quaternion with a zero-scalar component and a scalar quaternion part states to a quaternion with a zero-vector component.

$$\vec{q} = [q_0, q_1, q_2, q_3]^T \tag{3.1}$$

3.2.1 Properties of Quaternion

Some properties govern the quaternion; and a few are described as follows (Sidi, 1997):

A quaternion is defined as $q = q_0 + iq_1 + jq_2 + kq_3$ where q_1 , q_2 , and q_3 are real numbers. The symbols i , j and k obey the following relationships

$$i^2 = j^2 = k^2 = -1, \quad ij = k , ki = j , \quad jk = i , ji = -k , \quad kj = -i, \quad \text{and} \quad ik = -j .$$

1. The norm of quaternion should be a unit quaternion, which means its norm must be equal to 1, as shown in Equation 3.2.

$$q_0^2 + q_1^2 + q_2^2 + q_3^2 = 1$$

$$|q| = 1$$

(3.2)

2. The conjugate quaternion is equal to Equation 3.3

$$\vec{q}^{\,*} = q_0 - q_1 \mathrm{i} - q_2 \mathrm{j} - q_3 \mathrm{k}$$

(3.3)

3. The cross product of two quaternions is defined by Equation 3.4 (Landis Markley & Crassidis 2014):

$$\vec{q} \otimes \vec{q}_c = \begin{bmatrix} q_{0_c} \vec{q}_{1:3} + q_0 \vec{q}_{1:3_c} - \vec{q}_{1:3} \times \vec{q}_{1:3_c} \\ q_0 q_{0_c} - \vec{q}_{1:3} \cdot \vec{q}_{1:3_c} \end{bmatrix}$$

(3.4)

4. The dot product between two quaternions is defined by Equation 3.5 (Landis Markley & Crassidis 2014):

$$\vec{q} \odot \vec{q}_c = \begin{bmatrix} q_{0_c} \vec{q}_{1:3} + q_0 \vec{q}_{1:3_c} + \vec{q}_{1:3} \times \vec{q}_{1:3_c} \\ q_0 q_{0_c} - \vec{q}_{1:3} \cdot \vec{q}_{1:3_c} \end{bmatrix}$$

(3.5)

3.2.2 Rotational Matrix Quaternion

The rotational Matrix quaternions are represented, as shown in Equation 3.9. This matrix is obtained by considering the principal eigenvector or principal axis of rotation in Equation 3.6. where, α_r is the angle of rotation and $n_1, n_2, n_3,$ are the vector components of the principal axis of rotation $\vec{n}$.

$$\vec{q}_R = \begin{bmatrix} \cos\left(\dfrac{\alpha_r}{2}\right) \\ \sin\left(\dfrac{\alpha_r}{2}\right).n_1 \\ \sin\left(\dfrac{\alpha_r}{2}\right).n_2 \\ \sin\left(\dfrac{\alpha_r}{2}\right).n_3 \end{bmatrix} \tag{3.6}$$

Having a rotation order Z→ Y → X, the rotation matrix from Inertial reference frame to Body fixed reference frame using quaternions can be represented as:

$$R_{I_q}^B = \vec{q}_{R\psi} \cdot \vec{q}_{R\theta} \cdot \vec{q}_{R\phi} \tag{3.7}$$

where , $\vec{q}_{R\psi}$, $\vec{q}_{R\theta}$, and $\vec{q}_{R\phi}$ are the vector components of the rotational matrix with respect to the yaw, pitch and roll angles, respectively as defined in Equation 3.8.

$$\vec{q}_{R\psi} = \begin{bmatrix} \cos\left(\dfrac{\psi}{2}\right) \\ 0 \\ 0 \\ \sin\left(\dfrac{\psi}{2}\right) \end{bmatrix}, \; \vec{q}_{R\theta} = \begin{bmatrix} \cos\left(\dfrac{\theta}{2}\right) \\ 0 \\ \sin\left(\dfrac{\theta}{2}\right) \\ 0 \end{bmatrix}, \; \vec{q}_{R\phi} = \begin{bmatrix} \cos\left(\dfrac{\phi}{2}\right) \\ \sin\left(\dfrac{\phi}{2}\right) \\ 0 \\ 0 \end{bmatrix} \tag{3.8}$$

Applying the fifth property of quaternions shown in section 3.2.1, the Rotational Matrix from body fixed reference frame to inertial reference frame is as follow (Wie, 2015):

$$R_{I_q}^B = \begin{bmatrix} \cos\left(\dfrac{\psi}{2}\right)\cos\left(\dfrac{\theta}{2}\right)\cos\left(\dfrac{\phi}{2}\right)+\sin\left(\dfrac{\psi}{2}\right)\sin\left(\dfrac{\theta}{2}\right)\sin\left(\dfrac{\phi}{2}\right) \\ \cos\left(\dfrac{\psi}{2}\right)\cos\left(\dfrac{\theta}{2}\right)\sin\left(\dfrac{\phi}{2}\right)-\cos\left(\dfrac{\phi}{2}\right)\sin\left(\dfrac{\psi}{2}\right)\sin\left(\dfrac{\theta}{2}\right) \\ \cos\left(\dfrac{\phi}{2}\right)\cos\left(\dfrac{\psi}{2}\right)\sin\left(\dfrac{\theta}{2}\right)+\cos\left(\dfrac{\theta}{2}\right)\sin\left(\dfrac{\psi}{2}\right)\sin\left(\dfrac{\phi}{2}\right) \\ \cos\left(\dfrac{\phi}{2}\right)\cos\left(\dfrac{\theta}{2}\right)\sin\left(\dfrac{\psi}{2}\right)-\cos\left(\dfrac{\psi}{2}\right)\sin\left(\dfrac{\theta}{2}\right)\sin\left(\dfrac{\phi}{2}\right) \end{bmatrix} \tag{3.9}$$

3.2.3 Direction Cosine Matrix in Quaternions

The Rotational Matrix Quaternion provides the attitude angles in terms of quaternions, which now can be implemented to obtain the Direct Cosine Matrix (DCM) using transformations. To find a point P_2 relative to point P_1 with quaternion representation, Equation 3.10 is used.

$$P_2 = \vec{q} \cdot P_1 \cdot \vec{q}' \tag{3.10}$$

By using the property five from section 3.2.1, the Direct Cosine Matrix based on quaternions is obtained, as shown in Equation 3.11.

$$DCM_q = \begin{bmatrix} 1 - 2q_3{}^2 - 2q_2{}^2 & 2(q_1 q_2 - q_3 q_0) & 2(q_1 q_3 - q_2 q_0) \\ 2(q_1 q_2 + q_3 q_0) & 1 - 2q_3{}^2 - 2q_1{}^2 & 2(q_2 q_3 - q_1 q_0) \\ 2(q_1 q_3 - q_2 q_0) & 2(q_2 q_3 - q_1 q_0) & 1 - 2q_2{}^2 - 2q_1{}^2 \end{bmatrix} \tag{3.11}$$

Quaternion attitude representation can also be converted back to a Euler's angles attitude representation. In this case, it is recalled the well-known DCM. By obtaining the transpose of this DCM, it can be illustrated a rotation from a body fixed reference frame to the inertial reference frame, as shown in Equation 3.12.

$$DCM^T = R_B^I = \begin{bmatrix} \cos\theta\cos\psi & \sin\phi\sin\theta\cos\psi - \cos\phi\sin\psi & \cos\phi\sin\theta\cos\psi + \sin\phi\sin\psi \\ \sin\psi\cos\theta & \sin\phi\sin\theta\sin\psi + \cos\phi\cos\psi & \cos\psi\sin\theta\sin\psi - \sin\phi\cos\psi \\ -\sin\theta & \sin\phi\cos\theta & \cos\phi\cos\theta \end{bmatrix} \tag{3.12}$$

An extra positional row-column matrix DCM^* (see Equation 3.13) is used to correlate the DCM described in Equation 3.12 with the DCM quaternion based in Equation 3.11. Accordingly, to that correlation between those two DCM matrices, the attitude Euler's angles can be obtained using Equations 3.14, 3.15 and 3.16.

$$DCM^* = \begin{bmatrix} R_{11} & R_{12} & R_{13} \\ R_{21} & R_{22} & R_{23} \\ R_{31} & R_{32} & R_{33} \end{bmatrix} \tag{3.13}$$

$$\frac{R_{32}}{R_{33}} = \frac{\sin\phi\cos\theta}{\cos\phi\cos\theta} = \phi = \tan^{-1}\frac{2(q_2 q_3 + q_1 q_0)}{1 - 2q_2^2 q_3 - 2q_1^2} \tag{3.14}$$

$$R_{31} = \theta = a\sin\left[2(q_1 q_3 - q_2 q_0)\right] \tag{3.15}$$

$$\frac{R_{21}}{R_{11}} = \frac{\sin\psi\cos\theta}{\cos\phi\cos\psi} = \psi = \tan^{-1}\frac{2(q_1 q_2 + q_3 q_0)}{1 - 2q_3^2 q_3 - 2q_2^2} \tag{3.16}$$

3.3 Quaternion Error

Once quaternion is defined, the quaternion error between two quaternions can be obtained by the operation of a quaternion product as described in Equation 3.17. For control law purposes, one of the components of the quaternion error is assigned to be the desired Q_d and the remaining part is considered as the nominal (estimated).

$$q_e = Q_d \otimes \tilde{q}^{-1} \tag{3.17}$$

As shown in Equation 3.18, the quaternion desired Matrix Q_d can be described exactly in terms of desirable quaternion scalar, and desirable quaternion vector

$$Q_d = \begin{bmatrix} q_{3_d} & q_{2_d} & -q_{1_d} & -q_{0_d} \\ -q_{2_d} & q_{3_d} & q_{0_d} & -q_{1_d} \\ q_{1_d} & -q_{0_d} & q_{3_d} & -q_{2_d} \\ q_{0_d} & q_{1_d} & q_{2_d} & q_{3_d} \end{bmatrix} \tag{3.18}$$

By computing the quaternion error, the matrix defined in Equation 3.19 can be obtained.

$$q_e = \begin{bmatrix} q_{3_d}q_0 + q_{2_d}q_1 - q_{1_d}q_2 - q_{0_d}q_3 \\ -q_{2_d}q_0 + q_{3_d}q_1 + q_{0_d}q_2 - q_{1_d}q_3 \\ q_{1_d}q_0 - q_{0_d}q_1 + q_{3_d}q_2 - q_{2_d}q_3 \\ q_{0_d}q_0 + q_{1_d}q_1 + q_{2_d}q_2 + q_{3_d}q_3 \end{bmatrix} \tag{3.19}$$

3.4 Attitude Quaternion Kinematics

The relative orientation between the Inertial and the Body fixed reference frames from Section 3.1 can be described in terms of the angular velocity vector of the body

fixed reference frame with respect to the inertial reference frame. This angular velocity

vector time-dependent is defined as shown in Equation 3.20 (Wie, 2015).

$$\vec{\omega}_{B/I} = \vec{\omega}(t) = \begin{bmatrix} \omega_x \\ \omega_y \\ \omega_z \end{bmatrix} \tag{3.20}$$

Similar to Euler's angles attitude representation, a differential vector equation in

terms of quaternions can be written using the angular velocity vector (Sidi, 1997) from

Equation 3.20. These differential vector equations are known as the kinematic equations

for quaternions and are given by:

$$\dot{q} = \frac{1}{2}\Omega(\omega(t))\vec{q} \tag{3.21}$$

In Equation 3.21, $\Omega(\omega(t))$ is known as the kinematic quaternion matrix and it is

described as shown in Equation 3.22.

$$\Omega(\omega(t)) = \begin{bmatrix} 0 & -\omega_x & -\omega_y & -\omega_r \\ \omega_x & 0 & \omega_r & -\omega_y \\ \omega_y & -\omega_r & 0 & \omega_x \\ \omega_r & \omega_y & -\omega_x & 0 \end{bmatrix} \tag{3.22}$$

Equation 3.23 is a matrix form definition of equation 3.21.

$$\begin{bmatrix} \dot{q}_0 \\ \dot{q}_1 \\ \dot{q}_2 \\ \dot{q}_3 \end{bmatrix} = \frac{1}{2}\begin{bmatrix} 0 & -\omega_x & -\omega_y & -\omega_r \\ \omega_x & 0 & \omega_r & -\omega_y \\ \omega_y & -\omega_r & 0 & \omega_x \\ \omega_r & \omega_y & -\omega_x & 0 \end{bmatrix}\begin{bmatrix} q_0 \\ q_1 \\ q_2 \\ q_3 \end{bmatrix} \tag{3.23}$$

Taking the time derivative of Equation 3.17 and replacing it into Equation 3.21, the

quaternion error kinematics (Landis Markley & Crassidis, 2014) can be found as

shown in Equation 3.24. Where δq is the quaternion error.

$$\delta \dot{q} = \frac{1}{2}\Omega(\omega(t))\delta q \tag{3.24}$$

3.5 Attitude Dynamics

The rigid body assumption can be used to describe the vehicle motion based on position and velocity in the body fixed frame with respect to the inertial reference frame. Thus, the rigid body dynamics can be studied using to types of motion: translational and rotational:

3.5.1 Translational dynamics

In a rigid body system, the number of particles becomes infinite, and the mass of each particle becomes infinitesimal (De Ruiter Damaren & Forbes, 2013). Thus, the translational dynamics of the center of mass of a rigid body can be defined as:

$$m\ddot{\vec{r}}_c = \vec{F} \tag{3.25}$$

In Equation 3.25, $\vec{F}$ represents the total force on the body due to external forces, m the total mass of the system, and $\ddot{\vec{r}}$ the center of mass.

3.5.2 Rotational dynamics

The inertia matrix J is defined in the body fixed reference frame. J is real positive definite and symmetric matrix, where J_x, J_y, and J_z are called the principal moments of inertia as shown in Equation 3.26:

$$J = \begin{bmatrix} J_x & 0 & 0 \\ 0 & J_y & 0 \\ 0 & 0 & J_z \end{bmatrix} \tag{3.26}$$

In the rotational dynamics, the rotational velocity and the body's inertia is represented by the angular momentum vector and defined by Equation 3.27 as:

$$\vec{H} = J \cdot \vec{\omega} \tag{3.27}$$

Using the inertia matrix J from Equation 3.26, the angular velocity from Equation 3.20, and the angular momentum vector from Equation 3.27, the rotational equation of motion about its center of mass of a rigid body can be expressed as:

$$J\dot{\vec{\omega}} + \vec{\omega} \times J\vec{\omega} = \vec{M}(t)$$

$$\dot{\vec{\omega}} = J^{-1}\left[\vec{\omega} \times J\vec{\omega} + \vec{M}(t)\right]$$

$$(3.28)$$

Equation 3.28 is also called the Euler's rotational equation. From this equation, it can be obtained three nonlinear differential equations, which describe the rotational motion of a rigid body with three degrees of freedom, as shown in Equation 3.29

$$J_x\dot{\omega}_x + (J_z - J_y)\omega_y\omega_z = M_x$$

$$J_y\dot{\omega}_y + (J_x - J_z)\omega_x\omega_z = M_y \qquad (3.29)$$

$$J_z\dot{\omega}_z + (J_y - J_x)\omega_x\omega_y = M_z$$
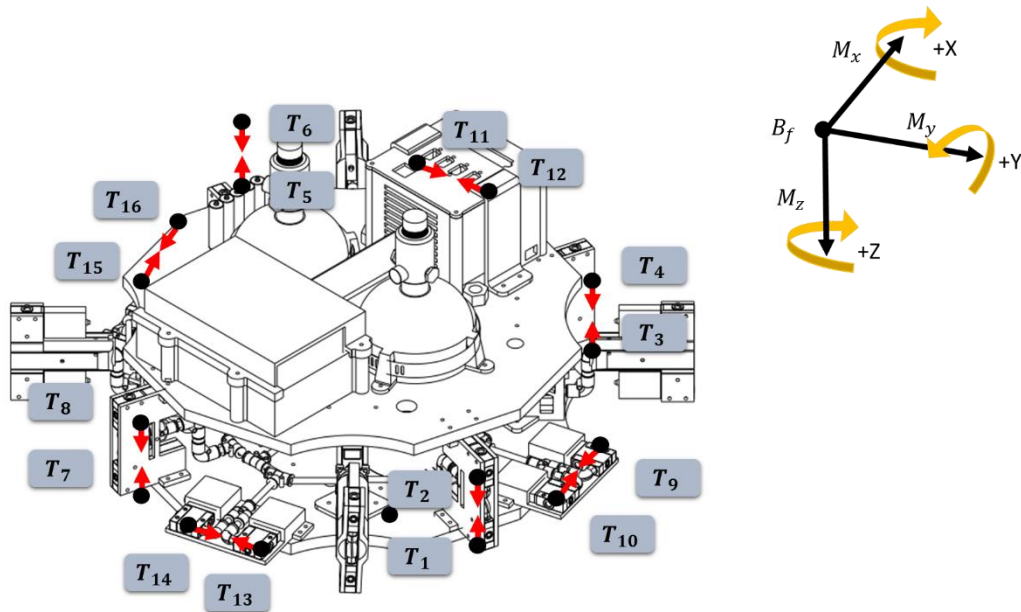
Figure 3.2 Forces and Moments EASY Spacecraft.

3.6 EASY Forces and Moments

In Chapter 2, the standard propulsion configuration system was described as a set of 16 Thrusters distributed uniformly around the X,Y, and Z axes of EASY spacecraft. Based on the mentioned actuator configuration, the diagram in Figure 3. 2 shows a general view of the forces and moments that act on the XYZ body fixed reference frame of EASY

Equation 3.30 describes the sum of forces generated by the thrusters in each individual axis. This set of forces is with respect to the center of gravity (CG) of EASY, as shown in Equations 3.31 through 3.35. Based on EASY's design, the orientation of 15 degrees in the yaw's thrusters location is taken into consideration.

$$\vec{F}(t) = \begin{bmatrix} \sum_{n=1}^{16} F_{nx} \\ \sum_{n=1}^{16} F_{ny} \\ \sum_{n=1}^{16} F_{nz} \end{bmatrix} \tag{3.30}$$

$$\vec{F}_1 = \begin{bmatrix} 0 \\ 0 \\ -T_1 \end{bmatrix} \quad \vec{F}_2 = \begin{bmatrix} 0 \\ 0 \\ T_2 \end{bmatrix} \quad \vec{F}_3 = \begin{bmatrix} 0 \\ 0 \\ -T_3 \end{bmatrix} \quad \vec{F}_4 = \begin{bmatrix} 0 \\ 0 \\ T_4 \end{bmatrix} \tag{3.31}$$

$$\vec{F}_5 = \begin{bmatrix} 0 \\ 0 \\ -T_5 \end{bmatrix} \quad \vec{F}_6 = \begin{bmatrix} 0 \\ 0 \\ T_6 \end{bmatrix} \quad \vec{F}_7 = \begin{bmatrix} 0 \\ 0 \\ -T_7 \end{bmatrix} \quad \vec{F}_8 = \begin{bmatrix} 0 \\ 0 \\ T_8 \end{bmatrix} \tag{3.32}$$

$$\vec{F}_9 = \begin{bmatrix} -\cos(15°)*T_9 \\ -\sin(15°)*T_9 \\ 0 \end{bmatrix} \quad \vec{F}_{10} = \begin{bmatrix} \cos(15°)*T_{10} \\ \sin(15°)*T_{10} \\ 0 \end{bmatrix} \quad \vec{F}_{11} = \begin{bmatrix} -\sin(15°)*T_{11} \\ \cos(15°)*T_{11} \\ 0 \end{bmatrix}$$

$$\vec{F}_{12} = \begin{bmatrix} \sin(15°)*T_{12} \\ -\cos(15°)*T_{12} \\ 0 \end{bmatrix} \tag{3.33}$$

$$\vec{F}_{13} = \begin{bmatrix} \sin(15^\circ)*T_{13} \\ -\cos(15^\circ)*T_{13} \\ 0 \end{bmatrix} \quad \vec{F}_{14} = \begin{bmatrix} -\sin(15^\circ)*T_{14} \\ +\cos(15^\circ)*T_{14} \\ 0 \end{bmatrix} \quad \vec{F}_{15} = \begin{bmatrix} \cos(15^\circ)*T_{15} \\ \sin(15^\circ)*T_{15} \\ 0 \end{bmatrix}$$

$$\vec{F}_{16} = \begin{bmatrix} -\cos(15^\circ)*T_{16} \\ -\sin(15^\circ)*T_{16} \\ 0 \end{bmatrix}$$

(3.34)

$$\sum \vec{F}_{EASY} = \begin{bmatrix} \cos(15^\circ)[-T_9+T_{10}+T_{15}-T_{16}]+\sin(15^\circ)[-T_{11}+T_{12}+T_{13}-T_{14}] \\ \sin(15^\circ)[-T_9+T_{10}+T_{15}-T_{16}]+\cos(15^\circ)[+T_{11}-T_{12}-T_{13}+T_{14}] \\ -[T_1+T_3+T_5+T_7]+[T_2+T_4+T_6+T_8] \end{bmatrix} = \begin{bmatrix} F_x \\ F_y \\ F_z \end{bmatrix}$$

(3.35)

The total moments produced by the thrusters in each of the axes with respect to the center of gravity is described in Equations 3.36 and 3.37. In these equations, L_x, L_y, and L_z correspond to the actual distance (X,Y and Z body fixed reference frame) of each thruster to the CG of the vehicle.

$$\vec{M}_{EASY} = \begin{bmatrix} \sum_{n=1}^{16} M_{nx} \\ \sum_{n=1}^{16} M_{ny} \\ \sum_{n=1}^{16} M_{nz} \end{bmatrix}$$

(3.36)

$$\sum \vec{M}_{EASY} = \begin{bmatrix} L_y[T_1+T_3+T_6+T_8]-L_y[T_2+T_4+T_5+T_7] \\ -L_x[T_1+T_7+T_4+T_6]+L_x[T_2+T_8+T_3+T_5] \\ L_z[T_9+T_{11}+T_{13}+T_{15}]-L_z[T_{10}+T_{12}+T_{14}+T_{16}] \end{bmatrix} = \begin{bmatrix} M_x \\ M_y \\ M_z \end{bmatrix}$$

(3.37)

4. Undesired Dynamics

Deviating from the desired flight path, losing control of the system, actuator saturation and increasing the fuel consumption are common errors directly related to the presence of undesired dynamics (or undesirable moments) acting on a space vehicle. The moments by itself depend on the forces generated by the vehicle's actuators (thrusters). The mentioned forces can change due to Thrust Misalignment Error and Thrust Magnitude Error (Hu, L,i Huo, & Shi, 2013). Thus, these two thrust errors become the two leading causes that could explain the generation of these undesirable dynamics.

Thrust Misalignment Error is defined by the tilt angle of the thrust vector from the nominal position. Misalignments can happen through different ways: inconsistencies in the nozzle geometry (disproportional roughness in the surface, bulges, out of round); out-of-position transient flows when starting or stopping; unequal deviations of the propulsion system or vehicle when containing a load; and inconsistencies in the gas flow (unequal burning rate in propellants, defective injector) (Sutton & Biblarz, 2010). Because of the deviation of the thrust vector, the attitude control and stability of the vehicle may be compromised (NASA, 1974). Difficulties may arise when the thrust axis of the propulsion system of a fixed nozzle is out of position. Even the misalignment of the high thrust engine system by an angle of less than 0.50 degrees can significantly affect the performance of the vehicle attitude. If this error is not minimized, the vehicle could fall or take a different direction (Sutton & Biblarz, 2010). The nozzle axis of the propulsion systems shall be aligned with precision to the aby vehicle so that the vehicle's compensating attitude control capability is not affected.

Also, a thrust magnitude error is mainly caused by increasing or decreasing the fuel mass at the thrusters (Dentis, Elisa & Guglieri, 2016). This kind of error is always tied to the failures that the propulsion system can suffer.

These two types of causes for undesired dynamics can be understood as uncertainties on the system and can be studied in decomposition in the controls area as unknown parameters. These unknown parameters are the misalignment angle and the error in the thrust magnitude, which are included as extra inputs of the system. A Mathematical Thrust Error (MTE) model is presented as the mathematical formulation used to study the behavior of these undesired dynamics in EASY spacecraft.

4.1 Mathematical Thrust Error (MTE) Model

The mathematical thrust error model introduced in this section is a general mathematical formulation of the total vector force of the system that considers the force calculation from each thruster under the presence of the thrust error caused by misalignment, and the thrust magnitude error already described. The total force is calculated by considering the fixed body reference frame (Lim & Bang, 2009). Thus, the total force for a given thruster is expressed as the sum of its thrust in nominal condition (no error), thrust with misalignment error, and thrust with magnitude error, as shown in Equation 4.1.

$$\vec{F}(t) = \begin{bmatrix} \sum_{n=1}^{16} F_{nx} \\ \sum_{n=1}^{16} F_{ny} \\ \sum_{n=1}^{16} F_{nz} \end{bmatrix} = \begin{bmatrix} \sum_{n=1}^{16} T_{nx_{Nom-condition}} + T_{nx_{with-misaligment-error}} + T_{nx_{with-magnitude-error}} \\ \sum_{n=1}^{16} T_{ny_{Nom-condition}} + T_{ny_{with-misaligment-error}} + T_{ny_{with-magnitude-error}} \\ \sum_{n=1}^{16} T_{nz_{Nom-condition}} + T_{nz_{with-misaligment-error}} + T_{nz_{with-magnitude-error}} \end{bmatrix} \qquad (4.1)$$

MTE model considers all kinds of misalignments in the positive and negative direction with respect to all of three axes. Two types of misalignments angles are defined: misalignment angle $\Delta\alpha$ denotes the angle at which the thrust force is located with respect to the X and Y axes; and misalignment angle $\Delta\beta$ refers to the angle at which the trust force is located with respect to the Z axis. Thrust magnitude error is defined as a function of time $\kappa(t)$ that directly affects the thrust in nominal condition. Equation 4.2 shows the force vector calculation for each of the thrusters based on Equation 4.1, and n represents the thruster number. In Equation 4.2, T_n is the desired thrust, $\vec{P}_{1x3}$ refers to the X, Y, and Z vector's components of the desired thrust without any error in consideration. The matrix $[M]_{3x2}$ correlates "sin" and "cos" angle's components of the thrust misalignment error in the X, Y and Z axes. Finally, the vector $\vec{E}_{2x1}$ describes the actual misalignment angle $\Delta\alpha$ and $\Delta\beta$.

$$\vec{F}_n = T_n\vec{P}_{1x3} + T_n[M]_{3x2}\vec{E}_{2x1} + (\kappa(t)T_n)\vec{P}_{1x3} \tag{4.2}$$

Within this MTE model, some assumptions are made, as shown in Equation 4.3.

$$\begin{aligned}
\cos(\Delta\alpha) &\approx \cos(\Delta\beta) \approx 1 \\
\sin(\Delta\alpha) &\approx \Delta\alpha \\
\sin(\Delta\beta) &\approx \Delta\beta \\
\Delta\alpha \cdot \Delta\beta &\approx \Delta\alpha \cdot \kappa(t) \approx \Delta\beta \cdot \kappa(t) \approx 0
\end{aligned} \tag{4.3}$$

Multiple configurations of misalignment angles can occur depending on the angle by itself and the axis from which the misalignment occurs. Due to the multiple configuration, a case of study is defined for EASY, and the mathematical thrust error model for this configuration is applied and presented through sections 4.2 and 4.3. This case of study includes the estimation of the total forces produced by each thruster using

the fixed body reference frame. Additionally, in Equation 4.4, some mathematical

identities that applied for this case of study are described.

$$\sin(\alpha + \beta) = \sin\alpha\cos\beta + \cos\alpha\sin\beta$$
$$\cos(\alpha + \beta) = \cos\alpha\cos\beta - \sin\alpha\sin\beta$$
$$\sin(\alpha - \beta) = \sin\alpha\cos\beta - \cos\alpha\sin\beta \tag{4.4}$$
$$\sin(\alpha - \beta) = \cos\alpha\cos\beta + \sin\alpha\sin\beta$$

4.2 MTE Model for Thrusters Associated with Pitch and Roll Maneuvers

In the development of the MTE model for thrusters involved in the performing of

pitch and roll maneuvers (thrusters 1 to 8), α and β angles are considered to be zero.

The consideration of these zero angles will keep the thrust force aligned with the Z axis

in a normal condition. On the other hand, the presence of misalignment angles will make

the thrust force to deviate from its initial alignment generating extra thrust force

components in the X, Y and Z axes. Figure 14 shows a graphical representation of

misalignment angles and thrust magnitude error.
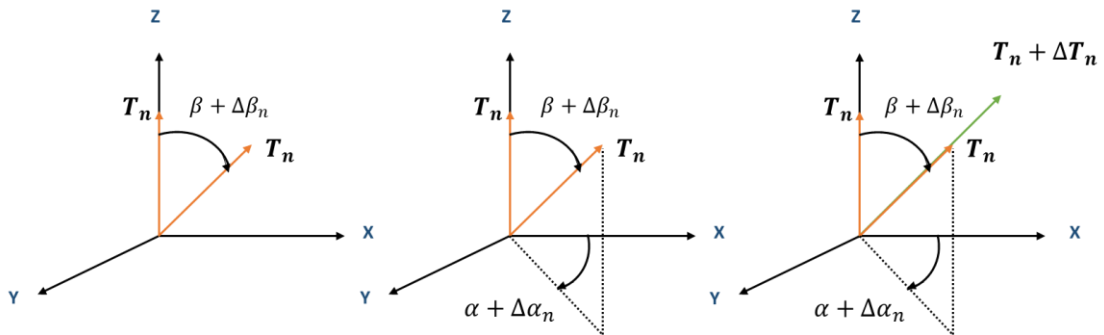
Figure 4.1 Generalized Graphical Representation of TMAE and TME for Pitch and Roll
Thrusters.

As an example, the derivations to calculte the total force for n given thrusters (1 to

8) is presented in Equation 4.5:

$$x_n = \left[\sin(\beta + \Delta\beta_n)\right]\left[\cos(\alpha + \Delta\alpha_n)\right]$$

$$x_n = \left[\sin(\beta)\cos(\Delta\beta_n) + \cos(\beta)\sin(\Delta\beta_n)\right]\left[\cos(\alpha)\cos(\Delta\alpha_n) - \sin(\alpha)\sin(\Delta\alpha_n)\right]$$

$$x_n = \left[\sin(\beta) + \cos(\beta)\Delta\beta_n\right]\left[\cos(\alpha) - \sin(\alpha)\Delta\alpha_n\right]$$

$$x_n = \left[\sin(\beta)\cos(\alpha) - \sin(\beta)\sin(\alpha)\Delta\alpha_n + \cos(\beta)\Delta\beta_n\cos(\alpha) - \cos(\beta)\Delta\beta_n\sin(\alpha)\Delta\alpha_n\right]$$

$$x_n = \left[\sin(\beta)\cos(\alpha) - \sin(\beta)\sin(\alpha)\Delta\alpha_n + \cos(\beta)\Delta\beta_n\cos(\alpha)\right]$$

$$y_n = \left[\sin(\beta + \Delta\beta_n)\right]\left[\sin(\alpha + \Delta\alpha_n)\right]$$

$$y_n = \left[\sin(\beta)\cos(\Delta\beta_n) + \cos(\beta)\sin(\Delta\beta_n)\right]\left[\sin(\alpha)\cos(\Delta\alpha_n) + \cos(\alpha)\sin(\Delta\alpha_n)\right] \quad (4.5)$$

$$y_n = \left[\sin(\beta) + \cos(\beta)\Delta\beta_n\right]\left[\sin(\alpha) + \cos(\alpha)\Delta\alpha_n\right]$$

$$y_n = \left[\sin(\beta)\sin(\alpha) + \sin(\beta)\cos(\alpha)\Delta\alpha_n + \cos(\beta)\Delta\beta_n\sin(\alpha) + \cos(\beta)\Delta\beta_n\cos(\alpha)\Delta\alpha_n\right]$$

$$y_n = \left[\sin(\beta)\sin(\alpha) + \sin(\beta)\cos(\alpha)\Delta\alpha_n + \cos(\beta)\Delta\beta_n\sin(\alpha)\right]$$

$$Z_n = \left[-\cos(\beta + \Delta\beta_n)\right]$$

$$Z_n = \left[-\cos(\beta)\cos(\Delta\beta_n) + \sin(\beta)\sin(\Delta\beta_n)\right]$$

$$Z_n = \left[-\cos(\beta) + \sin(\beta)\Delta\beta_n\right]$$

Figures 4.2 through 4.5 are also a graphical representation of misalignments angles and thrust magnitude error calculations for each of the considered thrusters. Equations 4.6 through 4.13 are the total force vector obtained for each of the mentioned thrusters.

Figure 4.2 Thruster No. 1 and 2 under TMAE and TME.

$$\vec{F}_{1_b} = T_1 \begin{bmatrix} \sin(\beta)\cos(\alpha) \\ -\sin(\beta)\sin(\alpha) \\ -\cos(\beta) \end{bmatrix} + T_1 \begin{bmatrix} \cos(\beta)\cos(\alpha) & -\sin(\beta)\sin(\alpha) \\ -\cos(\beta)\sin(\alpha) & -\sin(\beta)\cos(\alpha) \\ \sin(\beta) & 0 \end{bmatrix} \begin{bmatrix} \Delta\beta \\ \Delta\alpha \end{bmatrix} + T_1\kappa(t) \begin{bmatrix} \sin(\beta)\cos(\alpha) \\ -\sin(\beta)\sin(\alpha) \\ -\cos(\beta) \end{bmatrix} \quad (4.6)$$

$$\vec{F}_{2_b} = T_2 \begin{bmatrix} \sin(\beta)\cos(\alpha) \\ -\sin(\beta)\sin(\alpha) \\ \cos(\beta) \end{bmatrix} + T_2 \begin{bmatrix} \cos(\beta)\cos(\alpha) & -\sin(\beta)\sin(\alpha) \\ -\cos(\beta)\sin(\alpha) & -\sin(\beta)\cos(\alpha) \\ -\sin(\beta) & 0 \end{bmatrix} \begin{bmatrix} \Delta\beta \\ \Delta\alpha \end{bmatrix} + T_2\kappa(t) \begin{bmatrix} \sin(\beta)\cos(\alpha) \\ -\sin(\beta)\sin(\alpha) \\ \cos(\beta) \end{bmatrix} \quad (4.7)$$

$$\vec{F}_{3_b} = T_3 \begin{bmatrix} \sin(\beta)\cos(\alpha) \\ \sin(\beta)\sin(\alpha) \\ -\cos(\beta) \end{bmatrix} + T_3 \begin{bmatrix} \cos(\beta)\cos(\alpha) & -\sin(\beta)\sin(\alpha) \\ \cos(\beta)\sin(\alpha) & \sin(\beta)\cos(\alpha) \\ \sin(\beta) & 0 \end{bmatrix} \begin{bmatrix} \Delta\beta \\ \Delta\alpha \end{bmatrix} + T_3\kappa(t) \begin{bmatrix} \sin(\beta)\cos(\alpha) \\ \sin(\beta)\sin(\alpha) \\ -\cos(\beta) \end{bmatrix} \quad (4.8)$$

$$\vec{F}_{4_b} = T_4 \begin{bmatrix} \sin(\beta)\cos(\alpha) \\ \sin(\beta)\sin(\alpha) \\ \cos(\beta) \end{bmatrix} + T_4 \begin{bmatrix} \cos(\beta)\cos(\alpha) & -\sin(\beta)\sin(\alpha) \\ \cos(\beta)\sin(\alpha) & \sin(\beta)\cos(\alpha) \\ -\sin(\beta) & 0 \end{bmatrix} \begin{bmatrix} \Delta\beta \\ \Delta\alpha \end{bmatrix} + T_4\kappa(t) \begin{bmatrix} \sin(\beta)\cos(\alpha) \\ \sin(\beta)\sin(\alpha) \\ -\cos(\beta) \end{bmatrix} \quad (4.9)$$

Figure 4.3 Thruster No. 3 and 4 under TMAE and TME.
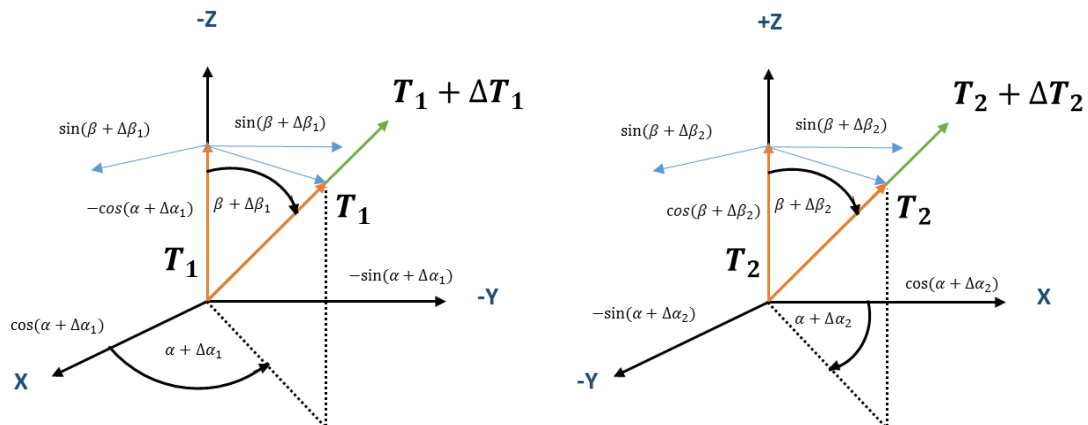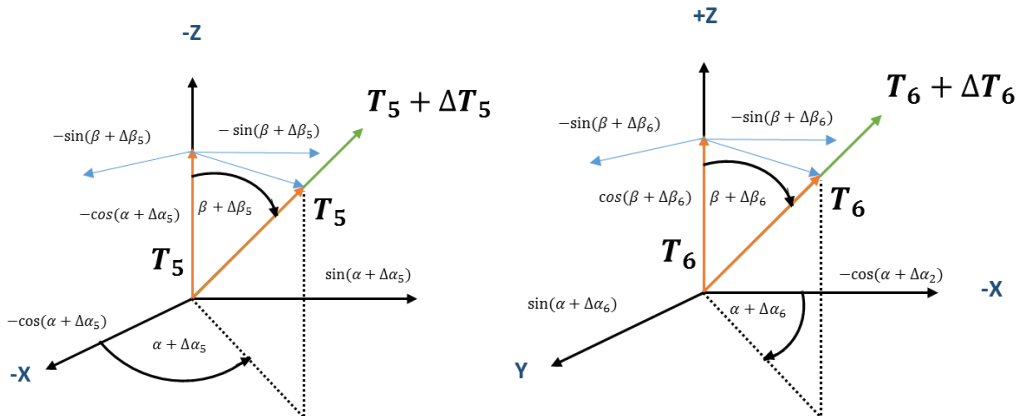

Figure 4.4. Thruster No. 5 and 6 under TMAE and TME.

Figure 4.5 Thruster No. 7 and 8 under TMAE and TME.

$$\vec{F}_{5_b} = T_5 \begin{bmatrix} \sin(\beta)\cos(\alpha) \\ -\sin(\beta)\sin(\alpha) \\ -\cos(\beta) \end{bmatrix} + T_5 \begin{bmatrix} \cos(\beta)\cos(\alpha) & -\sin(\beta)\sin(\alpha) \\ -\cos(\beta)\sin(\alpha) & -\sin(\beta)\cos(\alpha) \\ \sin(\beta) & 0 \end{bmatrix} \begin{bmatrix} \Delta\beta \\ \Delta\alpha \end{bmatrix} + T_5\kappa(t) \begin{bmatrix} \sin(\beta)\cos(\alpha) \\ -\sin(\beta)\sin(\alpha) \\ -\cos(\beta) \end{bmatrix} \qquad (4.10)$$

$$\vec{F}_{6_b} = T_6 \begin{bmatrix} \sin(\beta)\cos(\alpha) \\ -\sin(\beta)\sin(\alpha) \\ \cos(\beta) \end{bmatrix} + T_6 \begin{bmatrix} \cos(\beta)\cos(\alpha) & -\sin(\beta)\sin(\alpha) \\ -\cos(\beta)\sin(\alpha) & -\sin(\beta)\cos(\alpha) \\ -\sin(\beta) & 0 \end{bmatrix} \begin{bmatrix} \Delta\beta \\ \Delta\alpha \end{bmatrix} + T_6\kappa(t) \begin{bmatrix} \sin(\beta)\cos(\alpha) \\ -\sin(\beta)\sin(\alpha) \\ -\cos(\beta) \end{bmatrix} \qquad (4.11)$$

$$\vec{F}_{7_b} = T_7 \begin{bmatrix} \sin(\beta)\cos(\alpha) \\ \sin(\beta)\sin(\alpha) \\ -\cos(\beta) \end{bmatrix} + T_7 \begin{bmatrix} \cos(\beta)\cos(\alpha) & -\sin(\beta)\sin(\alpha) \\ \cos(\beta)\sin(\alpha) & \sin(\beta)\cos(\alpha) \\ \sin(\beta) & 0 \end{bmatrix} \begin{bmatrix} \Delta\beta \\ \Delta\alpha \end{bmatrix} + T_7\kappa(t) \begin{bmatrix} \sin(\beta)\cos(\alpha) \\ \sin(\beta)\sin(\alpha) \\ -\cos(\beta) \end{bmatrix} \qquad (4.12)$$

$$\vec{F}_{8_b} = T_8 \begin{bmatrix} \sin(\beta)\cos(\alpha) \\ \sin(\beta)\sin(\alpha) \\ \cos(\beta) \end{bmatrix} + T_8 \begin{bmatrix} \cos(\beta)\cos(\alpha) & -\sin(\beta)\sin(\alpha) \\ \cos(\beta)\sin(\alpha) & \sin(\beta)\cos(\alpha) \\ -\sin(\beta) & 0 \end{bmatrix} \begin{bmatrix} \Delta\beta \\ \Delta\alpha \end{bmatrix} + T_8\kappa(t) \begin{bmatrix} \sin(\beta)\cos(\alpha) \\ \sin(\beta)\sin(\alpha) \\ -\cos(\beta) \end{bmatrix} \qquad (4.13)$$

4.3 MTE Model for Thrusters Associated with Yaw Maneuvers

EASY'S mechanical standard configuration described in Chapter 3 considers the nominal position of the attitude thrusters for yaw motion with an inclination angle of 15 degrees with respect to the X and Y axes. Based on that inclination, α and β angles are considered to be 15 and zero degrees, respectively. Generalized graphical representation of misalignments angles and magnitude acting on yaw thrusters are shown in Figure 4.6.

Depending on the location of the yaw's thrusters around EASY spacecraft, α misalignment angle will be subtracted from the nominal one. This situation indicates that the misalignment is negative. Figures 4.7 through 4.10 shows graphical representation of thrusters 9 to 16 under misalignment and thrust magnitude error. Equations 4.14 through 4.21, represent the mathematical thrust error model for the already mentioned set of thrusters.
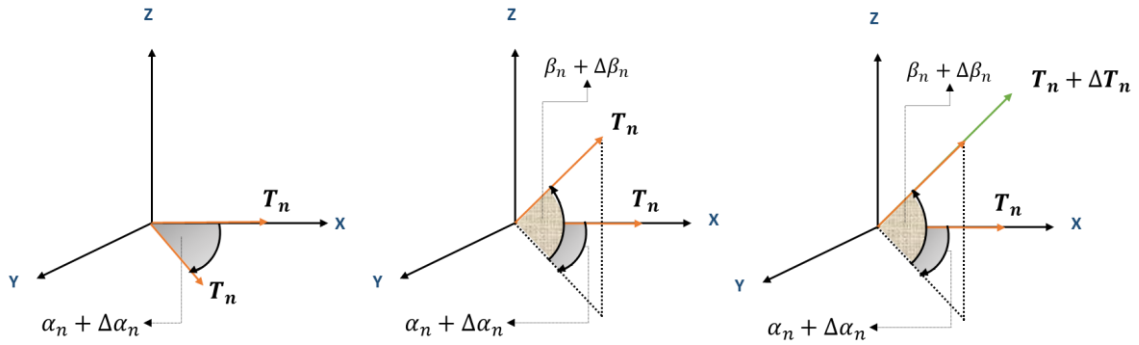
Figure 4.6 Generalized Graphical Representation of TMAE and TME for yaw thrusters.

Figure 4.7 Thruster No. 9 and 10 under TMAE and TME.

$$\vec{F}_{9_b} = T_9 \begin{bmatrix} \cos(\beta)\cos(\alpha) \\ \cos(\beta)\sin(\alpha) \\ -\sin(\beta) \end{bmatrix} + T_9 \begin{bmatrix} -\sin(\beta)\cos(\alpha) & -\cos(\beta)\sin(\alpha) \\ -\sin(\beta)\sin(\alpha) & \cos(\beta)\cos(\alpha) \\ -\cos(\beta) & 0 \end{bmatrix} \begin{bmatrix} \Delta\beta \\ \Delta\alpha \end{bmatrix} + T_9\kappa(t) \begin{bmatrix} \cos(\beta)\cos(\alpha) \\ \cos(\beta)\sin(\alpha) \\ -\sin(\beta) \end{bmatrix} \quad (4.14)$$
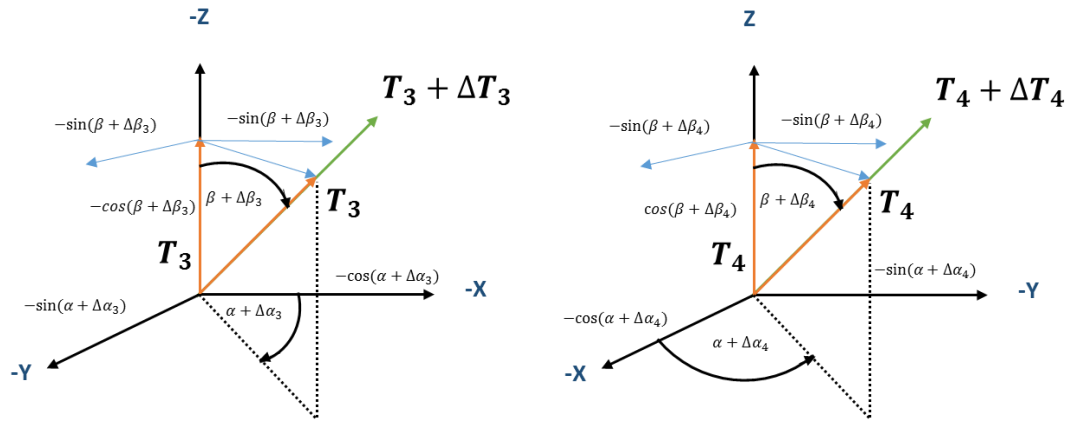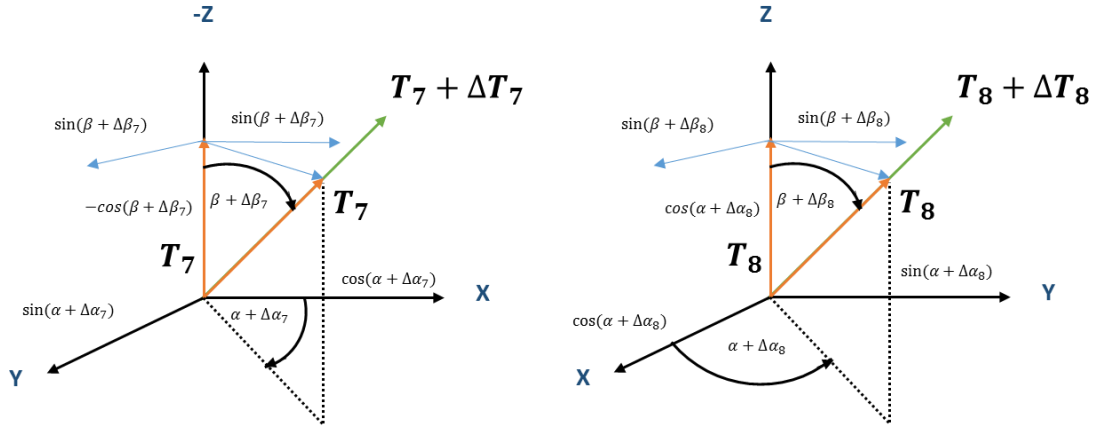
$$\vec{F}_{10_b} = T_{10} \begin{bmatrix} \cos(\beta)\cos(\alpha) \\ \cos(\beta)\sin(\alpha) \\ -\sin(\beta) \end{bmatrix} + T_{10} \begin{bmatrix} -\sin(\beta)\cos(\alpha) & \cos(\beta)\sin(\alpha) \\ -\sin(\beta)\sin(\alpha) & -\cos(\beta)\cos(\alpha) \\ -\cos(\beta) & 0 \end{bmatrix} \begin{bmatrix} \Delta\beta \\ \Delta\alpha \end{bmatrix} + T_{10}\kappa(t) \begin{bmatrix} \cos(\beta)\cos(\alpha) \\ \cos(\beta)\sin(\alpha) \\ -\sin(\beta) \end{bmatrix} \quad (4.15)$$
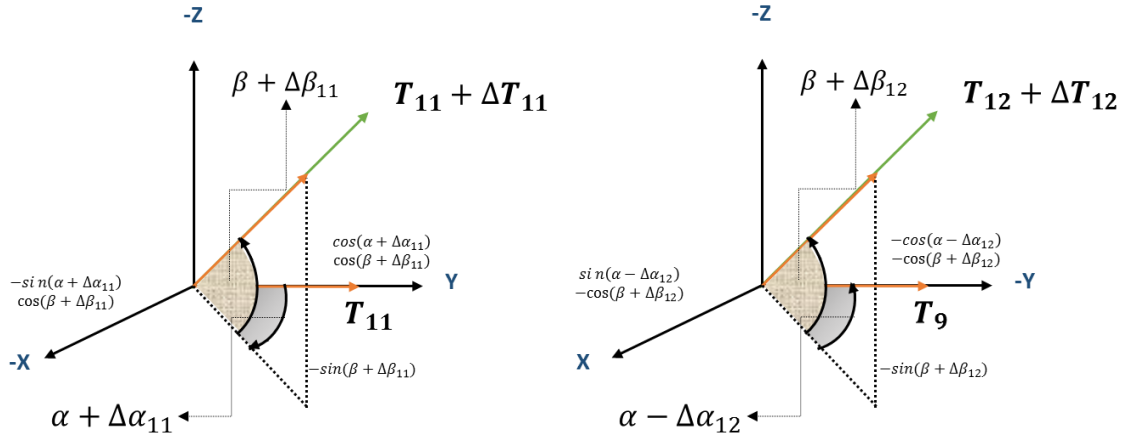
Figure 4.8 Thruster No. 11 and 12 under TMAE and TME.

$$\vec{F}_{11_b} = T_{11} \begin{bmatrix} -\cos(\beta)\sin(\alpha) \\ \cos(\beta)\cos(\alpha) \\ -\sin(\beta) \end{bmatrix} + T_{11} \begin{bmatrix} \sin(\beta)\sin(\alpha) & -\cos(\beta)\cos(\alpha) \\ -\sin(\beta)\cos(\alpha) & -\cos(\beta)\sin(\alpha) \\ -\cos(\beta) & 0 \end{bmatrix} \begin{bmatrix} \Delta\beta \\ \Delta\alpha \end{bmatrix} + T_{11}\kappa(t) \begin{bmatrix} -\cos(\beta)\sin(\alpha) \\ \cos(\beta)\cos(\alpha) \\ -\sin(\beta) \end{bmatrix} \quad (4.16)$$

$$\vec{F}_{12_b} = T_{12} \begin{bmatrix} -\cos(\beta)\sin(\alpha) \\ \cos(\beta)\cos(\alpha) \\ -\sin(\beta) \end{bmatrix} + T_{12} \begin{bmatrix} \sin(\beta)\sin(\alpha) & \cos(\beta)\cos(\alpha) \\ -\sin(\beta)\cos(\alpha) & -\cos(\beta)\sin(\alpha) \\ -\cos(\beta) & 0 \end{bmatrix} \begin{bmatrix} \Delta\beta \\ \Delta\alpha \end{bmatrix} + T_{12}\kappa(t) \begin{bmatrix} -\cos(\beta)\sin(\alpha) \\ \cos(\beta)\cos(\alpha) \\ -\sin(\beta) \end{bmatrix} \quad (4.17)$$
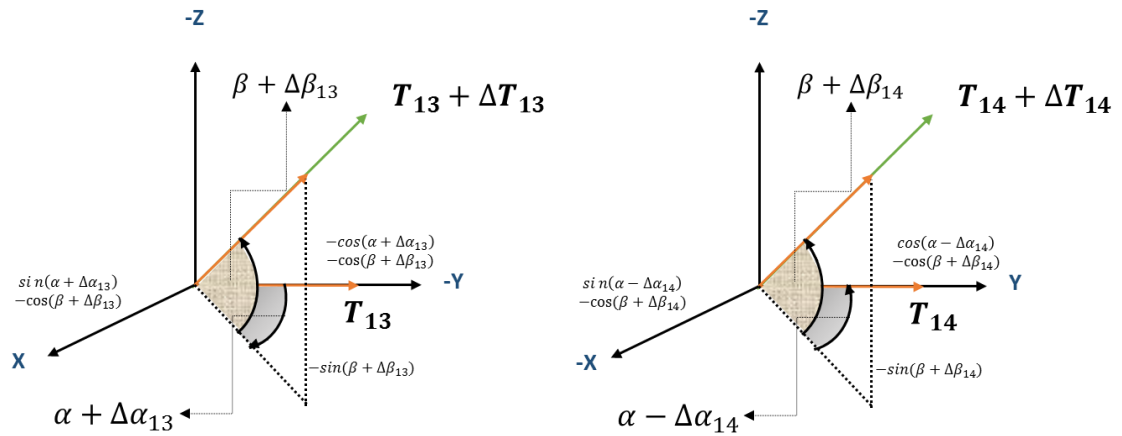
Figure 4.9 Thruster No. 13 and 14 under TMAE and TME.

$$\vec{F}_{13_b} = T_{13} \begin{bmatrix} -\cos(\beta)\sin(\alpha) \\ \cos(\beta)\cos(\alpha) \\ -\sin(\beta) \end{bmatrix} + T_{13} \begin{bmatrix} \sin(\beta)\sin(\alpha) & -\cos(\beta)\cos(\alpha) \\ \sin(\beta)\cos(\alpha) & -\cos(\beta)\sin(\alpha) \\ -\cos(\beta) & 0 \end{bmatrix} \begin{bmatrix} \Delta\beta \\ \Delta\alpha \end{bmatrix} + T_{13}\kappa(t) \begin{bmatrix} -\cos(\beta)\sin(\alpha) \\ \cos(\beta)\cos(\alpha) \\ -\sin(\beta) \end{bmatrix} \quad (4.18)$$

$$\vec{F}_{14_b} = T_{14} \begin{bmatrix} -\cos(\beta)\sin(\alpha) \\ \cos(\beta)\cos(\alpha) \\ -\sin(\beta) \end{bmatrix} + T_{14} \begin{bmatrix} \sin(\beta)\sin(\alpha) & \cos(\beta)\cos(\alpha) \\ -\sin(\beta)\cos(\alpha) & \cos(\beta)\sin(\alpha) \\ -\cos(\beta) & 0 \end{bmatrix} \begin{bmatrix} \Delta\beta \\ \Delta\alpha \end{bmatrix} + T_{14}\kappa(t) \begin{bmatrix} -\cos(\beta)\sin(\alpha) \\ \cos(\beta)\cos(\alpha) \\ -\sin(\beta) \end{bmatrix} \quad (4.19)$$
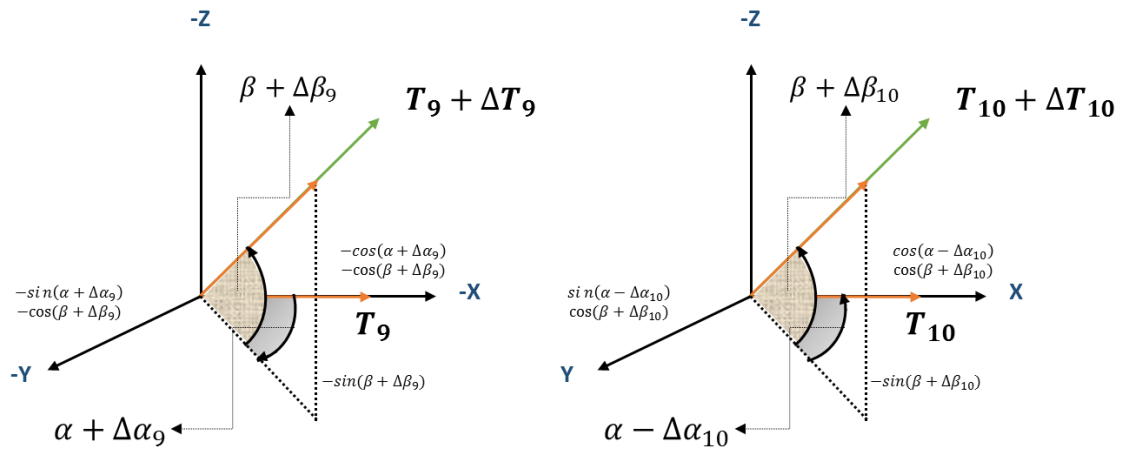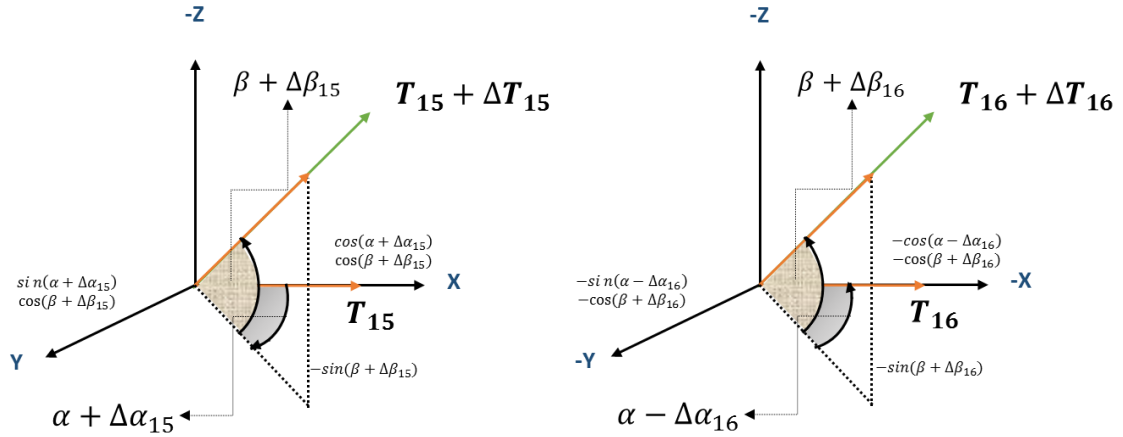

Figure 4.10 Thruster No. 15 and 16 under TMAE and TME.

$$\vec{F}_{15_b} = T_{15} \begin{bmatrix} \cos(\beta)\cos(\alpha) \\ \cos(\beta)\sin(\alpha) \\ -\sin(\beta) \end{bmatrix} + T_{15} \begin{bmatrix} -\sin(\beta)\cos(\alpha) & -\cos(\beta)\sin(\alpha) \\ -\sin(\beta)\sin(\alpha) & \cos(\beta)\cos(\alpha) \\ -\cos(\beta) & 0 \end{bmatrix} \begin{bmatrix} \Delta\beta \\ \Delta\alpha \end{bmatrix} + T_{15}\kappa(t) \begin{bmatrix} \cos(\beta)\cos(\alpha) \\ \cos(\beta)\sin(\alpha) \\ -\sin(\beta) \end{bmatrix} \quad (4.20)$$

$$\vec{F}_{16_b} = T_{16} \begin{bmatrix} \cos(\beta)\cos(\alpha) \\ \cos(\beta)\sin(\alpha) \\ -\sin(\beta) \end{bmatrix} + T_{16} \begin{bmatrix} -\sin(\beta)\cos(\alpha) & \cos(\beta)\sin(\alpha) \\ -\sin(\beta)\sin(\alpha) & -\cos(\beta)\cos(\alpha) \\ -\cos(\beta) & 0 \end{bmatrix} \begin{bmatrix} \Delta\beta \\ \Delta\alpha \end{bmatrix} + T_{16}\kappa(t) \begin{bmatrix} \cos(\beta)\cos(\alpha) \\ \cos(\beta)\sin(\alpha) \\ -\sin(\beta) \end{bmatrix} \quad (4.21)$$

# 5. Control Laws Design and Development

A full nonlinear (time-invariant) spacecraft attitude motion can be defined using

Equations 5.1 and 5.2, where $\dot{\vec{x}}(t)$ and $y(t)$ are called state equation and measurement

equation, respectively. The vector function $\vec{f}$ and $\vec{h}$ are dependent of $\vec{x}(t)$ (state vector),

$\vec{u}(t)$ (input vector) and t (time).

$$\dot{\vec{x}}(t) = \vec{f}\left(\vec{x}(t), \vec{u}(t)\right) \tag{5.1}$$

$$y(t) = \vec{h}\left(\vec{x}(t), \vec{u}(t)\right) \tag{5.2}$$

The state vector $\vec{x} \in \Re^{7x1}$ can be defined as shown in Equation 5.3. Where ω_x, ω_y and

ω_z are the angular velocities and $\delta q_0, \delta q_1, \delta q_2$ and δq_3 are the quaternion error.

$$\vec{x} = \left[\omega_x, \omega_y, \omega_z, \delta q_0, \delta q_1, \delta q_2, \delta q_3\right]^T \tag{5.3}$$

The input vector defined in Equation 5.4 contains the moments M_x, M_y and M_z

acting on the vehicle.

$$\vec{u} = \vec{M}(t) = \left[M_x, M_y, M_z\right]^T \tag{5.4}$$

Using Equations 3.24, 3.28, 5.3, and 5.4, the state equation from 5.1 can be expanded

into a state-space form as shown in Equation 5.5:

$$\dot{\vec{x}}(t) = \vec{f}\left(\vec{x}(t), \vec{u}(t)\right) = \begin{bmatrix} \dot{\vec{\omega}} \\ \delta\dot{q}_e \end{bmatrix} = \begin{bmatrix} J^{-1}\left[\vec{\omega} \times J\vec{\omega}\right] \\ \frac{1}{2}\Omega(\omega(t))\vec{q} \end{bmatrix} + \begin{bmatrix} J^{-1} \\ [0]_{4x3} \end{bmatrix} \begin{bmatrix} M_x(t) \\ M_y(t) \\ M_z(t) \end{bmatrix} \tag{5.5}$$

5.1 Quaternion Feedback Linearization Based Controller

A quaternion feedback linearization based controller was designed and developed,

and a general description is provided in this chapter. The goal of this controller is to

provide regulation control by driving the actual quaternions to the desired states and the

angular velocities to zero (Landis, Markley & Crassidis, 2014). By means of, quaternions

at the desired states is understandable that the actual attitude has been driven to the

desired fixed location (in the body fixed reference frame) by producing a sequence of

rotations. This process involves the implementation of a quaternion error operator, as

shown in Equation 3.17.

The designed controller is based on a feedback linearization of the angular rotational

dynamics of Equations 3.28. Equation 5.6 represents the control laws for this system,

where $u_v(q,\omega)$ is considered to be a time-invariant virtual controller (Wie & Barba, 1985).

$$\vec{M}(t) = u_{NLDI}(t) = \left[\vec{\omega} \times J\vec{\omega}\right] + J u_v(q,\omega) \tag{5.6}$$

The virtual controller $u_v(q,\omega)$ is defined by the multiplication between $K_{\omega q}$ (control

gain matrices) and $\delta\vec{\omega}, \delta\vec{q}$ vectors (angular velocity and quaternion errors), as shown in

Equation 5.7. The implemntation of this virtual control will stabilize the system.

$$u_v(q,\omega) = -K_{\omega q}\left[\delta\vec{\omega}, \delta\vec{q}\right]^T \tag{5.7}$$

By incorporating Equation 5.7 into Equation 5.6 the new control law shown in

Equation 5.8 is obtained.

$$\vec{M}(t) = u_{NLDI}(t) = \left[\vec{\omega} \times J\vec{\omega}\right] + J\left(-K_{\omega q}\left[\delta\vec{\omega}, \delta\vec{q}\right]^T\right) \tag{5.8}$$

The system presented in Equation 5.5 is modified by the new control law introduced

in Equation 5.8. Equation 5.9 describes the close loop system. However, the presence of

quaternions kinematics makes the system to remain nonlinear:

$$\dot{\vec{x}}(t) = \vec{f}\left(\vec{x}(t), \vec{u}(t)\right) = \begin{bmatrix} \dot{\omega} \\ \delta\dot{q}_e \end{bmatrix} = \begin{bmatrix} -K_{\omega q}\left[\delta\vec{\omega}, \delta\vec{q}\right]^T \\ \frac{1}{2}\Omega(\omega(t))\vec{q} \end{bmatrix} + \begin{bmatrix} J^{-1} \\ [0]_{4x3} \end{bmatrix}\begin{bmatrix} M_x(t) \\ M_y(t) \\ M_z(t) \end{bmatrix} \tag{5.9}$$

To overcome this nonlinearity, a linearization is made with respect to an equilibrium point of $\vec{x}$ shown in Equation 5.10:

$$\vec{x} = [0,0,0,1,0,0,0]^T \tag{5.10}$$

Given the equilibrium point, the linearization of the system is accomplished by introducing the Jacobian matrix calculation. The mathematical determination of a Jacobian matrix is performed based on the partial derivatives of a set of functions $f_n(x,t)$ with respect to the state vector shown in Equation 5.3. Equations 5.11 through 5.17 are the set of functions used to obtain the Jacobian matrix.

$$f_1(x,t) = \dot{\omega}_x = -K_{\omega_x}\omega_x - K_{q_1}\delta q_1 \tag{5.11}$$

$$f_2(x,t) = \dot{\omega}_y = -K_{\omega_y}\omega_y - K_{q_2}\delta q_2 \tag{5.12}$$

$$f_3(x,t) = \dot{\omega}_z = -K_{\omega_z}\omega_z - K_{q_3}\delta q_3 \tag{5.13}$$

$$f_4(x,t) = \delta \dot{q}_1 = \frac{1}{2}\left(\omega_x\delta q_0 + \omega_z\delta q_2 - \omega_y\delta q_3\right) \tag{5.14}$$

$$f_5(x,t) = \delta \dot{q}_2 = \frac{1}{2}\left(\omega_y\delta q_0 + \omega_x\delta q_3 - \omega_z\delta q_1\right) \tag{5.15}$$

$$f_6(x,t) = \delta \dot{q}_3 = \frac{1}{2}\left(\omega_z\delta q_0 + \omega_y\delta q_1 - \omega_x\delta q_2\right) \tag{5.16}$$

$$f_7(x,t) = \delta \dot{q}_0 = -\frac{1}{2}\left(\omega_x\delta q_1 + \omega_y\delta q_2 + \omega_z\delta q_3\right) \tag{5.17}$$

Equation 5.18 shows an example of the calculation of the jacobian matrices A and B.

$$A = \left[\frac{\partial \vec{f}}{\partial \vec{x}}\right]_{(X_1,X_2)} = \begin{bmatrix} \partial f_1/\partial x_1 & . & \partial f_1/x_n \\ . & . & . \\ \partial f_n/\partial x_1 & . & \partial f_n/x_n \end{bmatrix}_{(X_1,X_2)} \quad B = \left[\frac{\partial \vec{f}}{\partial \vec{u}}\right]_{(X_1,X_2)} = \begin{bmatrix} \partial f_1/\partial u_1 & . & \partial f_1/u_m \\ . & . & . \\ \partial f_n/\partial u_1 & . & \partial f_n/u_m \end{bmatrix}_{(X_1,X_2)} \tag{5.18}$$

Following Equation 5.18, the closed loop matrix $\tilde{A}$ in Equation 5.19 can be obtained. This closed-loop $\tilde{A}$ matrix contains an eigenvalue related to the quaternion's scalar part,

which cannot be controllable. To deal with the uncontrollable eigenvalue, the quaternion's scalar part can be excluded from the state vector in Equation 5.10. In the same way, from the quaternions error kinematics, the scalar part $\delta\dot{q}_0$ is omitted. This process leads to a reduction of the closed-loop $\tilde{A}$ matrix's size to a 6x6 matrix, which contains only 6 states, 3 inputs, and 3 quaternions to be controlled.

$$\tilde{A} = \begin{bmatrix} -K_{\omega_x} & 0 & 0 & -K_{q_1} & 0 & 0 & 0 \\ 0 & -K_{\omega_y} & 0 & 0 & -K_{q_2} & 0 & 0 \\ 0 & 0 & -K_{\omega_z} & 0 & 0 & -K_{q_3} & 0 \\ 0 & 0 & 0 & 0 & 0 & 0 & 0 \\ 0.5 & 0 & 0 & 0 & 0 & 0 & 0 \\ 0 & 0.5 & 0 & 0 & 0 & 0 & 0 \\ 0 & 0 & 0.5 & 0 & 0 & 0 & 0 \end{bmatrix} \tag{5.19}$$

The states space form of the system yields:

$$\dot{\vec{x}} = \tilde{A}\vec{x} + \tilde{B}\vec{u}$$
$$y = \tilde{C}\vec{x} + \tilde{D}\vec{u} \tag{5.20}$$

$$\begin{bmatrix} \dot{\omega}_x \\ \dot{\omega}_y \\ \dot{\omega}_z \\ \delta\dot{q}_1 \\ \delta\dot{q}_2 \\ \delta\dot{q}_3 \end{bmatrix} = \begin{bmatrix} K_{\omega_x} & 0 & 0 & K_{q_1} & 0 & 0 \\ 0 & K_{\omega_y} & 0 & 0 & K_{q_2} & 0 \\ 0 & 0 & K_{\omega_z} & 0 & 0 & K_{q_3} \\ 0.5 & 0 & 0 & 0 & 0 & 0 \\ 0 & 0.5 & 0 & 0 & 0 & 0 \\ 0 & 0 & 0.5 & 0 & 0 & 0 \end{bmatrix} \begin{bmatrix} \omega_x \\ \omega_y \\ \omega_z \\ \delta q_1 \\ \delta q_2 \\ \delta q_3 \end{bmatrix} + \begin{bmatrix} \frac{1}{I_{xx}} & 0 & 0 \\ 0 & \frac{1}{I_{yy}} & 0 \\ 0 & 0 & \frac{1}{I_{zz}} \\ 0 & 0 & 0 \\ 0 & 0 & 0 \\ 0 & 0 & 0 \end{bmatrix} \begin{bmatrix} M_x \\ M_y \\ M_z \end{bmatrix} \tag{5.21}$$

$$y = \begin{bmatrix} 1 & 0 & 0 & 0 & 0 & 0 \\ 0 & 1 & 0 & 0 & 0 & 0 \\ 0 & 0 & 1 & 0 & 0 & 0 \\ 0 & 0 & 0 & 1 & 0 & 0 \\ 0 & 0 & 0 & 0 & 1 & 0 \\ 0 & 0 & 0 & 0 & 0 & 1 \end{bmatrix} \begin{bmatrix} \omega_x \\ \omega_y \\ \omega_z \\ \delta q_1 \\ \delta q_2 \\ \delta q_3 \end{bmatrix} + \begin{bmatrix} 0 & 0 & 0 \\ 0 & 0 & 0 \\ 0 & 0 & 0 \\ 0 & 0 & 0 \\ 0 & 0 & 0 \\ 0 & 0 & 0 \end{bmatrix} \begin{bmatrix} M_x \\ M_y \\ M_z \end{bmatrix} \tag{5.22}$$

Using the closed-loop $\tilde{A}$ matrix from Equation 5.21, the polynomial characteristic equation can be found as defined in Equations 5.23 through 5.26:

$$p(\lambda) = \det(\lambda I - A) = \lambda^n + a_{n-1}\lambda^{n-1} + a_1\lambda + a_0 \tag{5.23}$$

$$p(\lambda) = \det(\lambda I - A) = \det\begin{bmatrix} \lambda - K_{\omega_x} & 0 & 0 & -K_{q_1} & 0 & 0 \\ 0 & \lambda - K_{\omega_y} & 0 & 0 & -K_{q_2} & 0 \\ 0 & 0 & \lambda - K_{\omega_z} & 0 & 0 & -K_{q_3} \\ -0.5 & 0 & 0 & \lambda & 0 & 0 \\ 0 & -0.5 & 0 & 0 & \lambda & 0 \\ 0 & 0 & -0.5 & 0 & 0 & \lambda \end{bmatrix} \tag{5.24}$$

$$p(\lambda) = \frac{\left(2\lambda^2 + 2K_{\omega_x}\lambda + K_{q_1}\right)\left(2\lambda^2 + 2K_{\omega_y}\lambda + K_{q_2}\right)\left(2\lambda^2 + 2K_{\omega_z}\lambda + K_{q_3}\right)}{8} = 0 \tag{5.25}$$

$$p(\lambda) = \left(\lambda^2 + K_{\omega_x}\lambda + \frac{K_{q_1}}{2}\right)\left(\lambda^2 + K_{\omega_y}\lambda + \frac{K_{q_2}}{2}\right)\left(\lambda^2 + K_{\omega_z}\lambda + \frac{K_{q_3}}{2}\right) = 0 \tag{5.26}$$

To find the control gains K_{ω_x}, K_{ω_y}, K_{ω_z}, K_{q_1}, K_{q_2}, and K_{q_3}, the obtained polynomial

characteristic equation from Equation 5.26 is directly compared to a desired polynomial

characteristic equation introduced in Equation 5.27.

$$p(\lambda) = \left(\lambda^2 + 2\zeta_x\omega_x\lambda + \omega_x^2\right)\left(\lambda^2 + 2\zeta_y\omega_y\lambda + \omega_y^2\right)\left(\lambda^2 + 2\zeta_z\omega_z\lambda + \omega_z^2\right) = 0 \tag{5.27}$$

The direct comparison between the two polynomial characteristic equations yields

the definition of control gains, as shown in Equations 5.28 through 5.33, where $\zeta_{x,y,x}$ and

$\omega_{x,y,z}$ are desirable damping ratio and natural frequency.

$$K_{\omega_x}\lambda = 2\zeta_x\omega_x\lambda \rightarrow K_{\omega_x} = 2\zeta_x\omega_x \tag{5.28}$$

$$K_{\omega_y}\lambda = 2\zeta_y\omega_y\lambda \rightarrow K_{\omega_y} = 2\zeta_y\omega_y \tag{5.29}$$

$$K_{\omega_z}\lambda = 2\zeta_z\omega_z\lambda \rightarrow K_{\omega_z} = 2\zeta_z\omega_z \tag{5.30}$$

$$\frac{K_{q_1}}{2} = \omega_x^2 \rightarrow K_{q_1} = 2\omega_x^2 \tag{5.31}$$

$$\frac{K_{q_2}}{2} = \omega_y^2 \rightarrow K_{q_2} = 2\omega_y^2 \tag{5.32}$$

$$\frac{K_{q_3}}{2} = \omega_z^2 \rightarrow K_{q_3} = 2\omega_z^2 \tag{5.33}$$

The desired damping ratio and natural frequency for each of the control gains described before can be calculated using Equations 5.34 and 5.35.

$$\zeta_{x,y,z} = \sqrt{\frac{\left(\ln\frac{PO}{100\%}\right)^2}{\pi^2 + \left(\ln\frac{PO}{100\%}\right)^2}} \tag{5.34}$$

$$\omega_{n:x,y,z} = \frac{2\tau}{4\zeta_{x,y,z}} \tag{5.35}$$

After obtaining the control gains $K_{\omega q}$, the virtual controller, $u_v(q,\omega)$ of the control law control system described in Equation 5.8, can be updated, as shown in Equation 5.36.

$$\vec{M}(t) = u_{NLDI}(t) = \left[\vec{\omega} \times J\vec{\omega}\right] + J\left(-K_{\omega q}\left[\delta\vec{\omega}, \delta\vec{q}\right]^T\right) \tag{5.36}$$

The control law described in Equation 5.36 ensures the stabilization of the system to the desired attitude quaternions. However, it does not provide the shortest path to achieve the final orientation. To solve this problem, Equations 5.37 includes a modification to the quaternion scalar part into the virtual controller (Landis Markley & Crassidis 2014).This modification takes into consideration the sing of the scalar quaternion part.

$$\vec{M}(t) = u_{NLDI}(t) = \left[\vec{\omega} \times J\vec{\omega}\right] + J\left(-K_q sign\left(\delta q_0\right)\left(\delta\vec{q}_{1:3}\right) - K_\omega \vec{\omega}\right) \tag{5.37}$$

A general schematic of the discussed controller is shown in Figure 5.1. This schematic includes the control law considered as a Inner Loop Controller, a control allocation form for EASY spacecraft, EASY Dynamics and a representation of an XA 6DOF simulation discussed in Chapter 6.
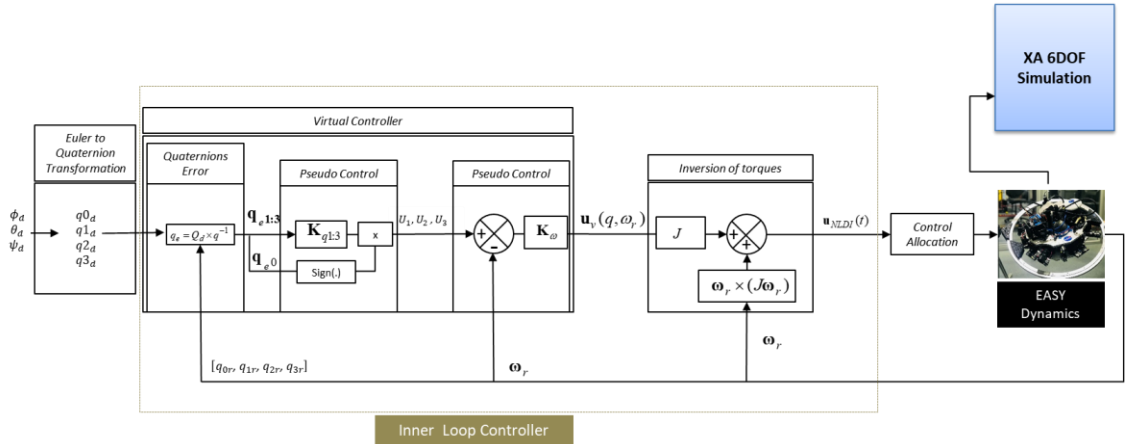
Figure 5.1 Control Law Schematic of Quaternion Feedback Linearization Based Controller.

5.2 Control Allocation

As previously mentioned in Chapter 2, there are 12 thrusters for nominal

configuration. In chapter 3, the forces and moments equations that acted on EASY

spacecraft were presented in Equation 3.32 and 3.34. However, the solution of those

equations to find the exact thrust forces yields to a set of six equations with sixteen

unknowns. To resolve this limitation, a new mathematical grouping of thrusters is

introduced just with the aim of finding the exact thrust forces. This new configuration is

based on a selection of pair thrusts R and W that states: *"if thruster R is on, then thruster*

W will never be on and vice versa." The new configuration based on thruster's pair is

described in Table 5.1

Table 5.1

Configuration of Thruster's Pair for Control Allocation

Thruster Pair	Thruster Number
T_E	7 and 8
T_F	3 and 4
T_G	1 and 2
T_H	5 and 6
T_{ABCD}	9,10,11,12,13,14,15 and 16

Equations 5.38 and 5.39 show the new forces and moments equations obtained using the new configuration of thruster's pairs.

$$\sum \vec{F}_{EASY} = \begin{bmatrix} -T_A \sin(\alpha) - T_B \sin(\alpha) + T_C \cos(\alpha) + T_D \cos(\alpha) \\ -T_A \cos(\alpha) + T_B \cos(\alpha) + T_C \sin(\alpha) - T_D \sin(\alpha) \\ T_E + T_F + T_H + T_G \end{bmatrix} = \begin{bmatrix} F_x \\ F_y \\ F_z \end{bmatrix} \tag{5.38}$$

$$\sum \vec{M}_{EASY} = \begin{bmatrix} -T_H L_y - T_E L_y + T_F L_y + T_G L_y \\ -T_H L_x - T_F L_x + T_E L_x + T_G L_x \\ L_z \left[-T_A - T_B - T_C - T_D \right] \end{bmatrix} = \begin{bmatrix} M_x \\ M_y \\ M_z \end{bmatrix} \tag{5.39}$$

Recalling the configuration of EASY spacecraft and the type of controller discussed in section 5.1, it is stated that EASY will not perform any translation motion, but instead, it will perform rotational motion. Therefore, to find the exact thrust forces, the total forces acting in the X and Y axes are neglected. Then, the vertical force must be divided in two. Equations 5.40 through 5.45 are the new set of the equation used to find exact thrust forces.

$$\frac{F_z}{2} = T_E + T_F \tag{5.40}$$

$$\frac{F_z}{2} = T_H + T_G \tag{5.41}$$

$$M_x = -T_H L_y - T_E L_y + T_F L_y + T_G L_y \tag{5.42}$$

$$M_y = -T_H L_x - T_F L_x + T_E L_x + T_G L_x \tag{5.43}$$

$$M_z = L_z \left[-T_A - T_B - T_C - T_D \right] \tag{5.44}$$

$$\begin{bmatrix} F_{z/2} \\ F_{z/2} \\ M_x \\ M_y \\ M_z \end{bmatrix} = \begin{bmatrix} 1 & 1 & 0 & 0 & 0 \\ 0 & 0 & 1 & 1 & 0 \\ -L_y & L_y & L_y & -L_y & 0 \\ L_x & -L_x & L_x & -L_x & 0 \\ 0 & 0 & 0 & 0 & -L_z \end{bmatrix} \begin{bmatrix} T_E \\ T_F \\ T_G \\ T_H \\ T_{ABCD} \end{bmatrix} \tag{5.45}$$

The simultaneous solution of the system described in Equation 5.45 yields the results shown in Equation 5.46 through 5.50 for the exact thrust forces.

$$T_E = \frac{F_z}{2} - \frac{M_x}{4L_y} + \frac{M_y}{4L_x} \tag{5.46}$$

$$T_F = \frac{F_z}{2} + \frac{M_x}{4L_y} - \frac{M_y}{4L_x} \tag{5.47}$$

$$T_G = \frac{F_z}{2} + \frac{M_x}{4L_y} + \frac{M_y}{4L_x} \tag{5.48}$$

$$T_H = \frac{F_z}{2} - \frac{M_x}{4L_y} - \frac{M_y}{4L_x} \tag{5.49}$$

$$T_{ABCD} = \frac{M_z}{L_z} \tag{5.50}$$

5.3 Performance Metrics

In order to evaluate the performance of the control system architecture presented in section 5.2.; a set of three performance metrics were developed and included in the simulation and implementation results in chapter 8. The mentioned metrics monitor the ability of the controller to achieve the desired attitude while maintaining a high tracking control performance during a given maneuver (Perez 2016).

Two of the performance metrics are related to the state vector in Equation 5.3, angular velocities and quaternions, whereas the third one correlates the total actuator activity of the system. All three performance metrics are calculated for a given time history and a set of cut-off parameters $C\Omega$, $C\Delta Q$, $C\Delta S$, and CP, in Equations 5.51, 5.52, 5.53 and 5.54 are used to represent the worst-case among a multiple performed tests. These cut-off values are used to normalize the global performance metric (Perez 2016).

5.3.1 Angular Rate Performance Metric

The angular rate performance metric takes into consideration the error between the commanded values and the current values of the angular rates ω_{ex}, ω_{ey} and ω_{ez}. Thus, this metric is calculated using the root mean square of the sum of the three mentioned angular rate errors as shown in Equation 5.51.

$$\tilde{e}_{\Omega} = \frac{1}{C\Omega}\left(\sqrt{\int_0^T \omega_{ex}^2 dt} + \sqrt{\int_0^T \omega_{ey}^2 dt} + \sqrt{\int_0^T \omega_{ez}^2 dt} \right) \tag{5.51}$$

5.3.2 Quaternion Performance Metric

The attitude performance metric measures the accumulative error of the commanded attitude angles (in quaternion attitude representation) with respect to the current attitude angles, δq_0, δq_1, δq_2, and δq_3. This performance is calculated using the mean square root of the total unit quaternion tracking error, as shown in Equation 5.52.

$$\tilde{\delta}_q = \frac{1}{C\Delta Q} \sqrt{\int_0^T \left[(1-\delta q_0)^2 + \delta q_1^2 + \delta q_2^2 + \delta q_3^2 \right] dt} \tag{5.52}$$

5.3.3 Solenoid Performance Metric

A solenoid performance metric is implemented with the aim of characterize the fuel consumption of the system in relation to the total actuation of each solenoid valve over a predetermined period of time. It is calculated as the sum of the root mean square of the PWM commanded signals of the total time the solenoid valve remained open, as shown in Equation 5.53 (Perez, 2016).

$$\tilde{s} = \frac{1}{C\Delta S}\left(\sum_{i=1}^{16} \sqrt{\int_0^T S_i(t) dt} \right) \tag{5.53}$$

5.3.4 Global Performance Index Metric

The results of the above performances metrics are grouped into a global performance Index Metric which provides an overall performance of the controller implemented for EASY. As shown in Equations 5.54 and 5.55, within this performance metric, a weight can be assigned to each of the performance metrics in consideration. The designation of the weight is based on controller performance's criteria; more weight is assigned if the given performance metric under study affects the performance of the controller directly, while less weight is assigned in the case that the error for a given metric does not affect the performance of the system. For this thesis, is established the same weight for each of the performance metrics.

$$P_I = 1 - \left[\frac{1}{3}\tilde{\delta}_q + \frac{1}{3}\tilde{e}_\Omega + \frac{1}{3}\tilde{s} \right] \tag{5.54}$$

$$\tilde{P}_I = \frac{P_I}{CP_I} \tag{5.55}$$

6. Software Development

The development of software tools or computing models that allow the prior and post testing of a defined system is a vital part when a research is being performed. In this chapter, is described the overall simulation and implementation environment of the algorithms used to model and test EASY spacecraft. Additionally, a description of the virtual environment developed for this research is also provided.
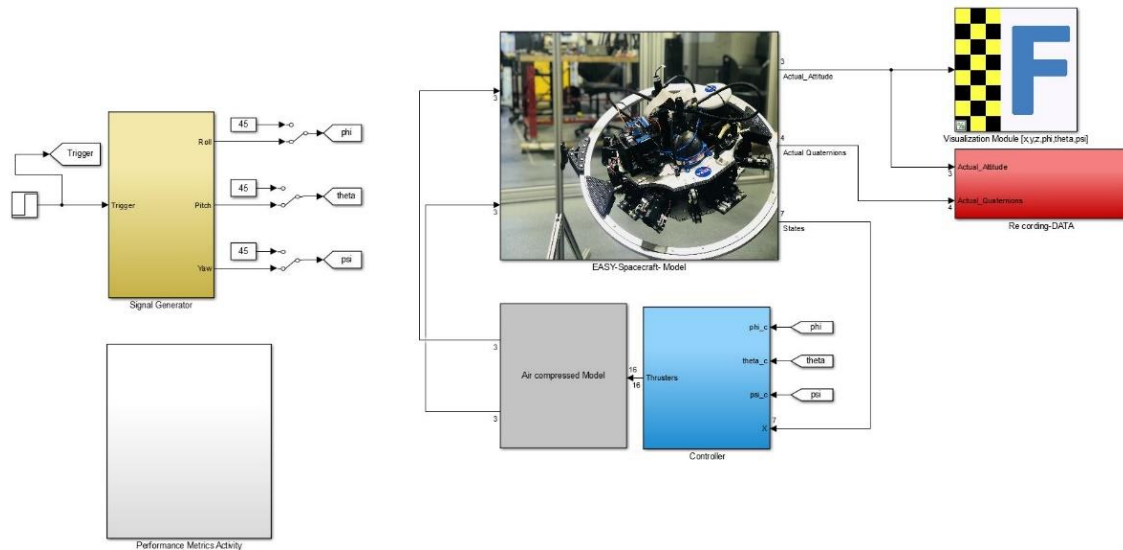

Figure 6.1 Simulation Environment EASY Spacecraft.

6.1 Simulation

A simulation environment was developed using MATLAB/Simulink to support the development and design of the proposed control laws algorithms mentioned in Chapter 5. The simulation environment shown in Figure 6.1 describes the main setup and components. Signal generator module is used to generate the commanded or desired attitude in Euler angles. Transformation of Euler angles into quaternions is performed within the controller module, which solves the control law architecture described in Chapter 5. Flight Gear interface module is used to provide 3D visualization of EASY.

The simulation also contains a Performance Metric Activity module used to measure and evaluate the performance of the controller. EASY's dynamics and compressed air modules are connected to the controller module. The simulation setup also features several output signals that are used to evaluate the attitude tracking performance within the Recording Data module. This last module includes scopes of desired parameters, such as quaternions and angular performance rates.

The Thrust Error Model described in Chapter 4 was implemented using the simulation environment, as shown in Figure 6. 2. In this figure, Section A provides the calculation of EASY's total forces and moments. As part of this section, the thrust frame to body module (section B) takes the normalized thrust force and calculates the force and moment vectors generated in the X, Y, and Z axes for each of the thrusters. In this calculation (section C), the thrust error caused by misalignment angles and the thrust magnitude error is included.
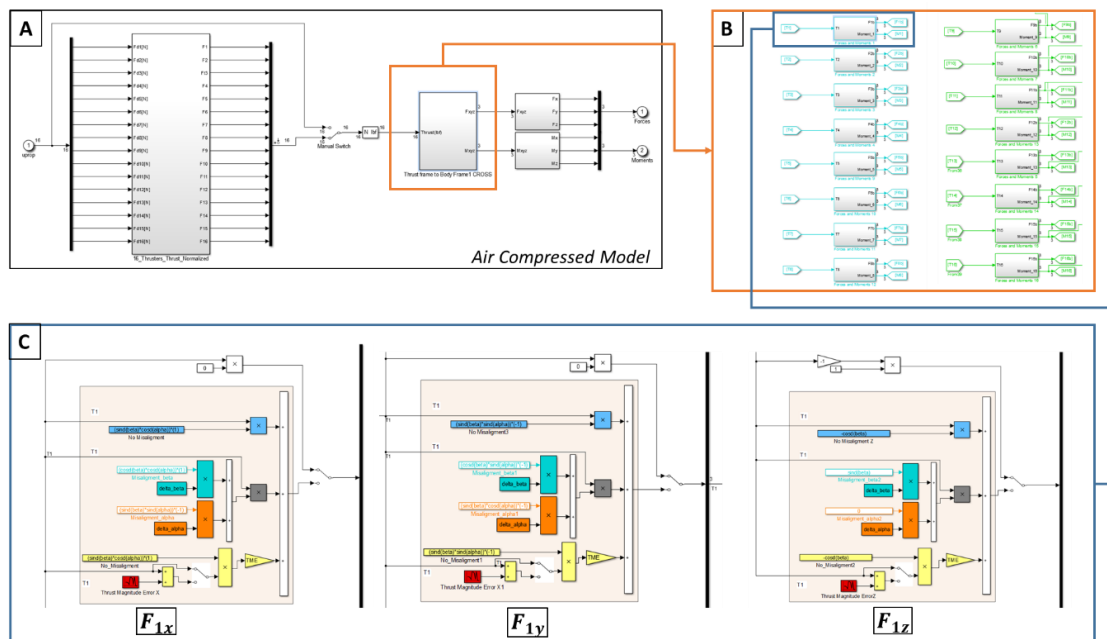

Figure 6.2 Implementation of MTE into a Simulation Environment.

6.2 Implementation

A general architecture of the control laws implementation code using MATLAB/Simulink® is shown in Figure 6.3. The main difference between simulation and implementation codes relies on the use of a hard real-time operating system (ROS) xPC-Target by MATLAB/Simulink®. This ROS system offers flexibility for fast prototyping capabilities by allowing compilation and deployment of developed Simulink models from a host computer on the EASY's PC/104 onboard computer, referred to as a Target. The implementation code also contains multiple blocks developed at ADCL (Perez, 2016).to enable transmission of data from the sensors (IMU) and the delivery of data to the Solenoid's drive board and Mini Polulu servo controller.
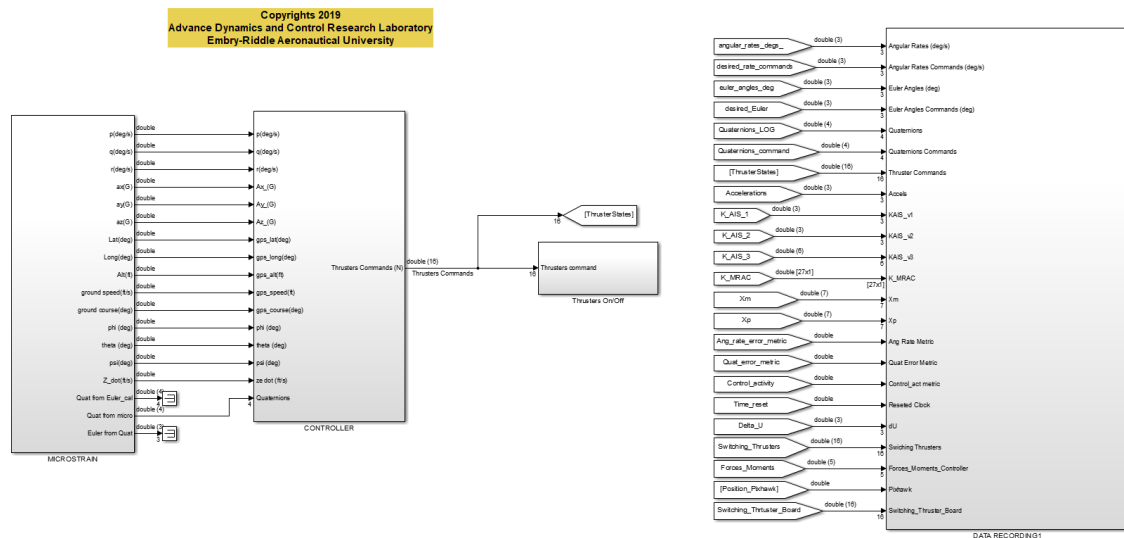

Figure 6.3 General Architecture of Implementation Code.

Using Simulink-Real time explorer, a GUI interface was developed at ADCL (Perez, 2016). This GUI interface, shown in Figure 6.4, allowed the execution in real-time of EASY's maneuvers and the monitoring of sensor data and thrust commanded to each

thruster. Additionally, a set of commands are programmed to inject selected thruster's
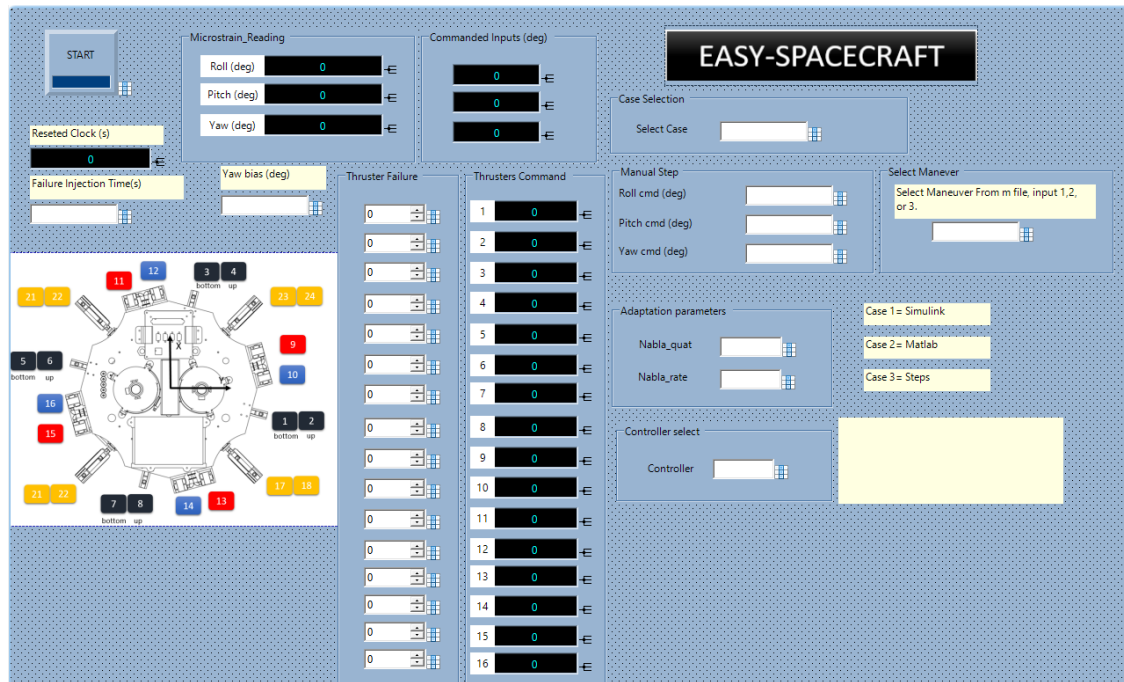
failures on the system in real-time.

Figure 6.4 GUI used for Normal Flight-Testing.

6.2.1 Tuning Real-Time

Figure 6.5 shows an additional GUI developed at ADCL (Perez, 2016).with the aim

of allowing the tuning of the control gains of the given control law system. This GUI

allows the tuning in real-time of the $K_{\omega q}$ control gains of the virtual controller described

in Chapter 5. A plot example of the tuning process is also shown in Figure 6.5. From the

plot, it can be noticed that the pre-define maneuver started at 20 seconds, and the tracking

of the signal is not being accomplished for the followed 20 seconds. At 40 seconds, the

controlled is already tuned, which increases the performance in real-time of the tracking

signal.
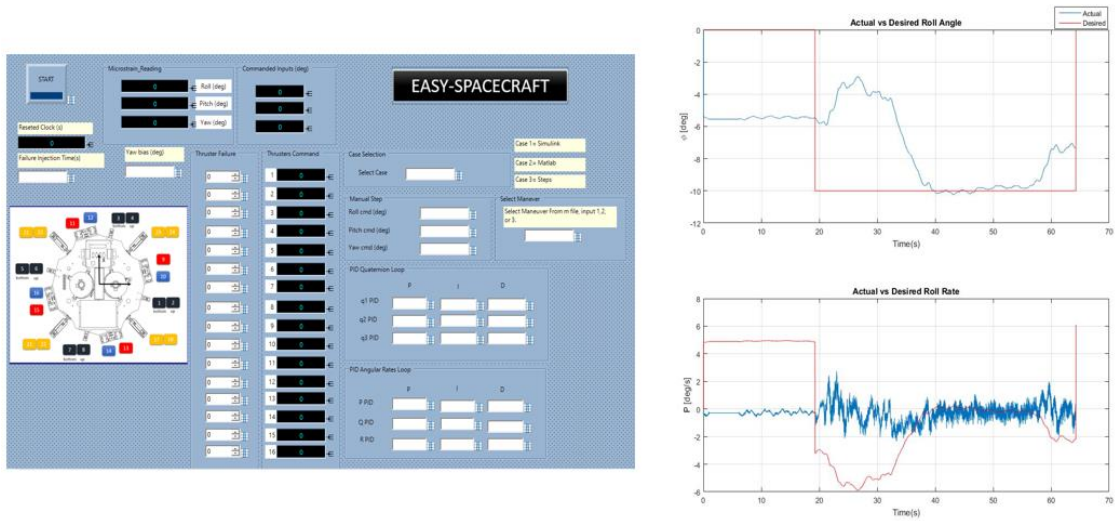
Figure 6.5 GUI used for Tuning Purposes of the Controller.

6.3 Virtual Environment

The modelling process of the 3D visual display for EASY was developed using the interaction between a 3D creation software CATIA VR5, a flight simulator Flight Gear, and an intermediate software Matlab/Simulink. Matlab/Simulink uses User Datagram Protocol (UDP) as the communication protocol to send data to FlightGear. Figure 6.6 shows Matlab/Simulink interface with Flight performing a given maneuver.

Figure 6.6 EASY 3D Visualization in Simulation using FlightGear.

7. Flight Testing Environment

The flight testing setup for EASY includes the mounting of the vehicle on a gimbal's frame and connected to an offloading system. This off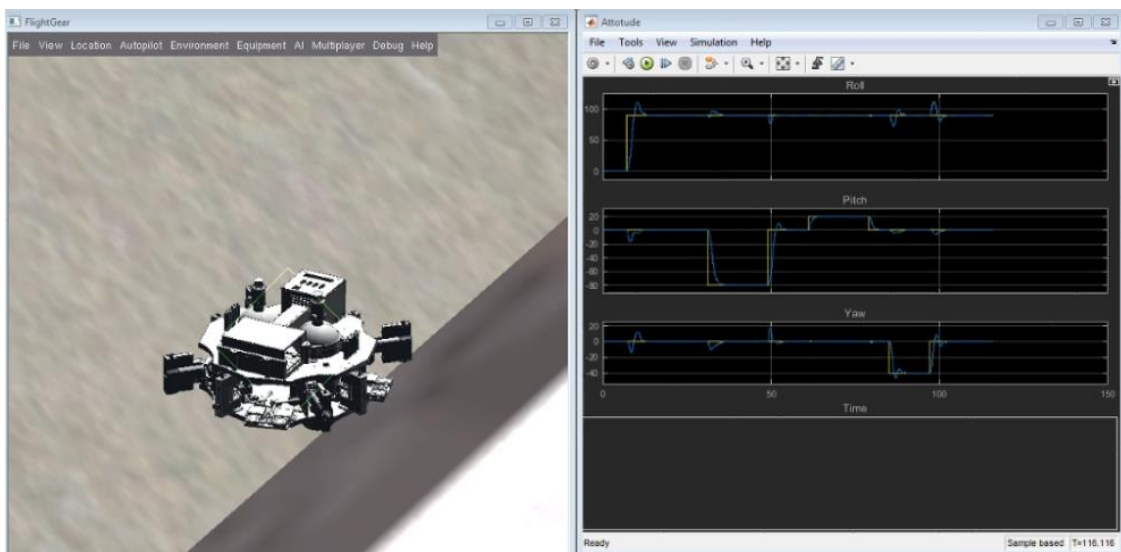loading system facility, known as Integrated Gravity Offloading Robotic System (IGOR), is available at the Advanced Dynamics and Control Laboratory. IGOR system allows the simulation of partial-gravity by using an offload mode, so a more realistic environment of a real space mission can be simulated. Figure 7.1 shows the general overview of the setup for EASY's implementation environment.

During a typical flight testing, IGOR system is configured with the partial gravity of the desired environment. The spacecraft's weight is sensed by IGOR and correlated to the pre-defined gravity value. Using Matlab/Simulink Real-Time, the communication between the host and the onboard PC/104 (Spacecraft) computers can be achieved. In this way, all the systems can communicate with each other in real-time.
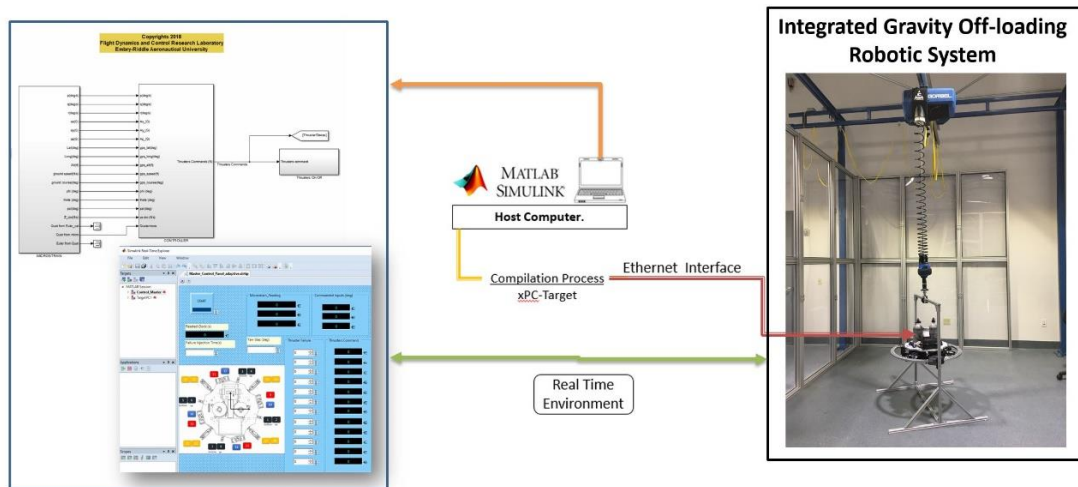

Figure 7.1 EASY Implementation Environment.

7.1 Integrated Gravity Off -Loading System – IGOR

IGOR concept is an active system to gravity offloading of space structures that deploy in six degrees of freedom plus translation in the three axes. A scalable gravity offload device simulates reduced gravity for the testing of various surface system elements such as mobile robots, excavators, habitats, and flyers in a relevant environment. The system has been designed to support a wide range of payload weights over a wide space of vertical and horizontal travel with fast response and almost zero friction. The device is capable of simulating reduced gravity by integrating a single-point to suspend the space vehicle via a load cable and a pair of linear drive tracking stages in the horizontal plane. An active control system is being implemented to minimize the horizontal drag forces on the payload, and it will actuate the linear drive stages such that the vertical cable is centered over the vehicle payload. Thus, the load cable is kept close to vertical as the payload moves under its own power. The horizontal and vertical systems work together to deliver gravity offloading for arbitrary trajectories of the payload.

Figure 7. 2 shows IGOR facility concept that includes three main subsystems: a gravity offloading device (IQ-GForce manipulator) that carries the weight and accommodates vertical motion of the payload; a linear movement X and Y stage system driven by commercial off the-shelf stepper motors that moves the IQ-device horizontally to keep the load cable vertical during active tracking; and an orientation sensor that measure the angle of the cable to control the horizontal movement. The result is a rectangular working area whereby the gravity offload device can simulate reduced

gravity in the area defined by the length of the linear movement system by the width (reach) of the 2 degree-of-freedom manipulator.

7.1.1 G-Force Intelligent Assist

The IQ-Device is a single-degree-of-freedom gravity offloading system that supports a wide range of payload weights over several centimeters or more of vertical travel with arbitrarily low stiffness, zero static deflection, minimal added mass, freedom from spurious modes, and perhaps most importantly, zero friction. The force application mechanism is principled upon precision and maintenance of pressure in an air cylinder. Precision regulation of pressure supply enables

constant force over the throw of the air cylinder. Varying the regulator supply pressure to the air cylinder(s) modifies the force experienced by the test article and therefore enables a gravity offload device to simulate a range of gravity fields proportional to the ability to regulate pressure.

7.1.2 Active Tracking Control System

The X and Y tracking active system is being designed to move up to 6ft/sec approximately in each direction. This configuration minimizes the horizontal drag forces, so the IQ-device is centered over the payload, and the load cable is kept close to vertical as the payload moves under its own power. The horizontal and vertical systems will work together to deliver gravity offloading for arbitrary trajectories of the payload at different ranges of motion.

7.1.3 Orientation Sensor

An orientation sensor system will measure the angle of the cable to control the bridge and runway movement. During active tracking, the horizontal forces on the

payload will create an angle on the cable relative to true vertical. This angle can be measured, so a closed-loop control system will minimize it to maintain the cable very close to vertical as the payload moves.
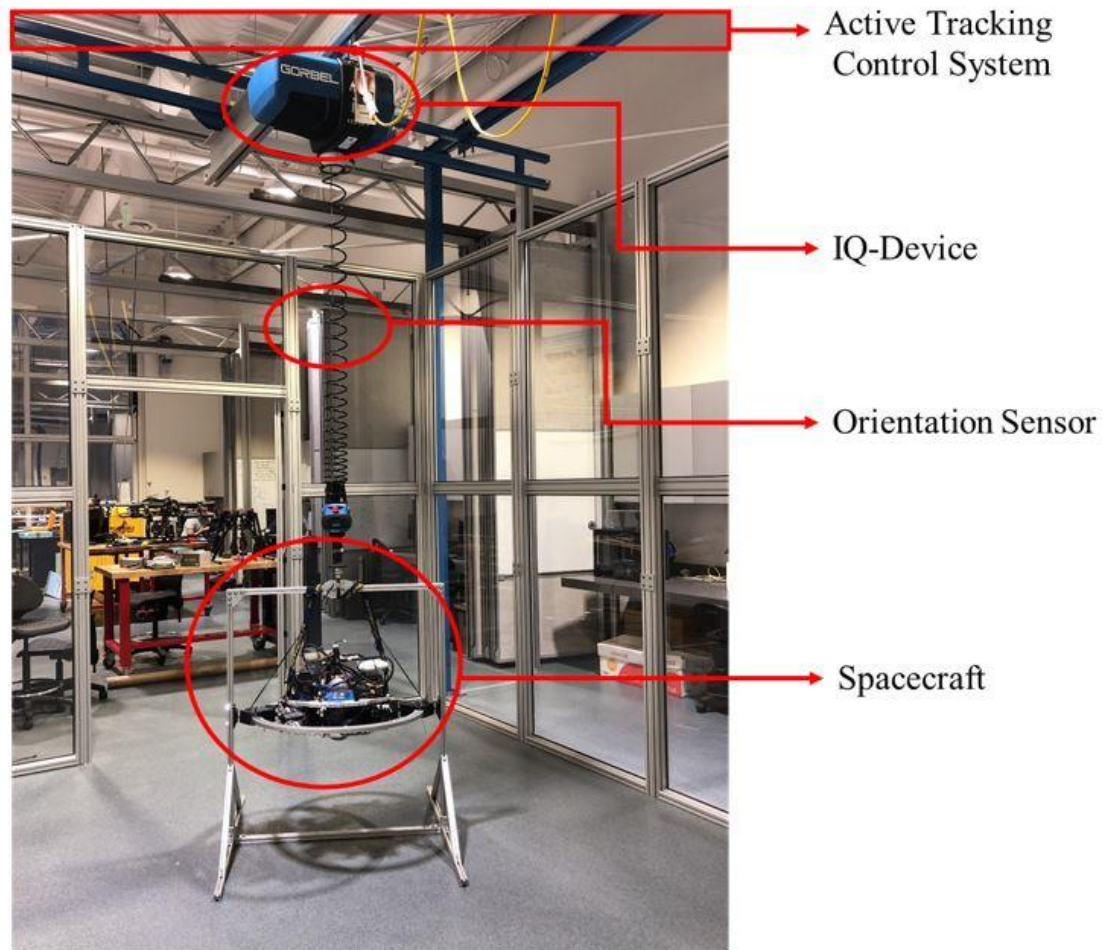

Figure 7.2 Integrated Gravity Offloading System.

8. Performance Analysis

In this chapter, the closed-loop performance system is analyzed using simulation and implementation. The main focus is to evaluate the stability and dynamic response of EASY's while the controller stabilize the system at the desired attitude maneuver. In addition, an analysis is presented for the performance under undesired dynamics outlined in Chapter 4. Demonstration of the correct on-off switching logic (control allocation) of thrusters based on the commanded maneuver is also explained in this chapter.

As previously mentioned, the EASY's equations of motion have been implemented using the quaternions approach. However, the quaternions are converted back into the Euler's angles representation for visualization purposes. EASY's configuration parameters used for simulation and implementation are shown in Table 8.1

Table 8.1

Design Parameters

Parameter	Units
Gravity	0.28 m/s2
Total Mass- EASY	23.1332 Kg
Type of fuel	Compressed Air
Max. Thrust per attitude thruster	1.35 N
Ixx	0.5698
Iyy	0.3679
Izz	0.6355

Since EASY has been designed for space exploration of bodies with low gravity environments, a dwarf planet known as Ceres has been established as the working environment for EASY's mission operations. Table 8.2 shows the relevant characteristics of this dwarf planet:

8.1 Simulation Results

Simulations results include the use of vehicle propulsion, attitude control system,

control allocation, and dynamic model. Table 8.3 details the desired dynamic

characteristics used to design control gains for numerical simulations. Likewise, Table

8.4 shows outlines estimated gains that were implemented within the controller, as

described in Chapter 5.

Table 8.2

Ceres Physical Characteristics

Quantity	Value	Units
Radius	473	km
Surface Gravity	0.28	m/s2
Escape Velocity	0.51	m/s
Atmospheric Pressure	Insignificant	
Sidereal period	~9	hours
Solar Constant	154.2 to 209.0	W/m2
Temperature Range	Unknown min – 235 max	K
Surface material	Carbonaceous regolith	

Table 8.3

Desired Damping Ratio and Natural Frequency for Control Gains

Damping Ratio		Natural Frequency	
ζ_x	0.8261	ω_{nx}	1.7293 [rad/s]
ζ_y	0.8261	ω_{ny}	1.7293 [rad/s]
ζ_z	0.8261	ω_{nz}	1.7293 [rad/s]

Table 8.4

Control gains

$K_{\omega q}$ Control Gains			
K_{ω_x}	2.9630	K_{q_1}	2.1709
K_{ω_y}	2.9630	K_{q_2}	2.1709
K_{ω_z}	2.9630	K_{q_3}	2.1709

8.1.1 Attitude Performance and Control Allocation for Nominal Condition

To validate the attitude performance, a set of sequence rotations were identified. Each set of rotations is presented with a time period of six seconds, i.e. every six seconds, the new desired attitude angle is commanded. **Table 8.5** illustrates the first set of these rotations, which is Maneuver No. 1. This maneuver includes different rotations (positive and negative direction) for different attitude angles.

Table 8.5

Maneuver No. 1.

Time [s] / Attitude [º]	0	1	2	3	4	5	6	7	8	9	10	11	12	13
ϕ	0	0	**-10**	**-10**	0	0	0	0	0	0	0	0	0	0
θ	0	0	0	0	0	0	**-20**	**-20**	**-20**	0	0	0	0	0
ψ	0	0	0	0	0	0	0	0	0	0	0	**10**	**10**	0

The stabilization performance of the controller for maneuver No. 1 is shown in Figures 8.1 and 8.2 for quaternion and Euler's angles representation, respectively. It is clear that the proposed controller achieves an acceptable performance with high stabilization accuracy after performing roll, pitch and yaw rotations.

As described in Chapter 5, the controller was designed using a quaternion-based feedback linearization approach. This controller provides regulation control by driving the actual quaternions to the desired or commanded values while regulating the angular velocities to zero. As it can be noted in Figure 8.3, the angular velocities converge to zero once the maneuver is performed.
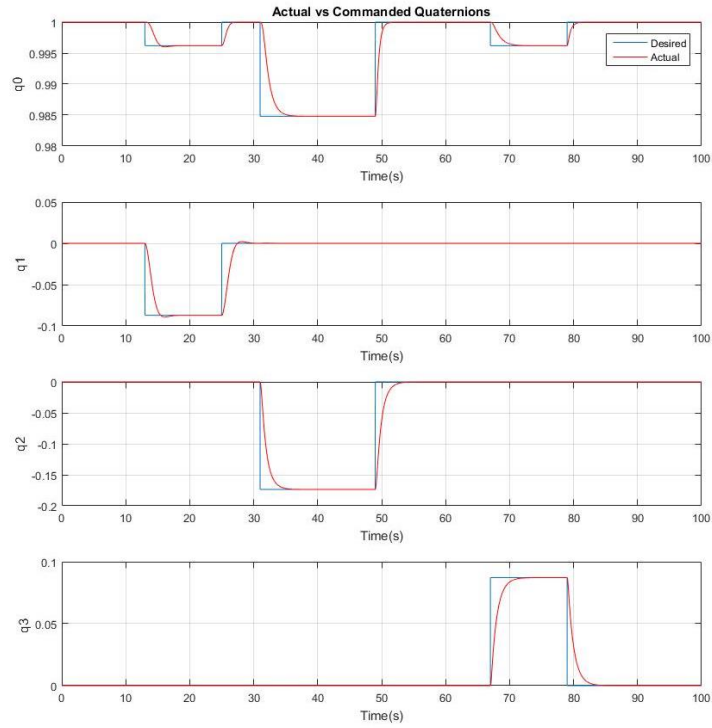
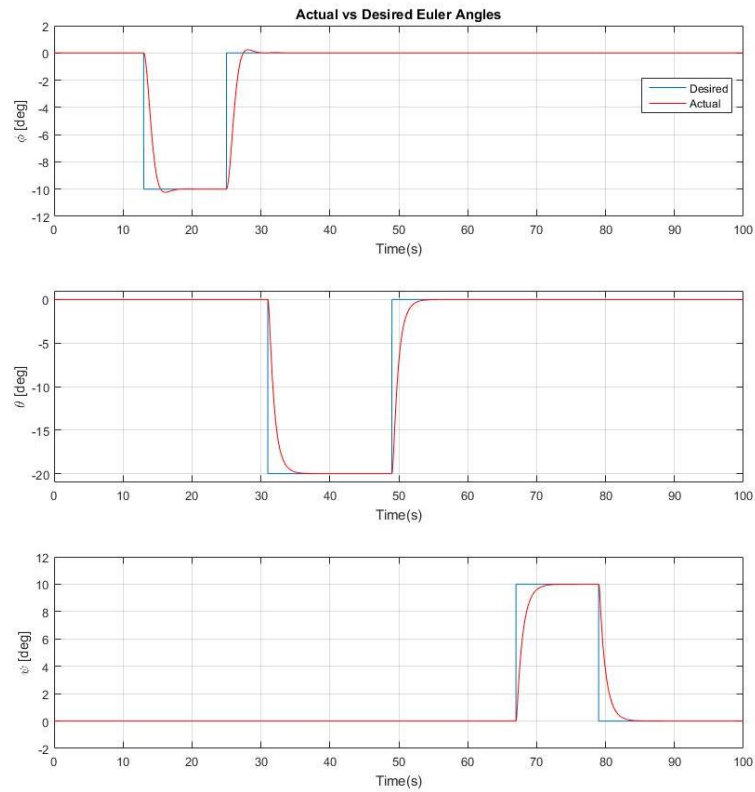*Figure 8.1* Quaternions Attitude Representation for Maneuver No. 1.

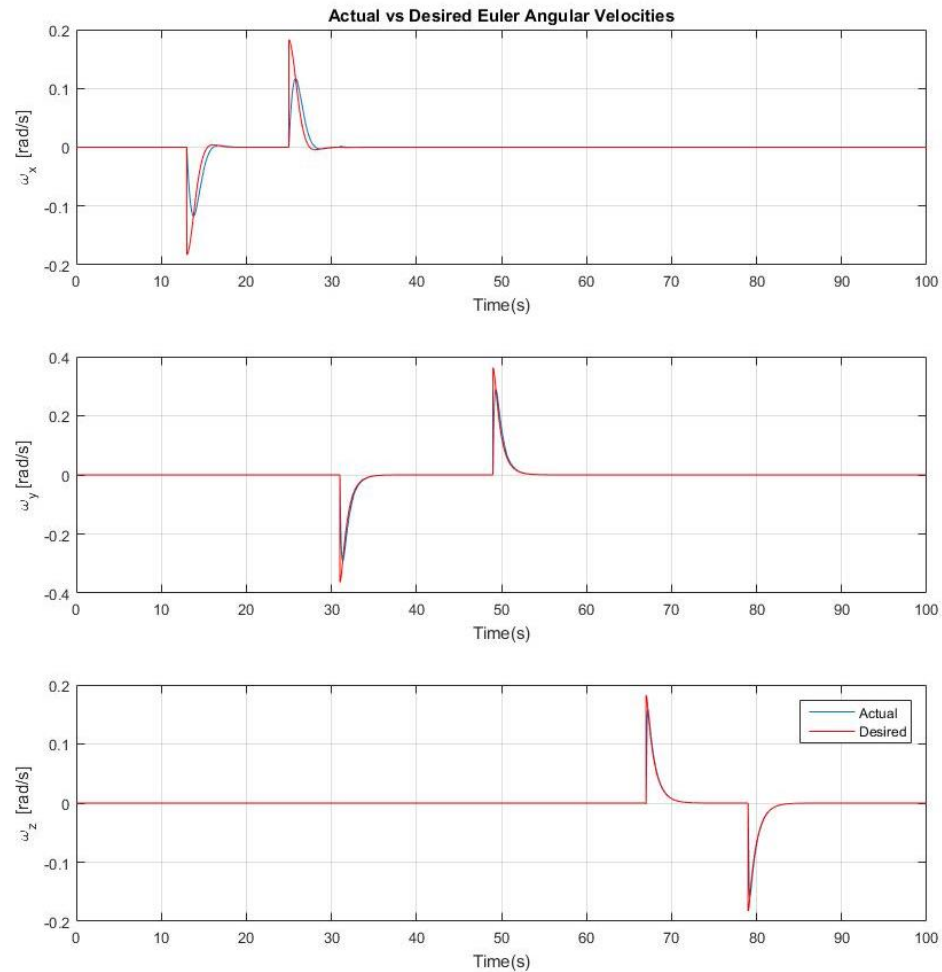*Figure 8.2* Euler Attitude Representation for Maneuver No. 1.

Figure 8.3 Angular Velocities for Maneuver No. 1.

Similarly, Figure 8.4 provides a time history of the Moments acting on EASY.

Essentially, it can be noted that the stabilization performance of the moments given by

the controller is well performed. As expected, during the period of times that the vehicle

is not performing any maneuver, the desired attitude is zero degrees. The moments

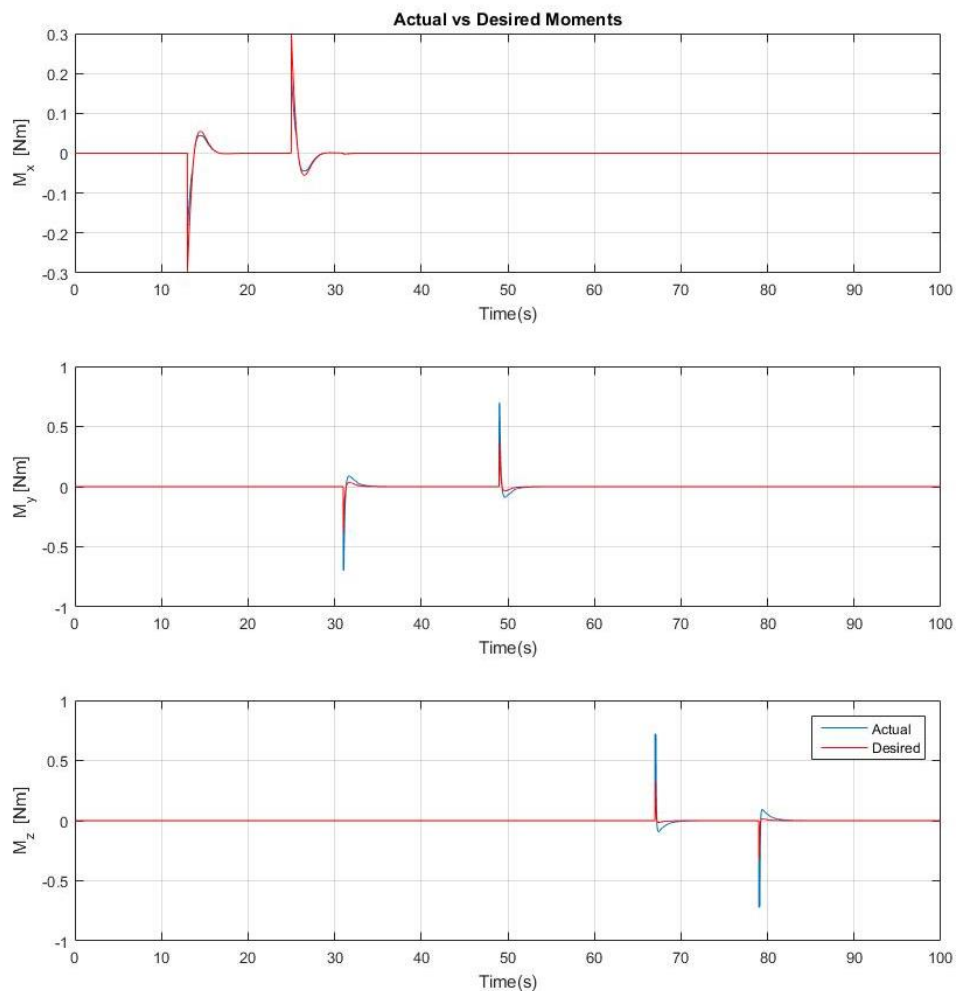remain at zero, which does not generate any rotation on the vehicle.

Figure 8.4 Moments for Maneuver No. 1.

Results from the actuation activity metric are shown in Figure 8.5. The bar represents

the normalized value of the total actuation of the thrusters. The pie graph grouped the

thrusters used for yaw rotation, and the thrusters used for roll and pitch rotations (due to

the existing coupling). This graph shows the percentage of actuation activity performed

by these two groups of thrusters with respect to the total actuation (solenoid) activity.
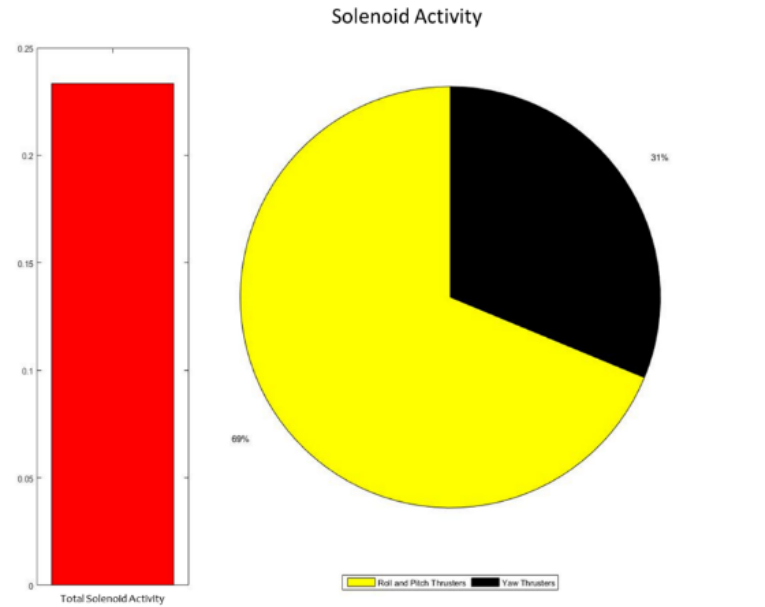
Figure 8.5 Actuation Activity for Maneuver No. 1.

Figure 8.6 and 8.7 depict the time history of the thrust activity (for all 16 thrusters) while EASY performs maneuver No. 1. The plots show the amount of thrust required to perform each maneuver. If a thruster is not needed within a specific maneuver, no thrust will be commanded. In this manner, the commanded thrust can be correlated to the state of the thruster off/on (control allocation), which represents the thruster used to perform a specific rotation. Table 8.6 summarizes the configuration of the thrusters to perform roll, pitch, and yaw maneuvers in the positive and negative direction.

Table 8.6

Control Allocation to Accomplish EASY Rotations

Attitude Command	Thrusters
Positive Roll	2, 4, 5 and 7
Negative Roll	1, 3, 6 and 8
Positive Yaw	9, 11, 13 and 15
Negative Yaw	10, 12, 14 and 16
Positive Pitch	2, 3, 5, and 8
Negative Pitch	1, 4, 6 and 7

Figure 8.6 illustrates the commanded thrust for the thrusters involved in roll and pitch rotations. Within the first 11 seconds of simulation, EASY keeps its initial position. At 12 seconds, the negative roll maneuver starts with thrusters 1, 3, 6, and 8 turned on. A few seconds later, thrusters 2, 4, 5 and 7 are turned on to maintain the stability of the spacecraft. During this period of time, thrusters 2, 4, 5 and 7 are not spending a significant amount of thrust. Since the setup of maneuvers demands to be back to the initial position, the time between 24 and 38 seconds describe a positive roll maneuver which is accomplished by firing thrusters 2, 4, 5 and 7 first, and then thrusters 1, 3, 6, and 8 (for stabilization proposes). Negative and positive pitch maneuvers can be seen between 30-50 seconds where thrusters 1, 7, 4, and 6 are turned on for a negative direction and 2, 3, 5, and 8 for a positive direction.

Finally, Figure 8.7 shows a positive and negative yaw maneuver that is achieved between the seconds 68-80. Thrusters 9, 11, 13, and 15 are turned on for the positive motion while 10, 12, 14, and 16 produce a small thrust to keep the system stable. In the same way, thruster 10, 12, 14, and 16 are turned on to accomplish the rotation for negative motion while thruster 9, 11, 13, and 15 produce a small thrust for stability of the system.

Table 8.7

Maneuver No. 2.

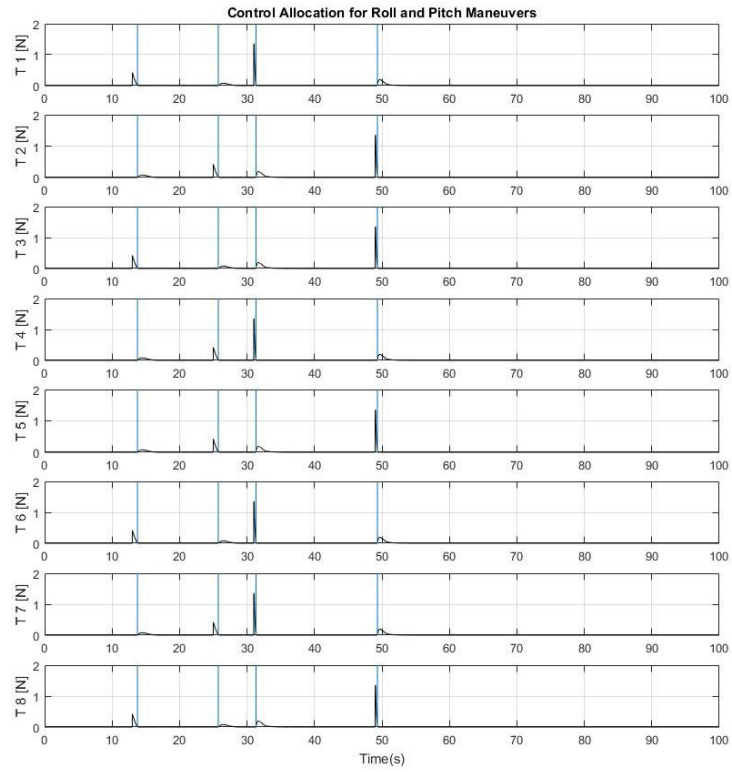| Time [s] / Attitude [°]	0	1	2	3	4	5	6	7	8	9	10	11	12	13
ϕ	0	0	0	0	0	0	0	0	0	0	0	**5**	**5**	0
θ	0	0	**-15**	**-15**	0	0	0	0	0	0	0	0	0	0
ψ	0	0	0	0	0	0	**-35**	**-35**	**-35**	0	0	0	0	0

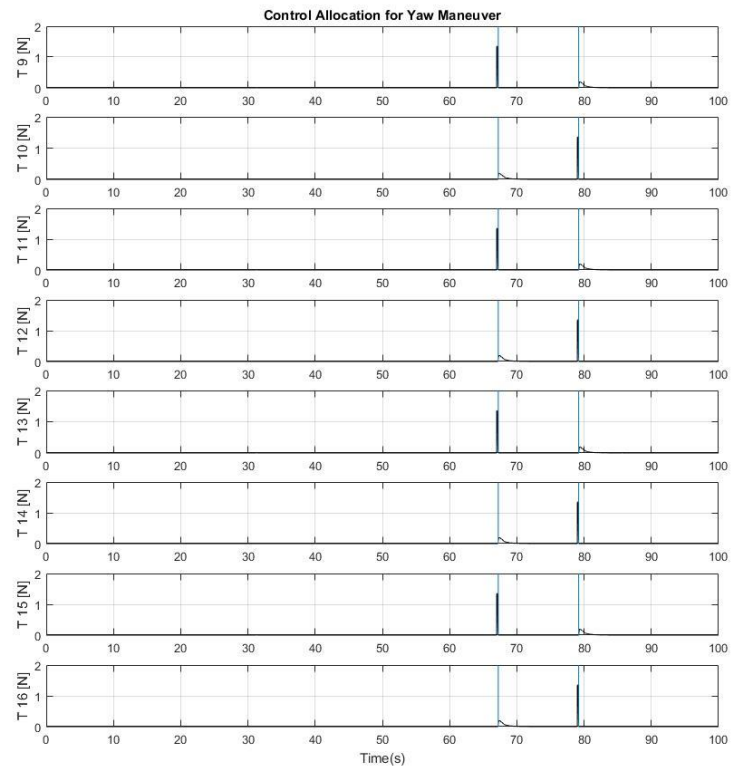*Figure 8.6* Control Allocation for Roll and Pitch Maneuvers No. 1.

Figure 8.7 Control Allocation for Yaw Maneuver No. 1.

An alternative maneuver was also selected, as shown in Table 8.7. For this maneuver, a negative pitch and yaw rotations, and a positive roll rotation are implemented to demonstrate the capability of the controller to perform positive and negative rotations. Figures 8.8 and 8.9 (quaternions and Euler's angles representation, respectively) show the attitude performance of maneuver No. 2 while the controller is stabilizing the system at the desired attitude.
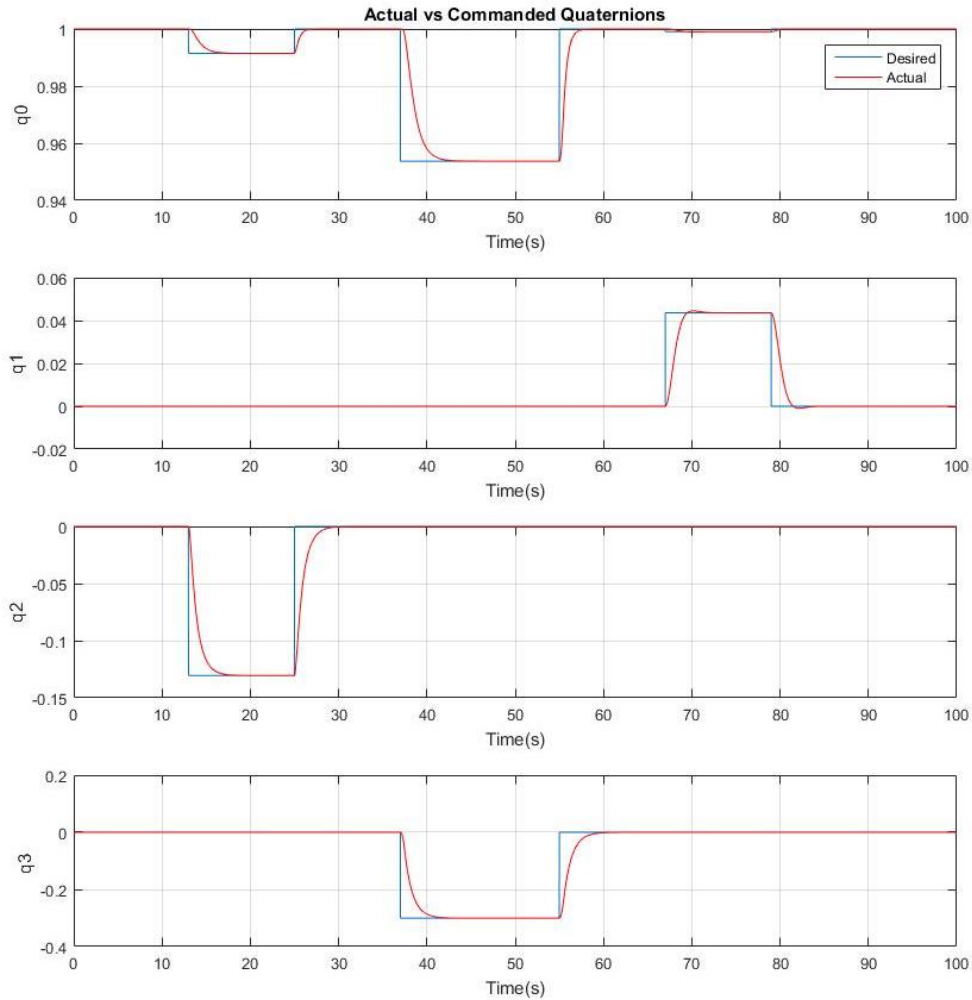

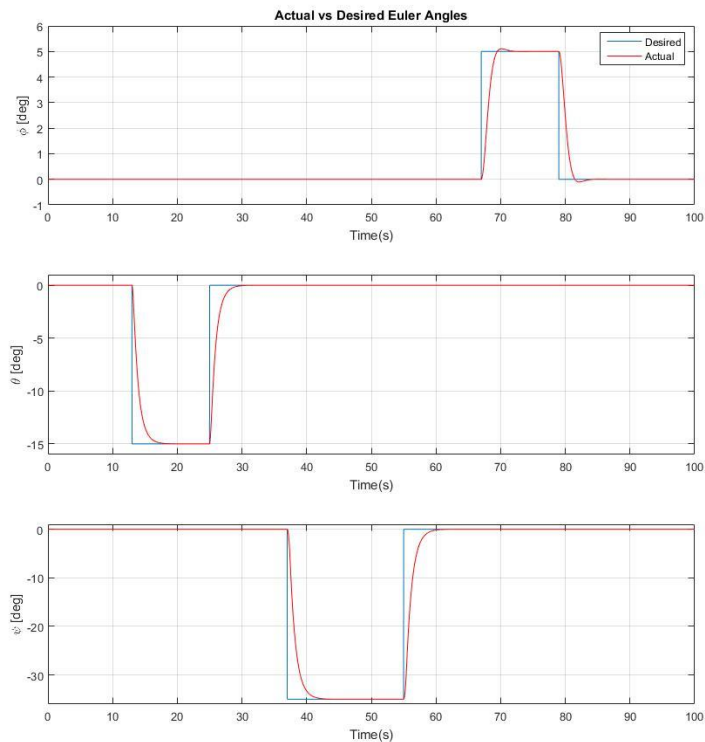*Figure 8.8* Quaternions Attitude representation for Maneuver No. 2.

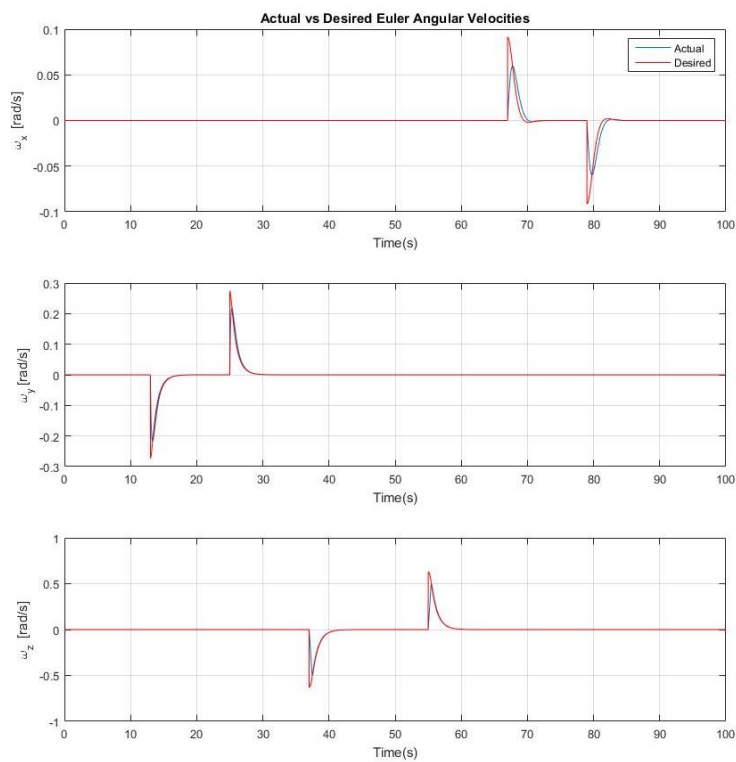*Figure 8.9* Euler Attitude Representation for Maneuver No. 2.

Figure 8.10 Angular Rates for Maneuver No. 2.

Similar to the previous maneuver, Figure 8.10 demonstrates that the angular velocities are driven to zero. The tracing of the moments for maneuver No. 2 is shown in Figure 8.11.
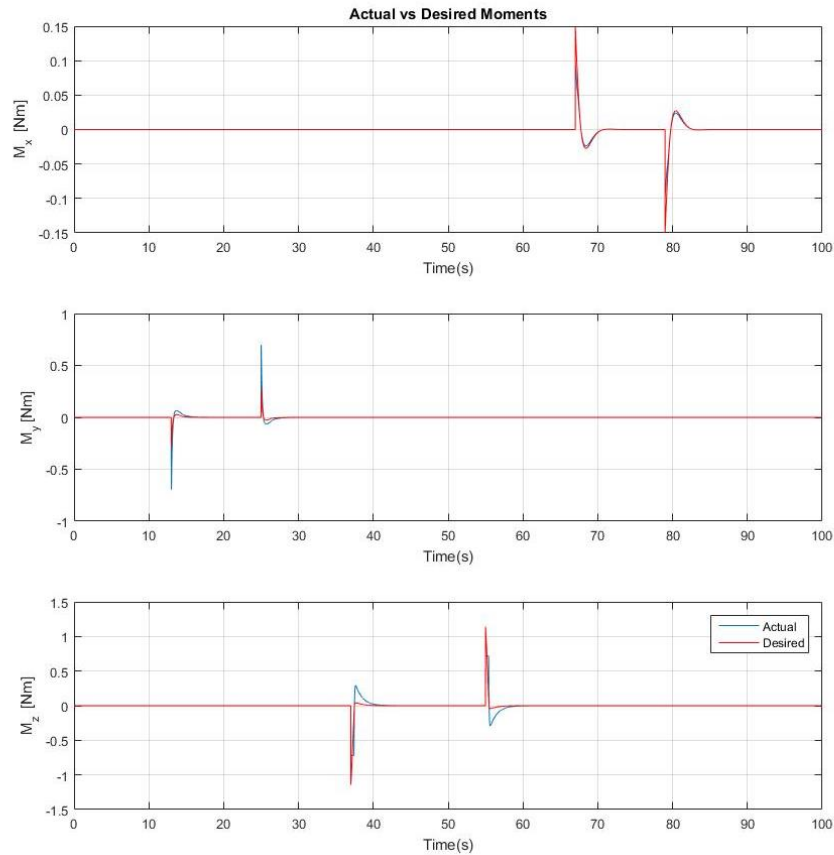

Figure 8.11 Moments for Maneuver No. 2.

Results from the Actuation activity metric are also shown for maneuver 2 in Figure 8.12. Because this maneuver type was selected with higher rotations, the actuation activity of the system increases as expected. However, small rotations for roll and pitch angles were also selected, which reduce the actuation contribution due to these set of thrusters. On the other hand, the majority of the actuation was done by the set of thrusters involved in the yaw rotation. It can be seen from the plot that 84% of contribution was due by the yaw thruster against the 18% of contribution that was due by the roll and pitch thrusters.
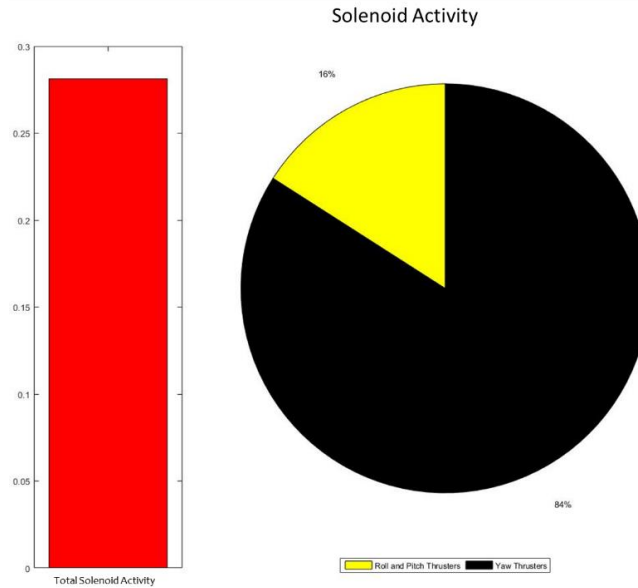
Figure 8.12 Thruster Activity for Maneuver No. 2.

Once again, the thrust commanded for each thruster is correlated to the on-off switching of attitude thrusters during maneuver No. 2, as shown in Figures 8.13 and 8.14. From Figure 8.13, it can be noted that during the first 11 seconds, the spacecraft remains in its initial position. At 12 seconds, the vehicle starts performing a negative pitch rotation. Thrusters 1, 4, 7, and 6 are fired while a few seconds later, thrusters 2, 3, 5 and 8 are turned on to keep the vehicle stable. During 66 and 80 seconds, the configuration of on-off thrusters for a positive roll rotation is described. Roll rotation is performed by using thrusters 2, 4, 5, and 7 in the positive direction followed by thrusters 1, 3, 6, and 8, and in the negative direction thrusters 1, 3, 6, and 8 are followed by thrusters 2, 4, 5, and 7.

In Figure 8.14, during 37 to 55 seconds, the yaw rotation is accomplished. In the negative direction, thrusters 10, 12, 14, and 16 are turned on, followed by thrusters 9, 11, 13, and 15. In the positive direction, thrusters 9, 11, 13, and 15.are turned on, followed by thrusters 10, 12, 14, and 16.
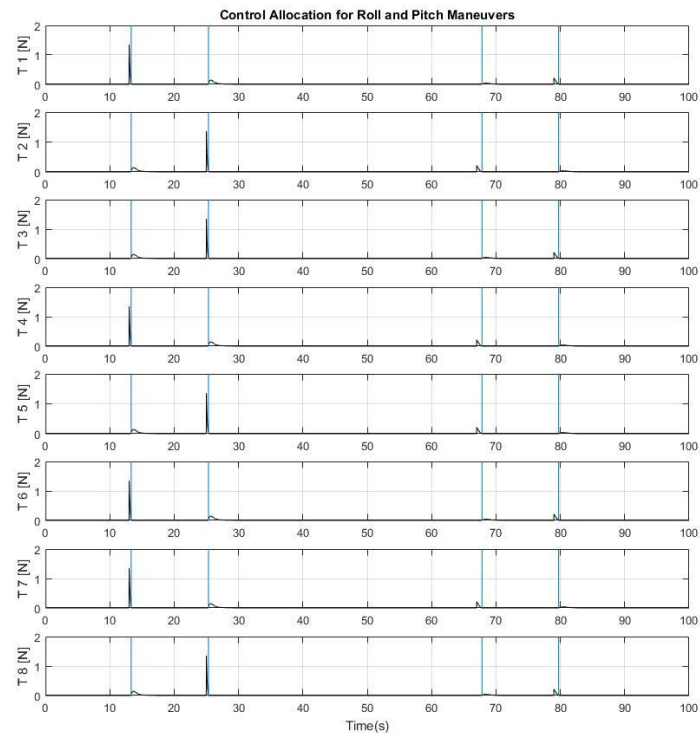
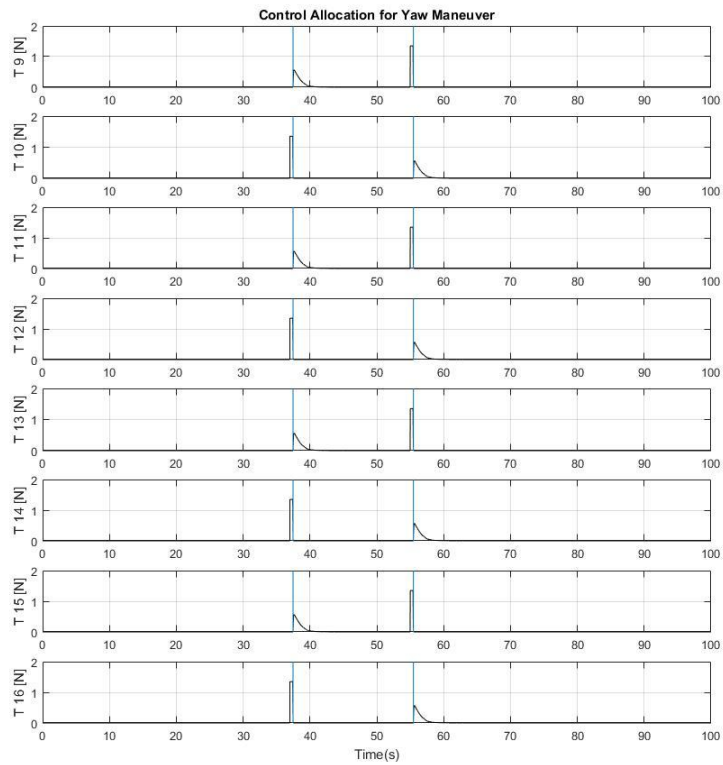*Figure 8.13* Control Allocation for Roll and Pitch Maneuvers No. 2.

Figure 8.14 Control Allocation for Yaw Maneuvers No. 2.

8.1.2 Attitude Performance with TMAE and TME

Simulations were also performed in order to evaluate the effects that the undesired

dynamics produce in the attitude performance of the vehicle and its overall stability. For

this purpose, a case of study is selected where a specific maneuver is established, as

shown in Table 8.8. This maneuver includes a rotation of 90 degrees to show the

capability of the controller to perform a rotation of 90 degrees in the pitch angle.

Table 8.8

Maneuver No. 3

Time [s] / Attitude [º]	0	1	2	3	4	5	6	7	8	9	10	11	12	13
ϕ	0	0	0	0	0	0	**2**	**2**	**2**	**2**	0	0	0	0
θ	0	**90**	**90**	0	0	0	0	0	0	0	0	0	0	0
ψ	0	0	0	0	0	0	**10**	**10**	0	0	0	**10**	**10**	0

This case of study represents a simple scenery where undesired dynamics produced

by Thrust Magnitude Error (Table 8.9) and Thrust Misalignment Angles (Table 8.10) are

present in multiple thrusters.

Table 8.9

Configuration of Thrust Magnitude Error for Maneuver No. 3

Thruster No.	Thrust Magnitude error
1 and 2	
9 and 10	2% of Thrust desired

Table 8.10

Configuration of Thrust Misalignment angle Errors for Maneuver No. 3

Thruster No.	Misalignment Angle
1, 3, 4, 6, 7 and 8	$\Delta\beta = 3$
10, 13, and 14	$\Delta\alpha = 2$

Figure 8.15 and Figure 8.16 show the overall attitude performance (quaternion and Euler's angles representation, respectively) while maneuver No. 3 is executed. These figures present the results obtained for the cases of nominal condition (Actual), the presence of thrust misalignment angles (Misalignment), when a small thrust magnitude error is considered (Thrust error), and when the mathematical thrust error model is used within the control allocation to compensate for these undesired dynamics (MTE).

As noted in these figures, in the presence of undesired dynamics, the overall tracking performance is slightly degraded. However, the controller is able to maintain an acceptable commanded attitude around bounds of nominal condition.
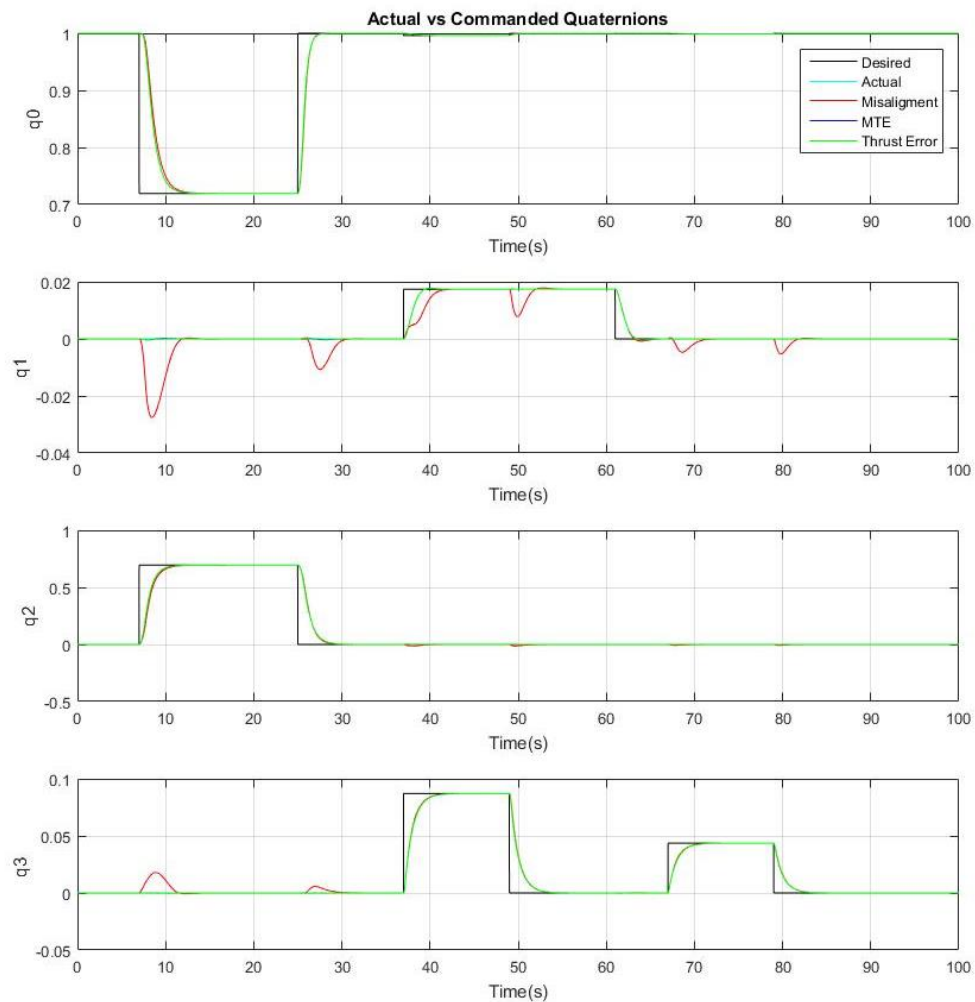

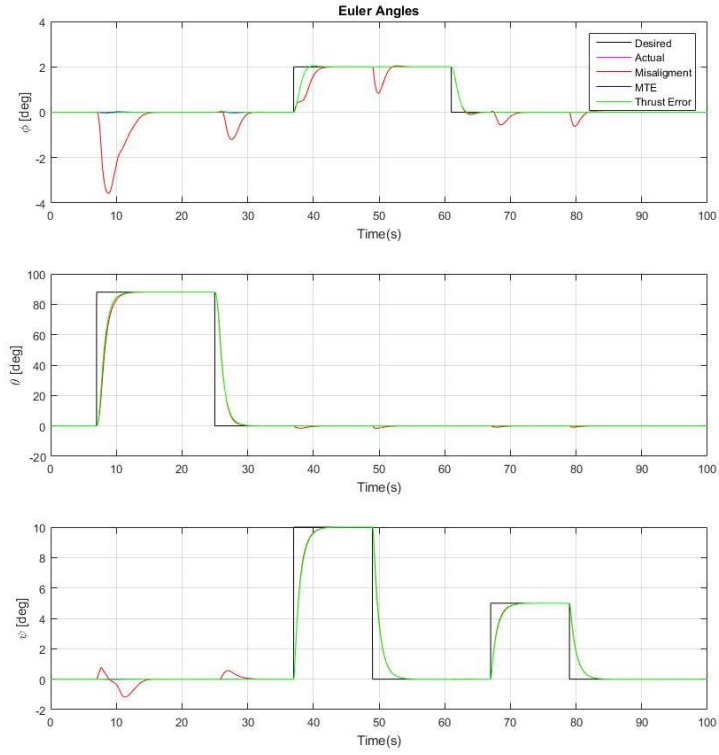*Figure 8.15* Quaternions Attitude representation for Maneuver No. 3.

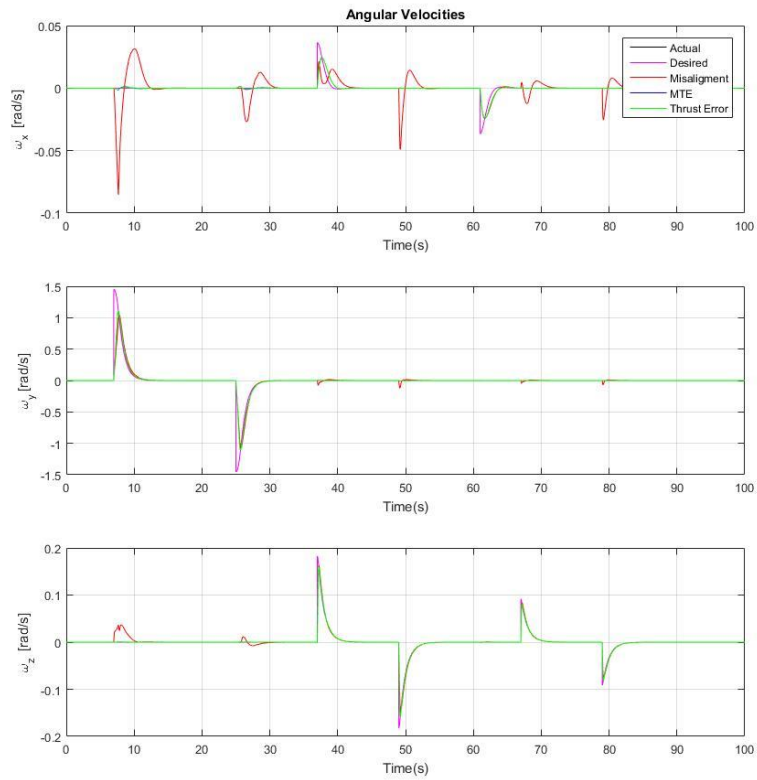*Figure 8.16* Euler Attitude Representation for Maneuver No. 3.

Figure 8.17 Angular Velocities for Maneuver No. 3.

The tracking response for angular velocities and moments acting on EASY are shown in Figures 8.17 and 8.18. The presence of thrust misalignments angles in different thrusters create extra forces acting in all three axes. These forces contribute to the generation of undesired moments that affect the desired rotations. In Figure 8.18, it can be noted that due to misalignments in the yaw's thrusters, an extra force in the X axis is generated. Thus, the moment around this axis presents a sudden rotation of higher magnitudes. This effect is also seen at the moment around Y axis.
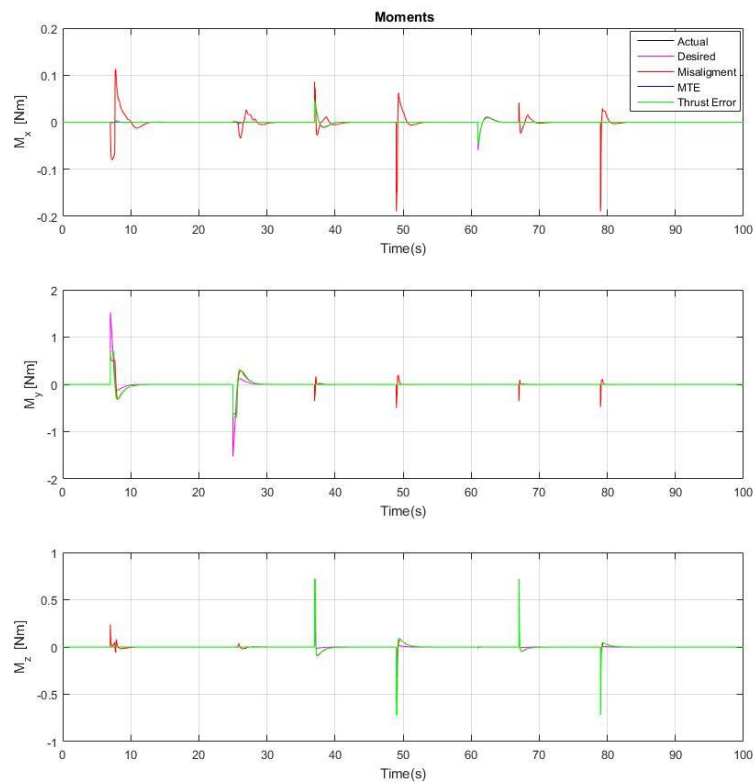

Figure 8.18 Moments for Maneuver No. 3.

Overall, Thrust Misalignments Angles affect the attitude performance of the vehicle by creating unexpected rotations. The thrust magnitude error considered in this case also contributes to the degradation of the attitude performance. However, since it was only

considered in a few of the thrusters and its magnitude was not beyond 2%, the attitude

response is close to the desired one. The implementation of the Mathematical Thrust

Error model within the control allocation helped to compensate for this undesired

dynamics by cancelling the effect in the feedback linearization process.

8.2 Implementation Results

This subsection describes the implementation results obtained from the quaternion

based feedback linearization controller described in Chapter 5. An evaluation of the

stabilization performance of the controller is presented under considering two cases: first

case, nominal condition, and second case, presence of undesired dynamics. A newly

defined maneuver is shown in Table 8.11

Table 8.11

Maneuver No. 4 for Implementation

Time [s] Attitude [°]	0	1	2	3	4	5	6	7	8	9	10
ϕ	**-20**	**-20**	**-20**	**-20**	**-20**	**-20**	**-20**	**-20**	**-20**	**-20**	**-20**
θ	0	0	0	0	0	0	0	0	0	0	0
ψ	0	0	0	0	0	0	0	0	0	0	0

8.2.1 Attitude Performance for Nominal Condition

Time history of attitude representation using quaternions and Euler is presented in

Figures 8.19 and 8.20, respectively. During the implementation process, the GUI

described in Chapter 8 is used, which facilitated the deployment of control law codes and

calibration of the initial attitude conditions before starting the maneuver. While this

process is in progress, the desired attitude maneuver is sent and recorded.

In Figures 8.19 through 8.23, it can be seen that some undesired rotation is achieved

in roll and pitch rotations at the beginning of the maneuver. This situation can be

explained due to the inaccurate distribution of pressure in the system. However, compensation for those undesired angles is accomplished. Although a steady state error is present in the pitch angle, it can be corrected with a better tuning of the controller. Despite this error, the attitude performance of the vehicle is acceptable.

Angular velocities tracking performance shown in Figure 8.21 support the performance of the controller shown in Figures 8.19 and 8.20. Although there is not zero error tracking, the existing error does not exceed more than 2 degrees per second for the angular velocities p and q.
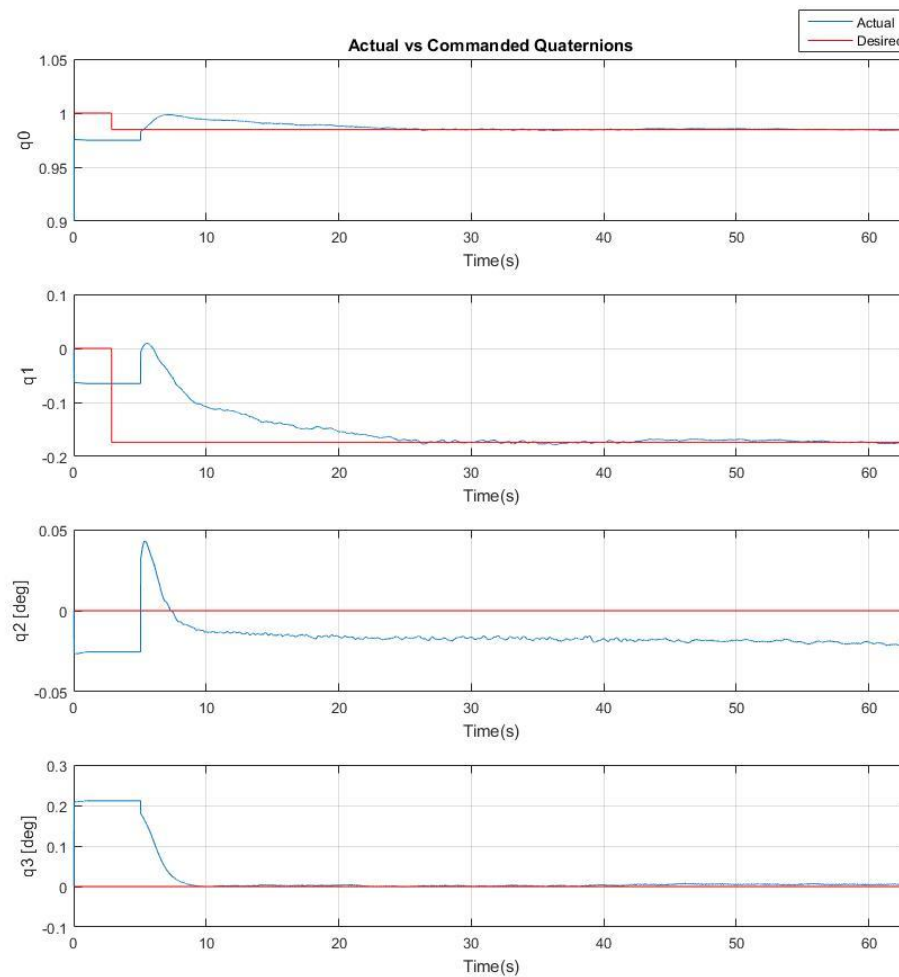

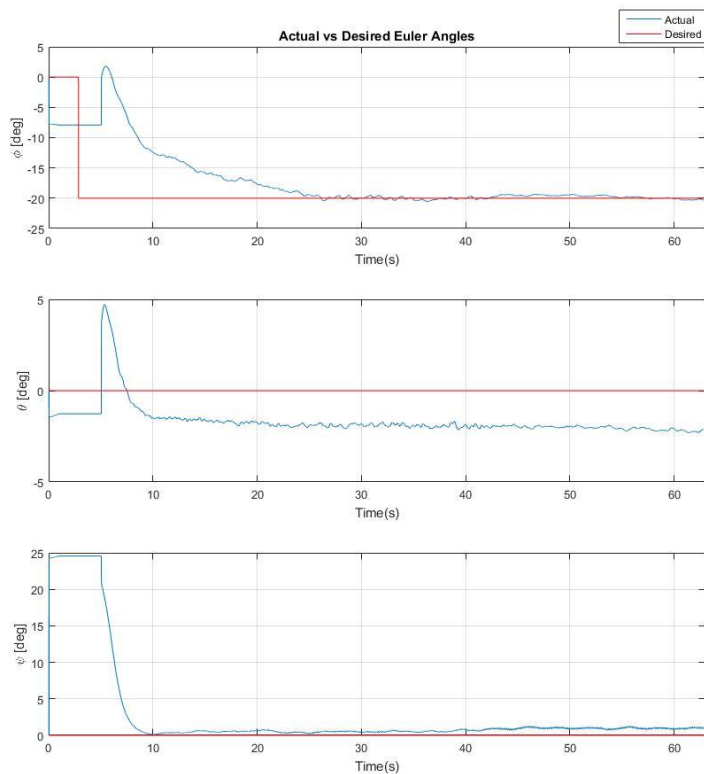*Figure 8.19* Quaternions Attitude Time History for Implementation Maneuver No. 4.

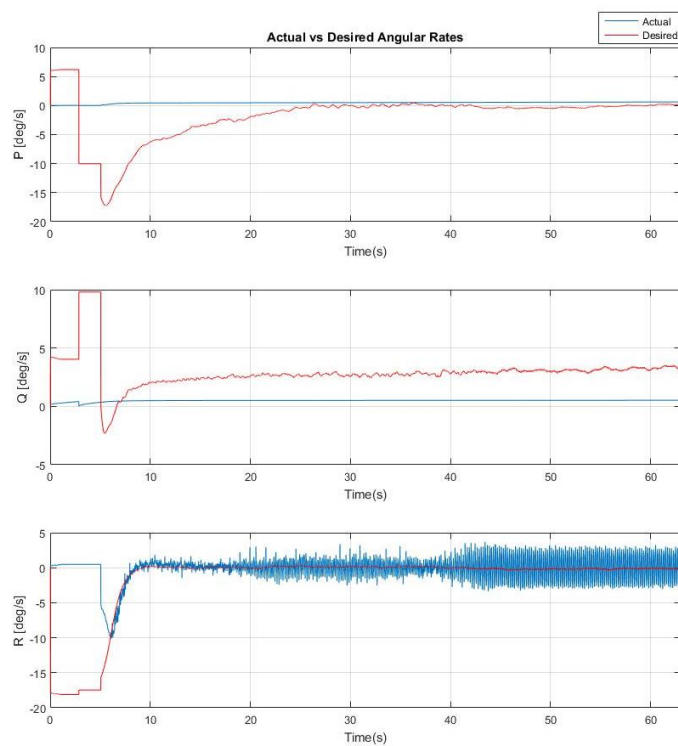*Figure 8.20* Euler Attitude Time History for Implementation Maneuver No. 4.

Figure 8.21 Angular Velocities Time History for Implementation Maneuver No. 4.

The desired moments provided by the implemented attitude control laws are used within the control allocation to provide the exact thrust force needed for each thruster. As part of the implementation process, each thrust force is converted into a duty cycle, as shown in Figure 2.13. Figure 8.22 shows the thrust force required for each of the thrusters involved in the yaw rotation. The corresponding duty cycle of this thrust force is shown in Figure 8.23. From Figure 8.23, it can be observed that the duty cycle is represented within a range between 1 and 0, representing the 'on' and 'off' state of the thruster. During the duty cycle corresponding to the yaw rotation, it can be seen that once the attitude is reached, the duty cycle is reduced.
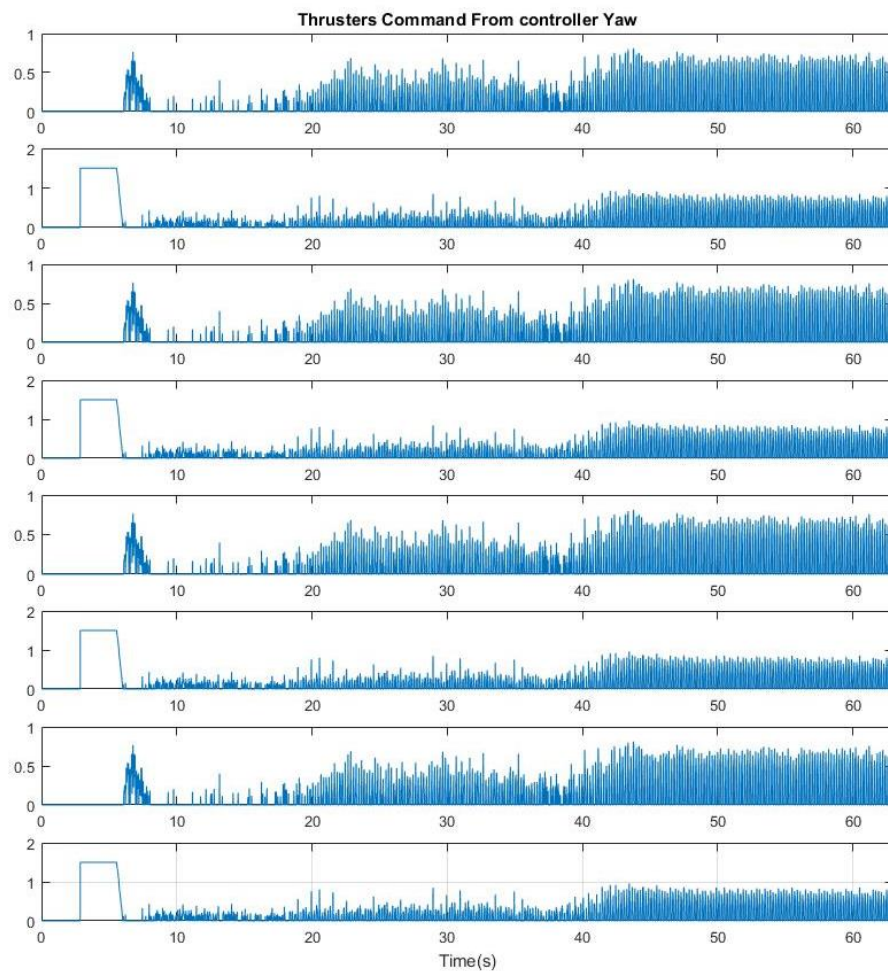

Figure 8.22 Thrust Commanded for Yaw Rotation in Implementation Maneuver No. 4.
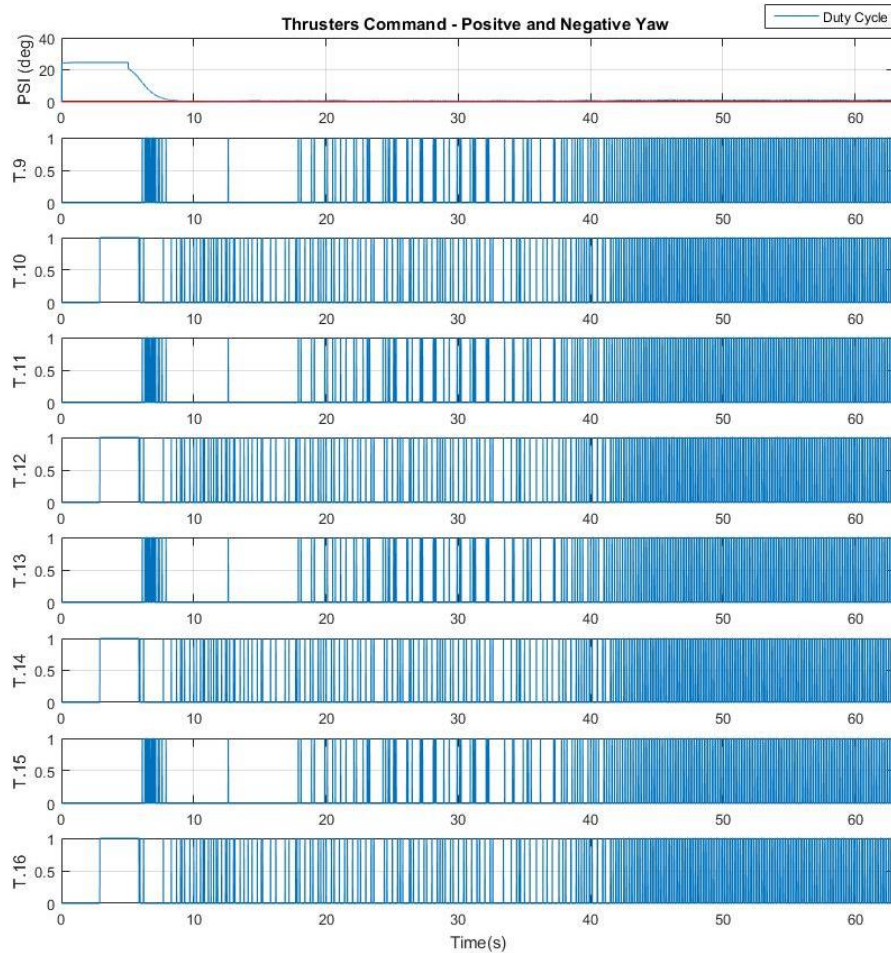
Figure 8.23 Duty Cycle for Yaw Rotation, Implementation Maneuver No. 4.

8.2.2 Attitude Performance with TMAE and TME

As outlined in Tables 8.12 and 8.13, different thrust misalignment angles and

magnitude thrust errors were chosen to study the performance of the controller under this

type of undesired dynamics. For this case, the vehicle is commanded to perform a final

maneuver as shown in table 8.14

Table 8.12

Configuration of Thrust Magnitude Error for Maneuver No. 5

Thruster No.	Thrust Magnitude error
1 and 2	1% of Thrust desired
9 and 10	

Table 8.13

Configuration of Thrust Misalignment Angles Error for Maneuver No. 5

Thruster No.	Thrust Misalignment Angle
11, 13, and 16	$\Delta\beta = 3$ $\Delta\alpha = 2$

Table 8.14

Implementation Maneuver No. 5

Time [s] Attitude [°]	0	1	2	3	4	5	6	7	8	9	10
ϕ	0	0	0	0	0	0	0	0	0	0	0
θ	0	0	0	0	0	0	0	0	0	0	0
ψ	**25**	**25**	**25**	**25**	**25**	**25**	0	0	0	0	0

Figures 8.24 and 8.25 illustrate the time history of the attitude stabilization. As it can be seen in the referenced plots, the attitude stabilization of the desired yaw rotation is kept during the whole maneuver. However, the degradation performance on the roll and pitch maneuvers is due to the presence of thrust misalignment angles in the yaw's thrusters (only) and the thrust magnitude error in the 1, 2, 9 and 10 thrusters. Thrust misalignment angles in the yaw thrusters generate an extra force component in the Z and X axes that creates a rotational moment with respect to the X and Y axes. As such, the thrust magnitude error decreases the force given to the thruster to perform the desired maneuver.

Even though the controller is able to maintain the desired yaw maneuver and the performance is degraded in the roll and pitch maneuvers, it is clear that the proposed controller has the capability of handling these amounts of undesired dynamic while maintaining the vehicle inside bounds of nominal stability.
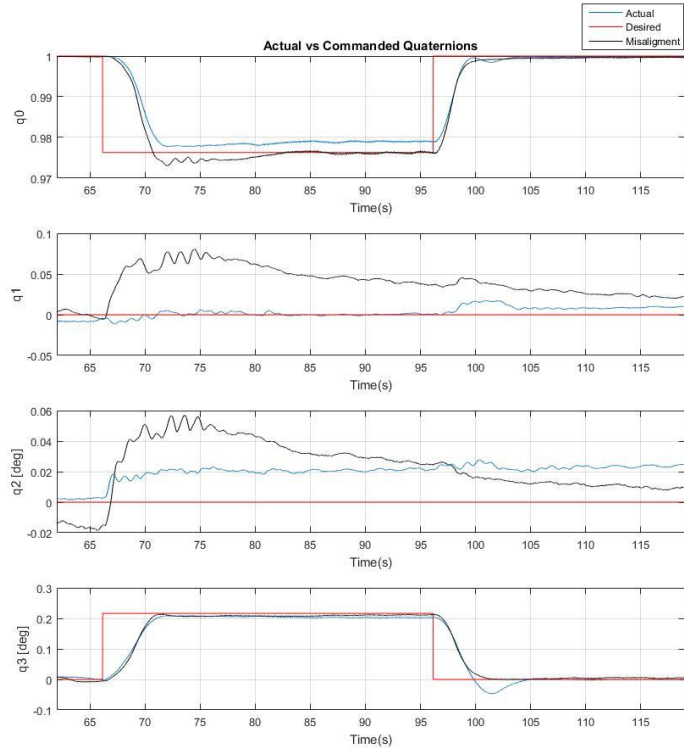
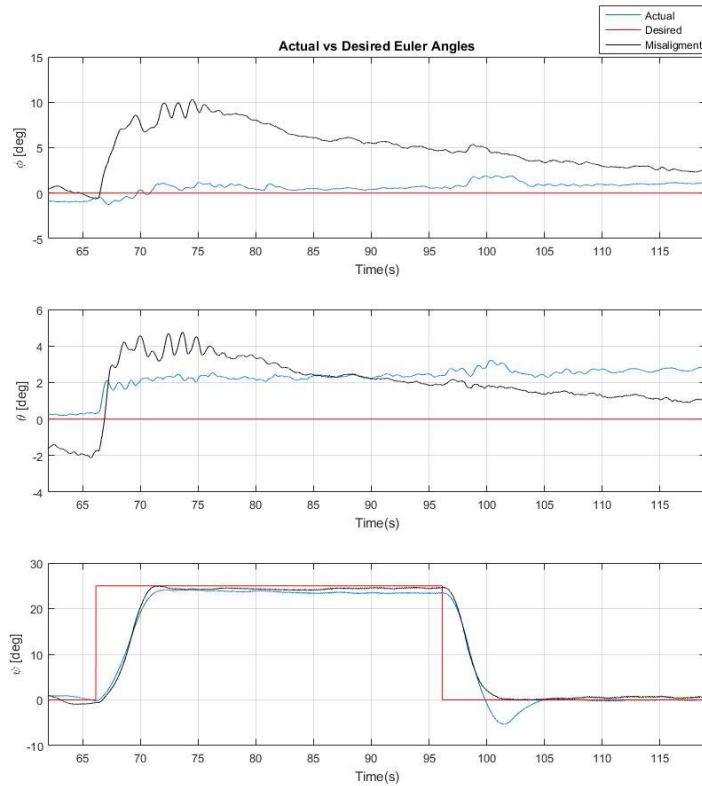*Figure 8.24* Quaternions Attitude Time History for Implementation Maneuver No. 5.

Figure 8.25 Euler Attitude Time History for Implementation Maneuver No. 5.
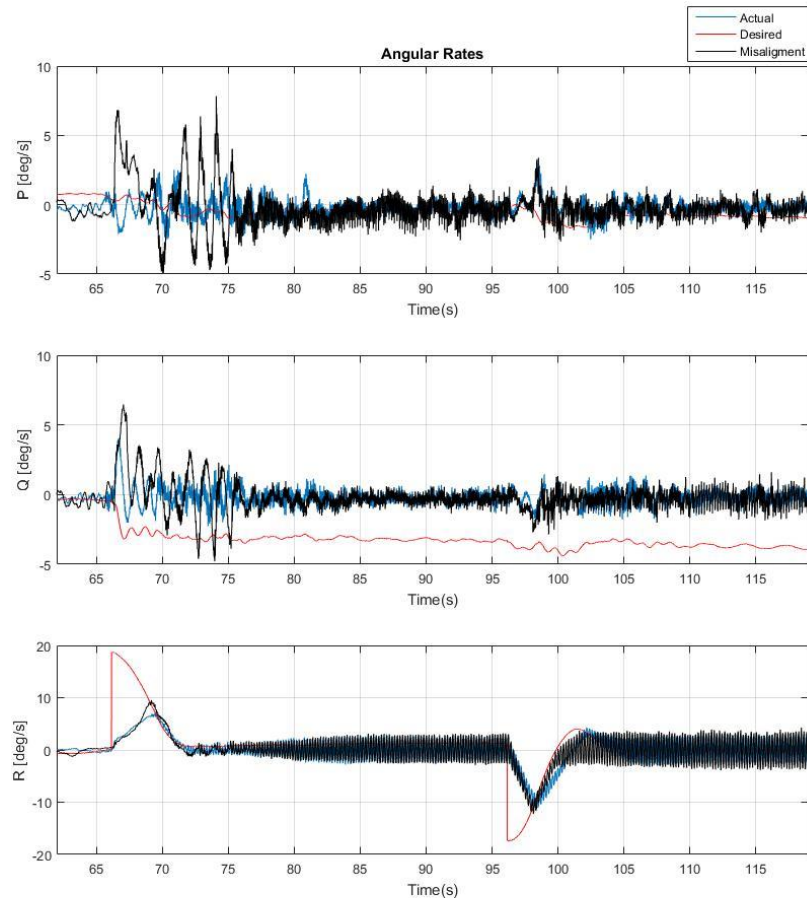
Figure 8.26 Angular Velocities, Implementation Maneuver No. 5.

Figure 8.26 shows the effect of undesired dynamics. Significant angular velocities p and q are present while the yaw maneuver is being performed.

Figures 8.27 and 8.28 show the moments and accelerations experimented by the spacecraft while the maneuver is performed. As already seen in the quaternions and Euler's angles representation plots, the stabilization performance of roll and pitch rotations is not accomplished. Looking at this error though the moments acting on the spacecraft in Figure 8.27, it can be noted that due to forces in the other axes, differential moments are generated thought the maneuver. A generation of extra moments implies a change in the acceleration of the corresponding axis.
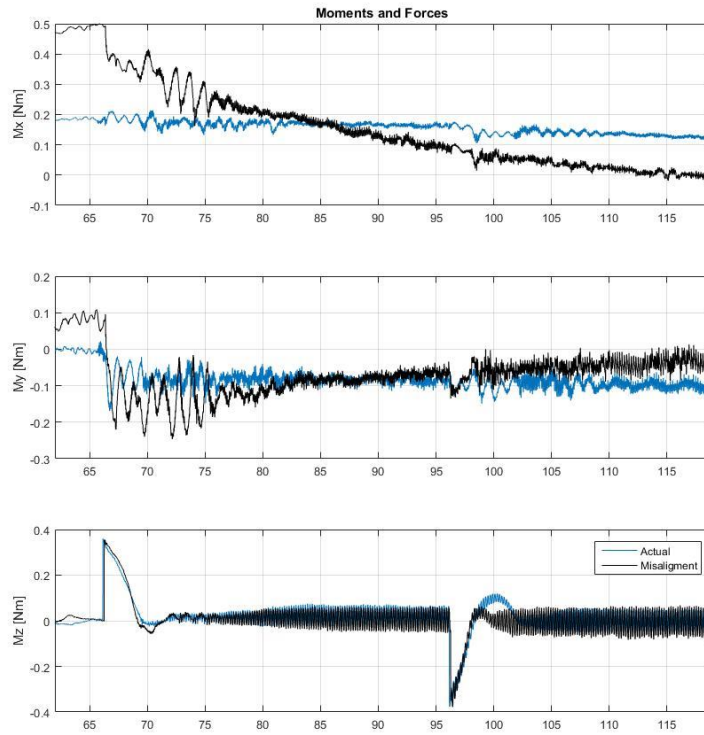
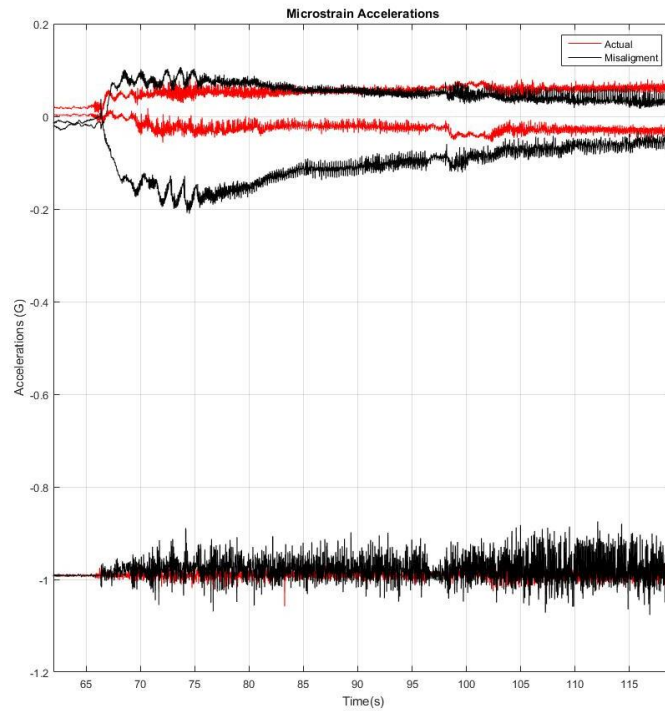*Figure 8.27* Moments Time History for Implementation Maneuver No. 5.

Figure 8.28 Body Accelerations Times History for Implementation Maneuver No. 5.

The amount of fuel spent by the propulsion system is increased, as shown in Figure 8. 29, demonstrating a notable increase in fuel expense when misalignments and thrust magnitude errors are present in the attitude thrusters. This increase may be explained by the amount of extra firing activity of the thrusters trying to compensate for undesired moments generated by such undesired dynamics.

As shown in Figure 8.30, the global performance index was also calculated for the entire duration of the maneuver. It is clear that the overall performance of the mission is degraded when misalignments and thrust magnitude errors are present in the system.
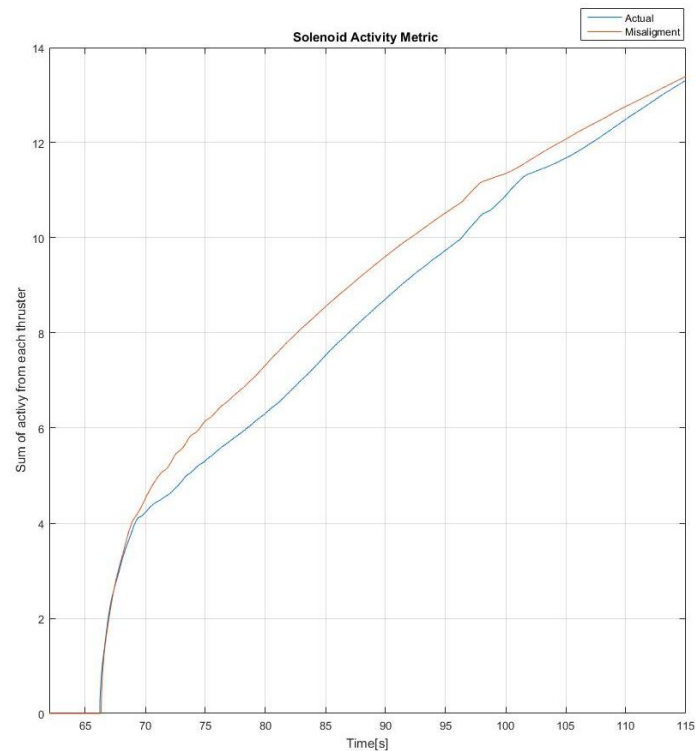

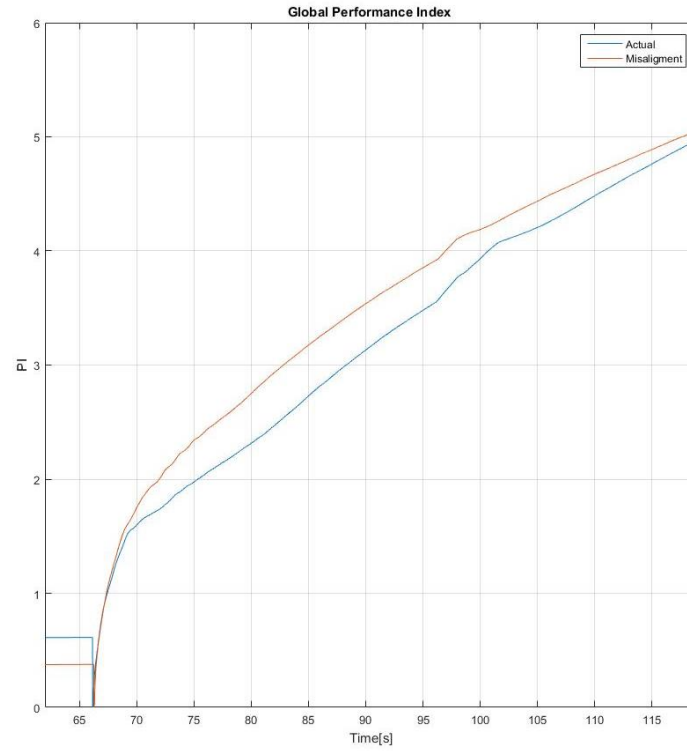*Figure 8.29* Solenoid Activity Metric, Implementation Maneuver No. 5.

Figure 8.30 Global Performance Metric, Implementation Maneuver No. 5.

9. Conclusions

This thesis study has explored the functionality of implementing a research spacecraft test-bed Extreme Access System (EASY) to support the testing, validation, verification and assessment of control laws algorithms. The developed prototype demonstrated significant capabilities and potential as a testbed for design and testing of control law algorithms. Specifically, the controller exhibited high fidelity, attitude stabilization and satisfactory performance.

A simulation environment was developed to support the objectives of this thesis and evaluate different mission scenarios previous to implementation. Performed numerical simulations included the analysis of the system when undesired dynamics such as misalignment angles and thrust magnitude errors are present.

Moreover, a description of the design, development, and implementation of a quaternions feedback linearization controller has been described. Overall, it was demonstrated through the implementation the capabilities of the designed controller to maintain the overall stability of the spacecraft. Even in the presence of undesired dynamics associated to thrust misalignment angles in the thrusters and errors in the thrust magnitude generated by the propulsion system the vehicle was able stabilized to the desired maneuver. Errors by 2 degrees are presented in the stabilization performance of the attitude; this can be explained by multiple causes that are external to the proposed controller by itself. The mentioned causes are related to the disturbances presented at the laboratory such as air coming from the air conditioner system, deformation of the tubing plastic, leaks of pressure,etc.

10. Recommendations and Future Work

There are still many avenues not shown in this thesis for future work in different areas. As mentioned earlier, this research Spacecraft test-bed can be used for the design validation and verification of multiple control law systems. So far, only a quaternion feedback linearization based controller has been implemented. However, multiple controllers such a PID, LQR, Adaptive and other controllers can be tested using this Spacecraft test-bed. For the tuning process of each controller is recommended to have a constant fuel supply attached to the vehicle. A pneumatic setup with a pair of storage cylinder for compressed air attached to the IGOR structure will provide this capability.

In terms of the propulsion system, there are two possible ways to enhance the thrust produced by the thrusters, that could be an interesting topic for future work, is to redefine the nozzle's dimensions as well as the manufacture and material method used for them. A metallic 3D printer could be used for this purpose. Moreover, the second one is to change the type of fuel, EASY'S pneumatic system is able to handle cold gas using the same air tanks described in chapter 2. Regarding the pressure lines that conduct the compressed air, the use of steel tubing instead of plastic tubing will avoid pressure leaks of the system, as weel as, possible deformations of the material due to the use of it.

For navigation purposes, the implementation of optical-flow based vision will provide the geopositional data required to perform translation displacements inside the environment testing described in chapter 7.

Finally, this thesis was not shown the thrust vectoring capability of the vehicle. Future implementation of control laws for the Thrust Vectoring Control Configuration will enhance the performance of the vehicle.

REFERENCES

ADVANTECH. (2019, November). *ADVANTECH*. Retrieved from ADVANTECH: https://www.advantech.com/products/pc-104-cpu-boards/sub_1-2jkltu

Brophy, J. R., Friedman, L., Strange, N. J., Prince, T. A., Landau, D., Jones, T., . . . Mansella, D. (2014). Synergies of Robotic Asteroid Redirection Technologies and Human Space Exploration. *65th International Astronautical Congress.* Toronto, Canada.

Compressors, A. (2019, November). *ALKIN Compressors*. Retrieved from ALKIN Compressors: https://www.alkinus.com/w31_mariner

De Ruiter, A. H., Damaren, C. J., & Forbes, J. R. (2013). *Spacecraft Dynamics and Control An Introduction.* West Sussex: John Wiley & Sons Ltd.

Dentis, M., Elisa, C., & Guglieri, G. (2016). A novel concept for Guidance and Control of Spacecraft Orbital Maneuver. *HINDAWI.*

Diamond Systems. (2019, November). *Diamond Systems*. Retrieved from Diamond Systems: http://www.diamondsystems.com/products/onyxmm

FESTO. (n.d.). *FESTO*. Retrieved from FESTO: https://www.festo.com/cat/en-gb_gb/data/doc_ENGB/PDF/EN/MH2TO4_EN.PDF

Garcia, D., Perez, A., Moncayo, H., Rivera, K., DuPuis, M., & Mueller, R. (2017). Spacecraft Heath Monitoring Using a Biomimetic Fault. *AIAA Information Systems-Infotech Aerospace Conference.* Grapevine, Texas.

Han, O., Kienholz, D., Janzen, P., & Kidney, S. (2010). Gravity-Offloading System for Large-Displacement Ground Testing of Spacecraft Mechanisms. *40th Aerospace Mechanisms Symposium, NASA Kennedy Space Center.*

Hever, M., Richard, P., & Ke, Z. (2015). Free-Flyer Robotic Spacecraft for Exploration and In Situ Resource Utilization of Interplanetary Bodies. *5Th International Workshop on Lunar Surface Applications, Lunar Landers, Lunar Surfaces Science and Lunar ISRU.* Cocoa Beach, FL.

Hockman, B., Frick, A., Nesnas, I., & Pavone, M. (2015). Design, Control, and Experimentation of Internally-Actuated Rovers for the Exploration of Low-Gravity Planetary Bodies. *Conference on Field and Service Robotics.* Toronto, Canada.

Hu, Q., Li, B., Huo, X., & Shi, Z. (2013). Spacecraft attitude tracking control under actuator magnitude. *Aerospace Science and Technology 28*, 266-280.

Inc, U. (2019, November). *Ubiquiti Inc*. Retrieved from Ubiquiti Inc: https://www.ui.com/airmax/nanobeam-ac-gen2/

Landis Markley, F., & Crassidis, J. L. (2014). *Fundamentals of Spacecraft Attitude Determination and Control.* New York: Springer Science+Business Media .

Lim, H.-C., & Bang, H. (2009). Adaptive control for satellite formation flying under thrust. *Acta Astronautica 65*, 112 – 122.

LORD SENSING MicroStrain. (2019, Novwmbwe). *LORD SENSING MicroStrain*. Retrieved from LORD SENSING MicroStrain: https://www.microstrain.com/inertial/3dm-gx4-45

NASA . (1974). *Solid Rocket Thrust Vector Control.*

National Aeronautics and Space Administration NASA. (2015, November 24). *United States Patent No. US 9,194,977 B1.*

NINJA. (2019, Novemebr). *NINJA*. Retrieved from NINJA: https://www.ninjapaintball.com/

Perez , A. (2016). *Development of Fault Tolerant Adaptive Control Laws for Aerospace Systems.* Daytona Beach, FL: Embry Riddle Aeronautical University .

Perez , A., Moncayo, H., Prazenica, R., Zacny, K., Mueller, R., Ebert, T., & DuPuis, M. (2016). Control Laws Development for a Free-Flying Unmmanned Robotic System to Support Interplanetary Bodies Prospecting and Characterization Missions. *AIAA Science and Technology Forum and Exposition.* San Diego, CA.

Prazenica , R., Kern, K., Jhon , T., Moncayo , H., Zacny , K., Mueller, R., . . . Dupuis, M. (2016). Vision-Aided Navigation for Free- Flying Unmanned Robotic System to Support Interplanetary Bodies Prospecting and Characterization Missions Control . *Scitech Conference, GNC, Aerospace Robotics and Unmanned/Autonomous System IV.*

Sidi, M. J. (1997). *Spacecraft Dynamics and Control A Practical Engieering Approach.* Cambridge University Press.

Sutton, G., & Biblarz, O. (2010). *Rocket Porpulsion Elements.*

Systems, D. (2019, November). *Diamond Systems*. Retrieved from Diamond Systems: https://www.diamondsystems.com/products/emeraldmm

Wie, B. (2015). *Space Vehicle Guidance Control, and Astrodynamics.* Reston, Virginia: American Institute of Aeronatuics and Astronautics, Inc.

Wie, B. (2015). *Space Vehicle Guidance, Control and Astrodynamics.* Reston, Virginia: American Institute of Aeronautics and Astronautics, Inc.

Wie, B., & Barba, P. M. (1985). Quaternion Feedback for Spacecraft Large Angle Maneuvers. *Journal of Guidance Control and Dynamics*, 360-365.

Zacny, K., Yaggi, B., Spring, J., Chu, P., Mueller, R., Ebert, T., . . . Prazenica R. (2016). Sample Acquisition System for a Free-Fying Unmmanned Robotic System to Support Interplanetary Bodies Prospecting and Characterization Missions. *Scitech Conference,Extraterrestrial Water: Prospecting and Acquisition.*